A Mathematical Model of Dendritic Microstructures in Nickel-Based Superalloys

Wei Wang

A thesis submitted for the degree of PhD at University of London and for the Diploma of Imperial College London.

Aug 2003

Department of Materials
Imperial College London
University of London, United Kingdom

不积跬步，无以致千里；

不积小流，无以成江海。

——《荀子·劝学篇第一》

Without the first small step, a faraway destination can never be reached;

without the initial tiny stream, an immense sea can never come into being.

—— Chinese archaic poem

Abstract

A mathematical model has been constructed in order to understand the development of dendritic structures formed in directional solidification of nickel-based superalloys. This model uses the cellular automaton technique to track the nucleation and growth of the solid phase from liquid phase, and a finite difference calculation for the diffusion of the alloying solute. Both the constitutional undercooling and the curvature undercooling are simulated, since they affect the growth velocity of the solid/liquid interface. The effect of crystallographic anisotropy is studied by the adaptation of a decentred square/octahedron growth algorithm. The model is three dimensional but when it runs on a domain composed of only one layer of cells, it degrades into a two-dimensional model.

This model has been applied to three specific aspects of microstructural development: the selection of stable primary dendrite spacing during directional solidification under varied growth conditions; multi-directional dendritic growth in the platform region of a turbine blade; and competitive growth at converging and diverging grain boundaries. For the first of these, simulations were carried out in both two and three dimensions; but only in two-dimensions for the other two. For competitive growth, a phase filed model developed by other researchers was used to carry out further investigations. The results of the simulation were compared with earlier analytical predictions, and with other computational and experimental results.

It was found that in directional solidification primary dendrite spacing is dependent on the processing history, that there is a range of stable spacings for any given growth condition which is reduced by perturbation. Sudden changes in the cross-sectional area of the turbine blade can give rise to a significant increase in the tip undercooling, favouring the nucleation of stray grains; with the combined effect of concave isotherms, a self-converging grain boundary tends to form. The simulations showed excellent correlation with prior theoretic analyses, computational models and experimental results.

Acknowledgements

I would like to express my sincere gratitude to my supervisors, Dr. Peter D. Lee and Prof. Malcolm McLean. Apart from their painstaking guidance and high standard supervision, they have also provided me with opportunities for systematic training in scientific research and interaction with other researchers, both of which have been very beneficial for me, not only in my PhD research, but also for my future career.

I would like to express my heartfelt thanks to Dr. Ingo Steinbach, director of the Access Center, RWTH-Aachen, Germany, where I worked as a visiting researcher for three months during my PhD course. Some of the work presented in this thesis was carried out under his supervision. Thanks are also due to his colleagues, Dr. Hermann-Josef Diepers, Mr. Philippe Schaffnit, Ms. Janin Tiaden, Dr. Bernd Böttger, Dr. Markus Apel and Dr. Dexin Ma, each of whom gave me a lot of valuable suggestions and kind help. Not only did I benefit greatly from the collaboration with Ingo's group, but also I enjoyed a very pleasant life in such a nice place as Aachen.

I would like to thank Dr. Ahmad Kermanpur who worked on the same project with me. He spent a lot of time doing experiments and carrying out comparisons between my simulation results and experimental work. He is an excellent co-worker and more than half my publications arose from our collaboration.

I would like to thank Dr. Robert C. Atwood for providing a lot of help on programming: he is like a live 'encyclopaedia', and is always willing to give me constructive suggestions when I discuss things with him. The computational program that I developed during my PhD research was based on the framework of one that he developed during his PhD.

I thank Dr. Yehia M. Youssef and Mr. Stuart McCallum (shortly to become Dr. McCallum), who were also doing their PhDs while I was working on mine. It was a very helpful to have a chat with them after a long day of tense effort. Though working on different projects, we sometimes came across similar problems, and we all benefited a lot from shared information and mutual encouragement.

I also thank my other colleagues in the Materials Processing Group (MPG). I quite like the fact that it is indeed an international team with members from Asia, Africa and America and Europe (perhaps we may recruit a new student from Oceania in the future?). I am especially indebted to Mr. Jianzhang Yi who provided generous support when I was in trouble. I would also like to acknowledge Dr. Hongbiao Dong and Ms. Xiaoli Yang, with each of whom I had a short period of cooperation.

My acknowledgements go also to Dr. Xuehua Xu, Dr. Weishan Zhang and Dr. Ali Chiraz, former members of MPG, for their help and assistance when I started my PhD. Dr. Weishan Zhang in particular because it was through him that I had the opportunity to work with Dr. Peter D. Lee and Prof. Malcolm McLean.

I also thank those in the Department of Materials who have given me all kinds of help, particularly Ms. Norma Hikel who helped me to prepare tons of documents for my applications for so many visas and travel grants to attend conferences and to visit other research centres. I thank Mrs. Andrea M. Walker for her kind help with proof reading my writing.

Many thanks to EPSRC, ORS and Rolls-Royce plc for their financial supports and to those from the Birmingham IRC, University of Cambridge, Rolls-Royce plc, Special Metals Wiggin Ltd, Wyman-Cordon Ltd and QinetiQ, all of whom worked on same grand project as I did, 'Integrated Modelling of the Manufacture of Aerospace Discs (IMMAD)'.

I would like to express my deepest appreciation and warmest regards to my dearest parents and to my brother for all their understanding and continuous support. I would also like very much to thank my girlfriend, Miss Xiaoli Zhong, who was preparing her MSc examinations when I was writing my thesis. The spring of 2003 saw us both working very hard even on sunny weekends! Without her company, writing thesis could never have been half so enjoyable a task.

Table of Contents

List of Figures

List of Tables

List of Symbols

A	area
A	number
B	constant
C	concentration
C_0	initial concentration
C_L	concentration in liquid
C_S	concentration in solid
C^*	concentration at solid/liquid interface
D	diffusion coefficient
D_L	diffusion coefficient in liquid
D_S	diffusion coefficient in solid
F	free energy
G	thermal gradient
G'	dimensionless thermal gradient ($G' = G\Gamma/(mC_0)^2$)
G_C	solute concentration gradient in liquid
H	energy
I	nucleation rate
K	number
L	length
N	number
Pe	Péclet number (defined as a half of the product of tip radius and tip velocity divided by diffusion coefficient in liquid)
R	radius
T	temperature
T_{liq}	liquidus temperature
V	pulling velocity
V_{CA}	volume of cell
V_n	velocity of solid/liquid interface
V_{tip}	tip velocity
V'	dimensionless pulling velocity ($V' = V\Gamma/(D_L mC_0)$)
a	number

b	number
c	number
d	critical diffusion length
c_p	specific heat
f_S	fraction of solid
f_g	volume fraction occupied by grain envelope
f_i	internal fraction of solid
k	equilibrium partition coefficient
k_B	Boltzmann's constant
m_l	liquidus slope
n	number
n	nucleation density
$n_{\max}$	the maximum nucleation density
p	probability of nucleation
r	radius
r	random number
t	time
v	velocity
x	coordinate
x_B	solute mole fraction
y	coordinate
z	oordinate
ΔG	free energy
ΔG_d	activation energy for diffusion across solid/liquid interface
ΔG°	activation energy for nucleation
ΔG_n°	activation energy for nucleation
ΔT	undercooling
ΔT_C	constitutional undercooling
ΔT_K	kinetic undercooling
ΔT_N	the mean nucleation undercooling
ΔT_R	curvature undercooling
ΔT_t	thermal undercooling

ΔT_{total}	total undercooling
ΔT_{σ}	the standard deviation of nucleation-undercooling distribution curve
$\Delta T'$	dimensionless undercooling ($\Delta T' = \Delta T k / [mC_0(k-1)]$)
Δf_S	increment of fraction of solid
Δh_f	latent heat of fusion per unit volume
Δs_f	entropy of fusion per unit volume
Δt	time step
Δx	cell size
Γ	Gibbs-Thomson coefficient
Ω	supersaturation
α	thermal diffusivity
δ	solute boundary layer thickness
δ	solid/liquid interface thickness
ε_{kin}	amplitude of anisotropy of mobility
ε_{st}	amplitude of anisotropy of surface energy
η	distance
φ	the phase field variable
$\dot{\varphi}$	changing rate of the phase field variable
κ	curvature
λ_1	primary dendrite spacing
λ_1'	dimensionless primary dendrite spacing ($\lambda_1' = \lambda m C_0 / \Gamma$)
μ	kinetic coefficient
θ	angle
σ	solid/liquid interface energy
ξ_C	a function of Pe

Chapter 1
Introduction

The continuous improvement in the efficiency of gas turbines for both aerospace and power applications has benefited significantly from continual improvements in the alloys used for both turbine blades and discs. Nickel-based superalloys are widely used in the aerospace industry because of their good performance at the high temperatures at which modern gas turbines usually operate. The performance of these alloys is dependent upon both their composition and the way in which they are processed. The first stage of processing is usually by solidification from a melt, where an initial microstructure is formed and subsequently altered by thermo-mechanical processing and/or heat treatment. The engineering requirements of turbine blades and discs are quite different. The operating temperature of the blades is maximised for engine thermal efficiency, requiring a combination of high temperature creep resistance coupled with thermal fatigue resistance during engine cycling. Discs operate within a lower temperature regime and thus require a high strength alloy to accommodate the large centrifugal forces experienced during engine operation and good resistance to fatigue crack propagation. These separate requirements have led to the development of very different classes of materials but in both cases the properties are dependent upon the solidification microstructure.

The microstructure of cast turbine blades has progressed from an equiaxed to directionally solidified (DS) and subsequently to single crystal (SX) grain structures. The processing requirements to achieve these structures have become increasingly stringent, and the propensity for the formation of defects has increased. Key to the formation of defects is dendritic growth. In DS and SX blades, misaligned stray grains cause many parts to be rejected (Pollock, *et al.* 1996). In discs, the initial microstructure is formed during a secondary remelting process, such as Vacuum Arc Remelting (VAR). During VAR, variations in the process parameters can lead to solidification features or defects such as freckles (macrosegregation) (Auburtin, *et al.* 2000) and tree rings (strings of equiaxed grains in an otherwise columnar dendritic microstructure) (Xu, *et al.* 2000). Understanding the formation of defects in both blade and disc alloys, requires a fundamental knowledge of the growth of the initial dendritic microstructure during solidification.

In this thesis, a mathematical model of dendritic microstructures in nickel-based superalloys is presented. The original code was written by Dr. Peter D. Lee, and then

expanded by a few prior PhD students (Dr. Robert C. Atwood and Dr. Xuehua Xu, *et al.*). I further expanded the code in several significant ways: incorporation of decentred square/octahedron grain growth algorithm, introduction of moving frame of reference technique, and many minor additional extensions and bug fixes.

A literature review is presented in Chapter 2 which describes the theory, experiments and modelling of solidification. In the section on modelling different types of numerical models of solidification are reviewed, with particular emphasis on the two major approaches: cellular automaton models and phase field models, and a comparison of these is carried out.

Chapter 3 describes the modelling theory in detail, including the assumptions made and solution techniques used. The model is a combination of a cellular automaton description of grain nucleation and growth and a finite difference computation of solute diffusion.

In Chapter 4, two-dimensional simulation results of directional solidification under well defined conditions are presented and discussed. The simulation results are compared with earlier theoretical and numerical predictions.

Three-dimensional simulations of directional solidification are presented in Chapter 5, and compared with the two-dimensional simulation results. The numerical predictions are also compared with earlier experimental results.

In Chapter 6 another application of the model is presented: simulation of the dendritic growth in a platform region of nickel-based superalloy turbine blades. The simulated structure is then compared with experiments.

Competitive growth between differently orientated grains is also studied using the model, and the results are presented in Chapter 7. The limitations of the model in this context are discussed, and a phase field model developed by other researchers is applied to carry out further investigations.

Conclusions are drawn in the last chapter, followed by recommendations for future work.

Chapter 2
Background

Solidification phenomena play an important role in many of the processes used in industrial fields for the production of metal and alloy components. The course of solidification is affected by material properties (e.g. liquidus temperature, initial concentration, equilibrium partition coefficient and solute diffusivity *et al.*) and processing parameters (e.g. initial temperature and cooling rate *et al.*). Changes in material properties and processing parameters can lead to different solidification structures, which will in turn affect the properties of the solidified products. Solidification has been the subject of extensive experimental and numerical investigations, as reviewed by (Hunt 1979; Laxmanan 1985; Kurz, *et al.* 1992). In this chapter the fundamental theory of solidification will be briefly reviewed, followed by descriptions of experiments and modelling of solidification. In the section on solidification modelling, several numerical methods are covered, with particular emphasis put on two major methods: cellular automaton models and phase field models.

2.1 Theory of Solidification

Solidification is a transformation process in which liquid phase changes into one or several solid phases. This process starts with grain nucleation and continues with solid growth.

2.1.1 Grain Nucleation

From a thermodynamic point of view, nucleation is the initial stage of phase transformation during which the total free energy approaches a lower value. When a liquid is in a state that the free energy of any solid phase is lower than that of the liquid phase, it becomes unstable and is likely to transform into one or several solid phases. But practically this transformation does not occur instantly, or in other words, a liquid can keep a supercooled or supersaturated state to a certain extent. Furthermore, when the condition is satisfied, the liquid does not change into solid entirely at the same time, and the transformation initiates at some sporadic places first. The reason for these phenomena is that some specific conditions must be satisfied to allow phase change to happen, or allow nucleation to start.

2.1.1.1 Homogeneous Nucleation

When a solid forms within its own melt without aid of foreign materials, it is said to nucleate homogenously (Flemings 1974). Homogenous nucleation involves creation of variously sized crystal clusters each with an interface between the liquid and solid phases. Assuming all the clusters have a spherical shape, the total free energy change, ΔG, for a single cluster with a radius of r can be written as (Kurz, *et al.* 1992)

$$\Delta G = \Delta G_I + \Delta G_V = 4\pi r^2 \sigma - \frac{4\pi r^3}{3} \Delta s_f \Delta T, \tag{2.1}$$

where ΔG_I is associated with the energy of solid/liquid interface formed, and ΔG_V associated with the difference in the free energies of liquid and solid, σ the solid/liquid interface energy, Δs_f the entropy of fusion per unit volume, and ΔT the undercooling.

At a temperature above or equal to the melting point, ΔG is always positive and increases monotonically with increasing radius, which means the solid phase is less stable than the liquid phase; therefore, no nucleation can occur naturally. At a temperature below the melting point, since the second term at the right hand side of equation (2.1) has a 3rd-power dependence on r while the first term only has a 2nd-power dependence, ΔG will become negative at large value of r, which means the solid phase is more stable than the liquid phase and nucleation is likely to occur. However, when r increases from 0 to infinity, ΔG has to pass through a maximum, $\Delta G°$, at a critical radius, $r° = 2\sigma / \Delta s_f \Delta T$,

$$\Delta G° = \frac{16\pi}{3} \cdot \frac{\sigma^3}{\Delta s_f{}^2} \cdot \frac{1}{\Delta T^2}. \tag{2.2}$$

The maximum value of free energy ($\Delta G°$) can be regarded as the activation energy for homogeneous nucleation, which has to be overcome in order to form a crystal nucleus that will continue to grow. When a fluctuation causes the cluster to become larger than $r°$, growth will occur due to the resultant decrease in the total free energy. $\Delta G°$ is the reciprocal of the square of ΔT, therefore, the higher the undercooling, the lower the activation energy, hence the easier for nucleation to happen.

The occurrence of homogeneous nucleation is limited to very restricted situations and often requires a quite high degree of undercooling. Otherwise, at the presence of nucleation agents or mould walls, the nucleation process will be facilitated and the threshold for nucleation undercooling is decreased, or heterogeneous nucleation occurs.

2.1.1.2 Heterogeneous Nucleation

When the melt contains solid particles, or is in contact with a crucible wall or oxide layer, nucleation may be facilitated if the activation energy is decreased, and it is said to nucleate heterogeneously (Flemings 1974). As shown in Fig. 2.1, a nucleus forms on the surface of a foreign solid, and the wetting angle, the contact angle between the nucleus and the foreign solid, is θ. Two new interfaces, A_{LC} and A_{CS} are formed during nucleation, one between the liquid and the nucleus, and the other between the nucleus and the foreign solid, but the area of the original interface between liquid and solid is also reduced by A_{CS}.

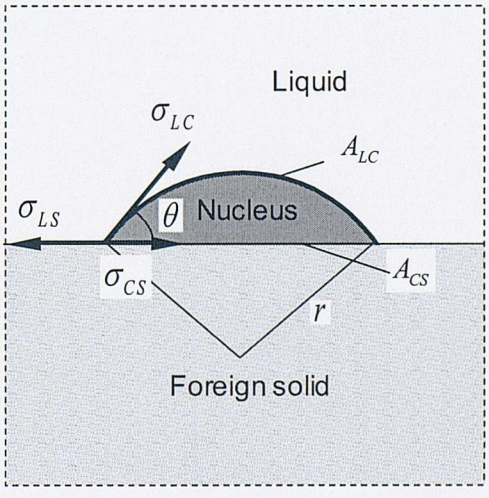

Fig. 2.1 Schematic of heterogeneous nucleation, and the wetting angle between the nucleus and the foreign solid is θ. There is a balance of surface tension of the interfaces between the liquid, the foreign solid and the nucleus (Kurz, *et al.* 1992).

The total free energy change can be expressed as

$$\Delta\tilde{G} = \left(\frac{4}{3}\pi r^3 \Delta s_f \Delta T + 4\pi r^2 \sigma_{LS}\right) \cdot f(\theta), \tag{2.3}$$

where $f(\theta)$ is a function of the wetting angle, θ,

$$f(\theta) = \frac{(2+\cos\theta)(1-\cos\theta)^2}{4}. \tag{2.4}$$

Following a similar analysis as in homogeneous nucleation, the activation energy for heterogeneous nucleation is

$$\Delta\tilde{G}^{\circ} = \frac{16\pi}{3} \cdot \frac{\sigma^2}{\Delta s_f^2} \cdot \frac{1}{\Delta T^2} \cdot f(\theta). \tag{2.5}$$

The value of $f(\theta)$ is always less than 1, thus the activation energy for heterogeneous nucleation is lower than that of homogeneous nucleation of a nucleus with the same radius r° . Therefore, heterogeneous nucleation is easier to occur in practical solidification process than homogeneous nucleation. Since the activation energy for heterogeneous nucleation is affected by the wetting angle (θ), it is possible to control the condition for heterogeneous nucleation by selecting appropriate crucible materials or adding appropriate nucleation agents.

2.1.1.3 Nucleation Rate

To calculate the number of nuclei formed in unit volume within unit time, the simplest case is considered, assuming the melt is an ideal mixture of small crystal clusters and liquid atoms. The number of clusters that contain n atoms is N_n, the number of atoms in liquid is N_L, and the equilibrium distribution of these clusters leads to (Kurz, *et al.* 1992)

$$\frac{N_n}{N_L} = \exp\left(-\frac{\Delta G_n}{k_B T}\right), \tag{2.6}$$

where k_B is the Boltzmann's constant, ΔG_n the free energy change for a nucleus containing n atoms formed in the melt, and T the temperature.

As ΔG is a function of the radius of a cluster, r, ΔG_n is a function of the atoms number in a cluster, n, and ΔG_n also passes a maximum at a critical value of $n°$. Beyond this value, ΔG_n decreases monotonically with increasing n, which means that the total energy of the cluster will decrease as the number of atoms in it increases. According to equation (2.6), under this circumstance, the number of clusters (N_n) will increase, which means that nucleation can occur naturally, and the nucleation rate is (Kurz, *et al.* 1992)

$$I = K_1 N_n^{\circ} = K_1 N_L \exp\left(-\frac{\Delta G_n^{\circ}}{k_B T}\right), \tag{2.7}$$

where K_1 is a constant.

Since the formation of clusters requires the transfer of atoms from the liquid to the nuclei, if the activation energy for diffusion across the solid/liquid interface, ΔG_d, is also considered, the nucleation rate is modified as (Kurz, *et al.* 1992)

$$I = I_0 \exp\left(-\frac{\Delta G_n^{\circ} + \Delta G_d}{k_B T}\right) = K_1 \exp\left(-\frac{K_2}{T\Delta T^2}\right)\exp\left(-\frac{\Delta G_d}{k_B T}\right), \tag{2.8}$$

where I_0 is a pre-exponential factor.

The above equation contains two exponential terms, one of which varies with $-1/T\Delta T^2$, while the other varies with $-1/T$. An increase in ΔT, giving more numerous and smaller nuclei of critical size, is accompanied by a decrease in T, resulting in fewer atoms transferred from the liquid to the nuclei. These opposite tendencies lead to a maximum nucleation rate, I_{max}, at a critical temperature, T_{CR}, as shown in Fig. 2.2.

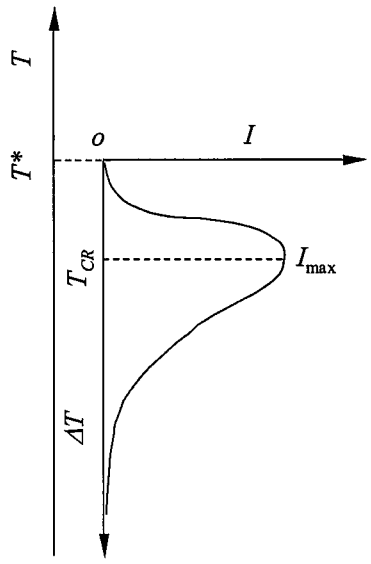

Fig. 2.2 Nucleation rate, I, is a function of temperature, T, and undercooling, ΔT. It approaches zero either as the temperature approaches absolute zero or approaches melting point, and passes a maximum at the critical value of T_{CR} (Thevoz, *et al.* 1989).

2.1.2 Solid Growth

Once an embryo has exceeded the critical size and becomes a stable nucleus, growth kinetics become important and dominate the solidification processes. For pure materials, the grain growth velocity is mainly decided by the efficiency to remove the heat of fusion; while for alloys, it is the result of combination of heat transfer and solute redistribution.

2.1.2.1 Diffusion Equation

The heat diffusion equations in liquid and solid are given as (Kurz, *et al.* 1992)

$$\frac{\partial T_L}{\partial t} = \nabla \cdot (\alpha_L \nabla T_L), \tag{2.9}$$

and

$$\frac{\partial T_S}{\partial t} = \nabla \cdot (\alpha_S \nabla T_S), \tag{2.10}$$

where T_L and T_S are temperatures in the solid and liquid, α_L and α_S thermal diffusivities in the liquid and solid, respectively. At the moving liquid/solid interface, the following boundary conditions should be satisfied

$$T_L^* = T_S^*, \tag{2.11}$$

and

$$\alpha_S \left.\frac{\partial T}{\partial n}\right|_S - \alpha_L \left.\frac{\partial T}{\partial n}\right|_L = \Delta h_f V_n, \tag{2.12}$$

where T_L^* and T_S^* are respectively temperatures of the liquid and solid at the interface, and Δh_f heat of fusion per mole, and V_n the moving velocity of the interface.

For alloy systems, solute diffusion in the liquid and solid is governed by following equations (Kurz, *et al.* 1992)

$$\frac{\partial C_L}{\partial t} = \nabla \cdot (D_L \nabla C_L), \tag{2.13}$$

and

$$\frac{\partial C_S}{\partial t} = \nabla \cdot (D_S \nabla C_S), \tag{2.14}$$

where C_L and C_S are solute concentrations in liquid and solid phases, D_L and D_S are diffusion coefficients in the two phases, respectively. The local equilibrium condition at the liquid/solid interface leads to

$$C_S^* = kC_L^*, \tag{2.15}$$

where k is the equilibrium partition coefficient.

2.1.2.2 Constrained Growth

In directional solidification, the direction of heat flow is opposite to that of the growth direction. This situation is often referred to as constrained growth, that is, the rate of advance of the isotherms constrains the grains to grow at a given velocity.

The morphology of the solidification front is dependent on both the pulling velocity and the thermal gradient in directional solidification: when the pulling velocity is sufficiently low and the thermal gradient is sufficiently high, a flat solidification front can be maintained, and no microsegregation is resulted; when the pulling velocity increases and/or thermal gradient decrease, the flat solidification front will become unstable and breaks down in to cellular structure, and microsegregation occurs; when the pulling velocity increases and/or thermal gradient decreases to a further extent, the cellular structure can transform into a dendritic structure, where microsegregation happens at both primary and secondary dendrites (McLean 1983).

For dendritic growth the morphology of the solidification front is quite complex, but a dynamic equilibrium condition is maintained at the solid/liquid interface, which can be expressed in terms of different undercoolings as (McCartney, *et al.* 1984)

$$\Delta T_{\text{total}} = T_{\text{liq}}^{0} - T_{\text{actual}} = \Delta T_t + \Delta T_C + \Delta T_R + \Delta T_K, \tag{2.16}$$

where ΔT_{total} is the total undercooling at the interface, T_{liq}^{0} the liquidus temperature at the initial concentration, T_{actual} the actual temperature, ΔT_t the thermal undercooling arising from the release of latent heat, ΔT_C the constitutional undercooling incurred by solute redistribution of portioned solute at the interface, ΔT_R the curvature undercooling due to the effect of surface tension, and ΔT_K the kinetic undercooling which is related to the velocity of the interface.

2.1.2.3 Primary Dendrite Spacing

A convenient and widely used measure of the effects of solidification conditions on dendrite structure is primary dendrite spacing. In directional solidification the columnar dendrites can adjust their spacing according to the varying pulling velocity and thermal gradient. As shown in Fig. 2.3, if the spacing is too close, one or another

primary arm falls behind and finally vanishes, and thus the spacing is increased; if the spacing is too wide, a ternary arm growing from a secondary arm catches up to the growing primary tips and becomes one of them, or tip branching occurs, then the spacing is reduced.

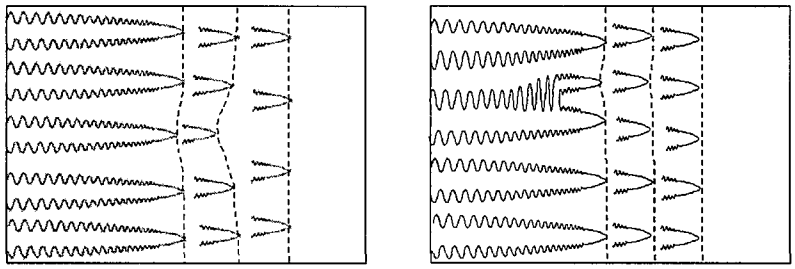

Fig. 2.3 Schematic illustration of spacing adjustment mechanisms for columnar dendritic growth: (a) if the primary arm spacing is too close, one or another primary arm falls behind and the spacing is increased; (b) if the spacing is too wide, new dendrite forms by tip splitting and the spacing is decreased (Wan, *et al.* 1997).

Flemings (Flemings 1974) suggested that the primary dendrite spacing dependents on the product of thermal gradient (G) and pulling velocity (V)

$$\lambda_1 = A(GV)^{-n}, \tag{2.17}$$

where n is generally very close to 0.5, and A is a coefficient determined by experiments.

Hunt (Hunt 1979) predicted a slightly different expression for primary dendrite spacing in directional solidification

$$\lambda_1 \propto G^{-0.5} \cdot V^{-0.25}. \tag{2.18}$$

By taking into account the equilibrium partition coefficient, solute diffusivity, and surface tension, Kurz and Fisher (Kurz, *et al.* 1992) derived a more complex expression

$$\lambda_1 = 4.3\left(\Delta T_0 D_L \Gamma\right)^{0.25} k^{-0.25} G^{-0.5} V^{-0.25}, \tag{2.19}$$

where ΔT_0 is the liquidus-solidus range at the initial concentration C_0. This relationship is in better agreement with Hunt's solution than Fleming's prediction.

Through numerical simulations, Hunt and Lu (Hunt, *et al.* 1996) obtained a quantitative relation between dimensionless primary dendrite spacing, λ_1', dimensionless thermal gradient, G', and dimensionless pulling velocity, V',

$$\lambda_1' = 0.07798 G'^{-0.6028} V'^{(a-0.75)} \left(V' - G'\right)^{0.75}, \tag{2.20}$$

where the dimensionless variables are defined as $\lambda_1' = \lambda m C_0 / \Gamma$, $G' = G\Gamma/(mC_0)^2$, and $V' = V\Gamma/(D_L m C_0)$ (where m is liquidus slope, C_0 initial concentration and Γ Gibbs-Thomson coefficient), and a is given by

$$a = -1.131 - 0.1555 \log_{10}(G') - 7.589 \times 10^{-3} \left[\log_{10}(G')\right]^2. \tag{2.21}$$

It is necessary to point out that in equation (2.20), the variable λ_1' refers to half spacing.

2.2 Experiments of Solidification

Dendritic growth has been the subject of extensive experimental and numerical investigation (reviewed by (Hunt 1979; Laxmanan 1985; Kurz, *et al.* 1992)).

2.2.1 Transparent Analogue Experiments

Many difficulties have been encountered in the study of solidification in metals because they are opaque. It would be of great interest to directly observe the solid/liquid interface morphology during solidification. The existence of transparent materials that freeze as metals do provides the opportunity to observe many of the

phenomena during solidification. Jackson and Hunt (Jackson, *et al.* 1965) investigated several transparent materials and obtained quite different interfacial morphologies: a faceted solid/liquid interface in salol, a planar solidification front in carbon tetrabromide, a cellular interface in carbon tetrabromide and a dendritic structure in cycolohexanol.

Somboonsuk and Trivdei (Somboonsuk, *et al.* 1985) used the succinotrile-acetone system to investigate the stability of the dendritic interface in directional solidification. Time-dependent changes in the interface pattern were examined as the pulling velocity was suddenly changed. A hysteresis effect was observed in the interface restabilisation process, and two different mechanisms were found to operate during increase and decrease of the pulling velocity, involving the creation of additional primary dendrites (branching) and the elimination of existing dendrites (overgrowth).

Huang *et al.* (Huang, *et al.* 1993) used succinonitrile-ethanol and studied the effect on the dendritic structure of stepped changes in the pulling velocity. The experimental results showed that a wide permitted range of primary spacing of dendritic arrays exists for given growth conditions; the upper and lower limits of the allowable range are very sharp, and the average primary spacing is remarkably dependent on solidification history. The upper limit, $\lambda_{\max}^{1}$, and the lower limit, $\lambda_{\min}^{1}$, as a function of pulling velocity, V, can be expressed generally as $\lambda_{\max}^{1} = aV^{-b}$ and $\lambda_{\min}^{1} = a'V^{-b'}$, where a, a', b and b' are constant for given alloy and temperature gradient.

Wan *et al.* (Wan, *et al.* 1997) also showed in their experiments on succinonitrile-acetone that the average primary dendrite spacing depends very much on past history. Ma (Ma 2002; Ma 2003) carried out a series of experiments using succinonitrile-acetone to investigate the behaviour of primary dendrite spacing in response to a varying temperature gradient during directional solidification while the pulling velocity remained constant. When the temperature gradient was increased or decreased by a factor of 6, the primary dendrite spacing was found to vary by a factor of 3. After a cycle of variation the temperature gradient was restored to its initial state but the average primary spacing could not return to its original value, revealing an unclosed hysteresis loop for the $\lambda_1 - G$ diagram, as shown in Fig. 2.4 (cycle 1). Continuing the process of changing G, a closed loop will be formed, see cycle 2 in Fig. 2.4.

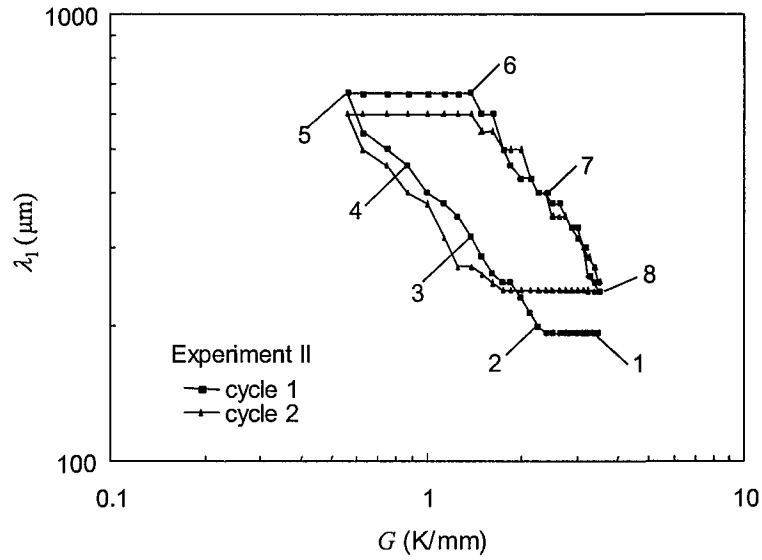

Fig. 2.4 Changes in average primary dendrite spacing in response to the variation in temperature gradient (Ma 2003).

2.2.2 Experiments on Nickel-Based Superalloys

Many experiments have been carried out on nickel-based superalloys. Pollock *et al.* (Pollock, *et al.* 1992) carried out a series of experiments on directional solidification of simple cylindrical bars in which the pulling velocity was fixed but the thermal gradient changed over a wide range. The cooling rate was determined by calculating an average between equilibrium solidus and liquidus temperatures, measured by thermocouples inserted in the moulds. The experimental results showed that the primary dendrite spacing increases from 166 to 686 μm when the cooling rate decreases from 0.77 to 0.01 K/s. Both primary and secondary spacings follow a linear relationship with the cooling rate in logarithmic scale, and such a relationship has also been found in many other experiments (Yu, *et al.* 1992; Zou, *et al.* 1992). The segregation of alloying elements across dendrites was also measured (Zeisler-Mashl, *et al.* 1992; Zou, *et al.* 1992).

Other experiments performed for the directional solidification of nickel-based superalloys also show a fine dendritic structure arising from an increase in pulling

velocity, together with an reduction in both the primary and secondary spacings while the thermal gradient remains roughly constant (Davies, *et al.* 1980; Kermanpur, *et al.* 2000; Wang, *et al.* 2001). When the pulling velocity is increased by a factor of 5, from 35 to 145 μm/s, the primary dendrite spacing is reduced from 153 to 97 μm, and the secondary spacing from 67 to 30 μm (Wang, *et al.* 2001).

Several types of grain defect may develop during directional solidification. Pollock *et al.* (Pollock, *et al.* 1992) investigated the formation of grain defects during the directional solidification of nickel-based single crystals over a wide range of imposed thermal gradients and pulling velocities. Partitioning of refractory alloying elements, such as Re, W and Ta, during solidification leads to the development of convective instabilities which promote freckling and equiaxed grain nucleation through dendrite fragmentation. A complete transition from columnar to equiaxed solidification occurs when the thermal gradient at the solidification front is reduced significantly.

Numerous grain defects were found in experimental castings of single crystal turbine airfoils with complex shapes, including high/low angle boundaries, equiaxed grains and freckles. The formation of misorientated dendrites is related to the contour of the solidification front (Yu, *et al.* 1992).

More experiments will be reviewed in the chapters of results where comparisons are carried out between simulations and experiments.

2.3 Modelling of Solidification

With the advent of powerful computers, advanced numerical methods have been developed for the modelling of microstructure formation and associated characteristics or defects. In recent years, three major contributions have emerged: (1) modelling of solidification processes and microstructural features using averaging methods; (2) modelling of grain structure formation using physically based cellular automata methods; (3) modelling of microstructure formation using phase field methods (Boettinger, *et al.* 2000). All three are important since the macro-scale of a solidification process (typically cm-m), the grain size (typically mm-cm) and the characteristic dimension of the solidification microstructure (typically μm) encompass

six orders of magnitude and cannot be taken into account simultaneously. The main characteristics of the three methods are reviewed in the following sections. Some dendrite tip growth models, which are widely used in cellular automaton models to determine the relationship between tip undercooling and growth velocity, are also reviewed.

2.3.1 Dendrite Tip Growth Models

A theoretical model (KGT model) was proposed by Kurz *et al.* (Kurz, *et al.* 1986) for describing the growth of columnar dendrites. It is assumed that the dendrite has an ideal parabolic shape. Using Ivanstov's solution for the solute transportation problem around the tip, the supersaturation, defined as $\Omega = (C_L - C_0)/[C_L(1-k)]$, can be derived as a function of solutal Péclet number, Pe,

$$\Omega = \mathrm{Iv}(\mathrm{Pe}) = \mathrm{Pe} \cdot \exp(\mathrm{Pe}) \int_{\mathrm{Pe}}^{\infty} \frac{\exp(-u)}{u} \mathrm{d}u, \tag{2.22}$$

and Pe is related to the tip radius, R, and tip velocity, V_{tip}, by

$$\mathrm{Pe} = \frac{RV_{\mathrm{tip}}}{2D_L}. \tag{2.23}$$

When the thermal gradient, G, is assumed to be constant and its effect on the diffusion field around the tip is neglected, R is given by

$$R = 2\pi \sqrt{\frac{\Gamma}{mG_C\xi_C - G}}, \tag{2.24}$$

where G_C is the solute gradient in the liquid at the tip, which can be calculated using a flux balance at the dendrite tip, and ξ_C is also a function of Pe which, at low growth rates, is close to unity.

Kinetic undercooling is neglected, and the total undercooling at the dendrite tip only contains constitutional undercooling and curvature undercooling, expressed as

$$\Delta T_{\mathrm{total}} = \Delta T_C + \Delta T_R = m_l(C_L - C_0) + \frac{2\Gamma}{R} = m_l C_0 \frac{(1-k)\Omega}{1-(1-k)\Omega} + \frac{2\Gamma}{R}. \tag{2.25}$$

Since Ω is related to R and V_{tip}, and the value of R can be calculated from equation (2.24), a relationship between ΔT_{total} and V_{tip} can then be obtained. No simple analytical solution can be derived for this relationship, and the numerical solution can be approximated by a polynomial function:

$$V_{tip} = A_1(\Delta T_{total})^2 + A_2(\Delta T_{total})^3. \tag{2.26}$$

where A_1 and A_2 are two constants related to material properties and surrounding parameters.

The KGT solution showing that the tip velocity is a function of total undercooling, has been validated by experimental measurements (Brown, *et al.* 1994; Koss, *et al.* 1999). It has been widely used in cellular automaton models of grain growth during solidification (Charbon, *et al.* 1993; Ch.-A. Gandin, *et al.* 1996; Q. Y. Xu, *et al.* 2002a; M. F. Zhu, *et al.* 2003).

Hunt and Lu (Hunt, *et al.* 1996) developed an axisymmetric model of cellular and dendritic growth. This model can predict the primary spacing and tip undercooling for both cellular and dendritic structures, and the transition between these two structures as well. The simulation results confirm that dendrite tips do have a parabolic shape.

Kinetic undercooling is also taken as zero in this model, and only constitutional undercooling and curvature undercooling contribute to the total undercooling. The calculated constitutional undercooling can be fitted by a function of dimensionless variables

$$\Delta T_C' = \left(\frac{G'}{V_{tip}'}\right)^c + aV_{tip}'^{\,b} + (1-a)V_{tip}'^{\,1.2b}, \tag{2.27}$$

where the dimensionless undercooling is defined as, $\Delta T' = \Delta T k / [mC_0(k-1)]$, and the coefficients are

$$a = 8.734 + 5.930\log_{10}(k) + 0.2578[\log_{10}(k)]^2, \tag{2.28}$$

and

$$b = 0.4307 - 1.656\times10^{-4}\log_{10}(k) - 4.455\times10^{-2}\left[\log_{10}(k)\right]^2, \quad (2.29)$$

and

$$c = 1.454 + 0.2735\log_{10}(G') + 4.145\times10^{-2}\left[\log_{10}(G')\right]^2 + 1.882\times10^{-3}\left[\log_{10}(G')\right]^3. \quad (2.30)$$

When the equilibrium partition coefficient, k, is less than 1, equation (2.27) approximates to

$$\Delta T_C' = \frac{G'}{V_{\text{tip}}'} + V_{\text{tip}}'^{\,0.333}. \quad (2.31)$$

And the numerical results of curvature undercooling can be fitted with an expression of the form

$$\Delta T_R' = 0.41\left(V_{\text{tip}}' - G'\right)^{0.51}. \quad (2.32)$$

Jackson and Hunt (Jackson, *et al.* 1966) also studied eutectic growth in binary alloy systems. Two solid phases, α and β, are assumed to grow in the form of lamellae perpendicular to the solid/liquid interface. By considering the solute diffusion between the periodic arrangement of lamellae, and the equilibrium of the surface forces at the three-phase junction, the relationship between the growth velocity and undercooling is obtained as

$$V_{\text{tip}} = A\left(\Delta T_{\text{total}}\right)^2. \quad (2.33)$$

where A is coefficient determined by the liquidus slope, surface tension and the ratio of the width of α phase to that of β phase.

2.3.2 Averaging Models

Modelling of solidification processes and microstructural features has benefited from the introduction of averaged conservation equations and the coupling of these equations with microscopic models of solidification. When conservation equations are averaged over the liquid and solid phases, the interfacial continuity condition

automatically vanishes and average entities (e.g. mean temperature or solute concentration) appear.

Rappaz *et al.*(Rappaz, *et al.* 1987b; Rappaz, *et al.* 1987a) proposed a model using averaging methods to predict the growth of equiaxed grains under isothermal conditions. It was assumed that the grain always has a spherical envelope, its average radius, R_g, is demarked by the dendrite tip radius, that the distance between grains are long enough that they cannot 'see' each other and each grain grows freely in a total volume with a radius of R_{tot}, as shown in Fig. 2.5.

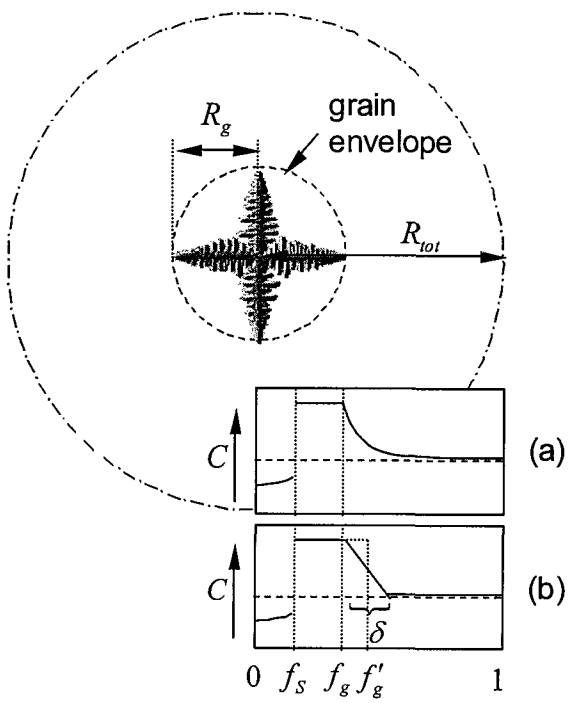

Fig. 2.5 Schematic representation of equiaxed dendritic solidification. One equiaxed grain with a radius of R_g, grows within a total volume of radius, R_{tot}. (a) Concentration profiles based on numerical calculations of the solute diffusion; (b) replacement of solute diffusion by a solute layer of thickness, δ (Rappaz, *et al.* 1987b).

The volume fraction occupied by the grain envelope is simply given by (Rappaz, *et al.* 1987a)

$$f_g = \left(\frac{R_g}{R_{tot}} \right)^3 . \tag{2.34}$$

The grain is not fully solid, and the fraction of solid with respect to the volume of the grain is f_S, and it is related to f_g by

$$f_S = f_i \cdot f_g . \tag{2.35}$$

where the internal fraction of solid, f_i, is supposed to be constant, typically 0.2-0.4, during growth.

Isothermal conditions are applied in the simulations, and a local equilibrium condition is maintained at the dendrite tips. Furthermore, since the curvature undercooling is negligible on this simulation scale, the solid/liquid dendrite interface is an iso-concentrate, C_L^*, whose value can be directly deduced from the equilibrium phase diagram. Considering the balance of heat flow, the dendrite tip velocity, or the rate of the change of the average grain radius, is related to the concentration by

$$\frac{\mathrm{d}R_g}{\mathrm{d}t} = \frac{DmC_0}{\pi^2 \Gamma (k-1)} \left(\frac{C^* - C_R}{C_0} \right)^2 . \tag{2.36}$$

When this equation is solved simultaneously with the diffusion equation using a finite difference method, the growth rate of the equiaxed grain can then be obtained.

In order to simplify the calculation, the solute diffusion can be replaced by a solute layer of thickness, δ, as shown in Fig. 2.5 (b) (Rappaz, *et al.* 1987b). This equivalent layer contains the same total solute content as the exponential profile. After complex algebraic manipulation, the rate of the change of the grain volume fraction is related to the supersaturation (Ω) by

$$\frac{\mathrm{d}f_g}{\mathrm{d}t} = 3A \frac{f_g}{R_g} \cdot \Omega^2 , \tag{2.37}$$

where A is a constant.

This analytical solution permits one to include realistic nucleation laws easily by simply changing the value, $R_{tot}(t)$, which is calculated at each time step from the grain density. Furthermore, such a microscopic model for equiaxed dendritic growth can be incorporated into heat-flow calculations for an entire casting.

Grain structure formation can be modelled successfully with averaging methods. Such methods are particularly suitable when the grain size is small with respect to the scale of the process and/or when only one morphology, either columnar or equiaxed, is present. They are however unable to predict grain competition in the columnar zone and the associated texture evolution, and furthermore cannot provide a representation of the microstructure. The prediction of morphology transitions (from equiaxed to columnar or from columnar to equiaxed (Brown, *et al.* 1989)) is also quite difficult with averaging methods. In order to overcome these shortcomings, cellular automaton models and phase field models have been developed.

2.3.3 Cellular Automaton Models

Cellular Automaton (CA) models are algorithms that describe the discrete spatial and/or temporal evolution of complex systems by applying local, global deterministic or probabilistic transformation rules to the sites of a lattice (Raabe 1998). In a CA model the simulated domain is divided into a grid of cells, and each cell works as a small independent automaton. Variables and state indices are attributed to each cell, and a neighbourhood configuration is also associated with it. The time is divided into finite steps. At a time step, each cell automaton checks the variables and state indices of itself and its neighbours at the last time step, and then decides the updated results at the present step according to the pre-defined transition rules. By iterating this operation with each time step, the evolution of the variables and state indices of the whole systems is obtained.

2.3.3.1 The Monte Carlo Procedure

The Monte Carlo procedure was employed in CA models by Brown and Spittle (Brown, *et al.* 1989) to simulate the stochastic process of grain growth and interaction

during solidification. The domain is divided into a triangular lattice, and a state index is assigned to each lattice site. If the site is liquid, the index is zero, otherwise it has a value greater than zero. And sites belonging to the same grain have the same index values. At each time step, a site randomly selected changes from liquid to solid, and the energy associated with a grain boundary or liquid/solid interface is calculated. If the new energy (H_n) is equal to or greater than the initial value (H_i), the site remains in its original state; otherwise a change in state is imposed. By careful selection of parameters, this model can simulate equiaxed and columnar growth and determine the Columnar-to-Equiaxed Transition (CET). However, the main limitation of the model is that both the nucleation and the grain growth occur at a fixed temperature and the solute redistribution during alloy freezing is not considered. Also the Monte Carlo step is not related to the real time step.

A significant improvement to the previous model was later made by Spittle and Brown (Spittle, *et al.* 1989a) by associating a temperature with each site, and averaging the temperature of every site with its nearest neighbours to calculate the continuous heat loss from the system during freezing. This improvement enabled both the nucleation and growth to proceed in a natural manner according to local conditions.

A further improvement was made by the same authors (Spittle, *et al.* 1989b) to take account of the solute redistribution. On freezing, either by nucleation or capture by a growing grain, the composition of a site changes from C_L to kC_L, and the rejected solute is redistributed to its liquid neighbours.

However, all of the above Monte Carlo procedures are based on hypothetical materials, and a number of important physical materials parameters are not included. A new Monte Carlo method was developed by Zhu & Smith (P. Zhu, *et al.* 1992), which is coupled with continuum heat and solute transfer equations. Not only the interfacial energy but also the bulk free energy is considered. At each time step, a new configuration is accepted with a probability of unity only if the new free energy (F_n) is less than that of the initial value (F_i). Otherwise, the probability is $\exp[-(F_n - F_i)/k_B T]$, where k_B is the Boltzman constant. This algorithm searches for the configuration of lowest free energy. This method solves the heat and solute transfer equations, and a conversion formula was established between the Monte Carlo steps

with the real time. Although different state values of each grain mean they have different orientations, the liquid/solid interfacial energy is assumed to be isotropic, which is actually an average value of the various different orientations, therefore the crystallographic anisotropy cannot be simulated.

Crystallographic anisotropy is a very important characteristic of metallic and alloy materials, and many peculiar solidification phenomena (such competitive growth between differently oriented grains) are related to it. In order to incorporate the effect of the crystallographic anisotropy, considerable effort has been made, and these models, classified by two categories, are presented below,

2.3.3.2 Neighbourhood Selection Algorithm

In CA models, once a cell on the solid/liquid interface becomes solid it captures the neighbouring cells, which then become interface cells. When a regular square grid is used, each cell has four nearest and four second-order nearest neighbours. Through combination of these neighbours, different types of neighbourhood configurations can be defined. As shown in Fig. 2.6, type (a) is the configuration of four nearest neighbours, called a von Neumann neighbourhood (X. Xu, *et al.* 1999); type (b) is the configuration of both four nearest and four second-order nearest neighbours, called the Moore neighbourhood (Yao, *et al.* 2002); type (c) and (d) represent 6-cell left- and right-handed neighbourhoods, respectively (Nastac, *et al.* 1997).

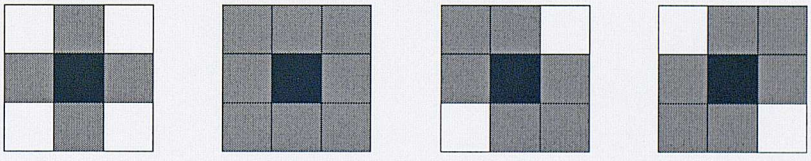

Fig. 2.6 Different types of neighbourhood: (a) 4-cell or von Neumann neighbourhood; (b) 8-cell or Moore neighbourhood; (c) 6-cell left-hand neighbourhood; (d) right-hand neighbourhood (X. Xu, *et al.* 1999).

The selection of different neighbourhood configurations has a direct effect on the grain shape and size. As shown in Fig. 2.7, 4-cell neighbourhoods produce square grains with the fastest growth direction being perfectly aligned with the grid, while 8-cell neighbourhoods still give square grains but its fastest growth direction has a 45° misorientation in respect to the grid. Both 6-cell left-hand and right-hand neighbourhood result in elongated hexagonal grains oriented at 45° with respect to the grid. Combination of 4-cell and 6-cell neighbourhoods can produce grains that have arbitrary misorientation (θ) (X. Xu, *et al.* 1999).

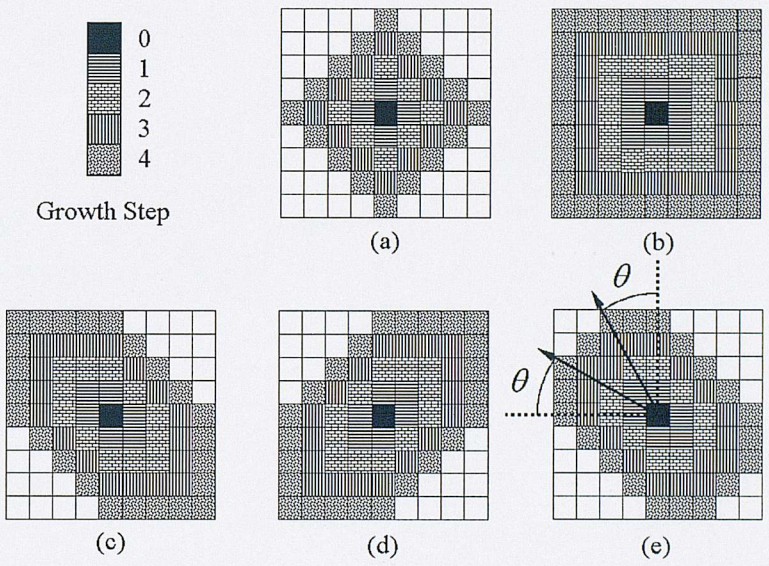

Fig. 2.7 Grain growth direction using different type of neighbourhood: (a) 4-cell, (b) 8-cell, (c) 6-cell left-hand, (d) 6-cell right-hand neighbourhood and (e) combination of 4-cell and 6-cell left-hand neighbourhood (X. Xu, *et al.* 1999).

This neighbourhood selection algorithm has some difficulties: different types of neighbourhood will lead to different occupancy numbers of cells at the same time; combination of different types of neighbourhood has practical difficulty in accounting for grain misorientation of any given angle (θ), since it is impossible to distinguish the two directions indicated by the two arrows shown in Fig. 2.7 (e).

Aware of the artificial anisotropy introduced by a square grid, Beltran-Sanches and Stefanescu (Beltran-Sanchez, *et al.* 2002) proposed a new set of neighbour capturing rules. The neighbourhood is defined as a group of cells centred on the crystallographic growth direction of the dendrite. As shown in Fig. 2.8 (a), the neighbourhood group has 16 cells. After all the cells in the defined neighbourhood around a centre point are solid, a number of new neighbourhoods are captured, becoming interface neighbourhoods. As shown in Fig. 2.8 (b), only the four newly captured neighbourhoods are displayed and the original one is in the back.

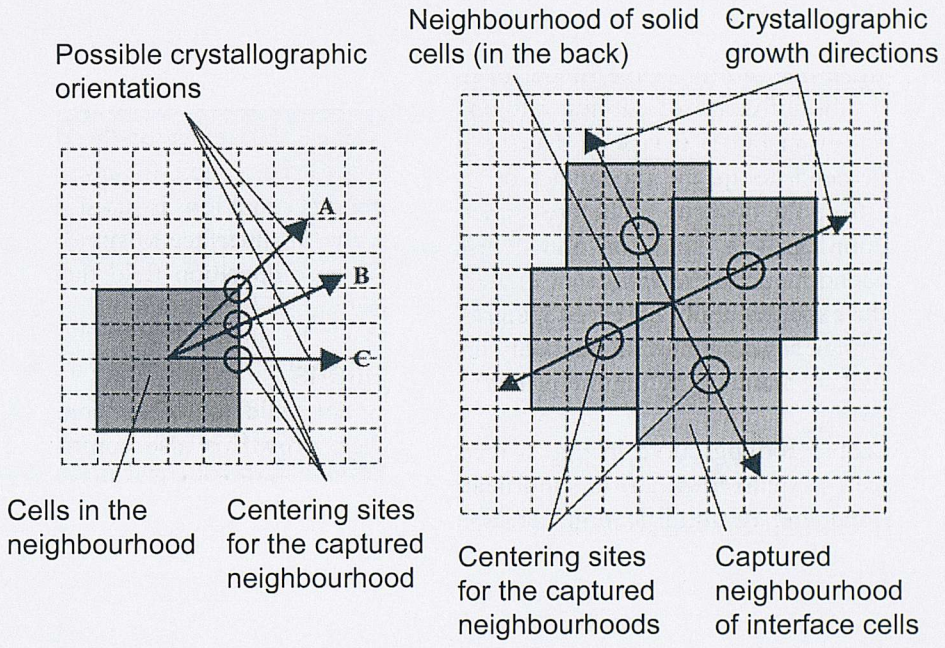

Fig. 2.8 Definition of neighbourhood used for cells capturing during solidification: (a) definition of a neighbourhood around a centre point that enables growth in three possible crystallographic orientations; (b) capturing of four neighbourhoods of interface cells once the original neighbourhood becomes solid for a dendrite growing in the B direction (Beltran-Sanchez, *et al.* 2002).

Theoretically, this definition of a multi-cell neighbourhood is able to reproduce physically realistic growth directions not aligned with the grid axis without arbitrary

corrections. However, it is sometimes not feasible in practice. As shown in Fig. 2.8 (a), the 16-cell neighbouring allows the grain to grow in the three directions: A, B and C. And the orientations for these growth directions are: direction A, $\tan^{-1}(1)$; direction B, $\tan^{-1}(1/2)$, and direction C, 0 (all the angles are in radians). But if any directions other than these are to be simulated, new configurations must be defined. For example to simulate the growth of a grain with a misorientation of $\tan^{-1}(1/100)$ radian (or 0.5°), a neighbourhood composed of 200×200 cells must be used.

In order to tackle the problems of grain growth with arbitrary misorientation with respect to the square grid, a decentred square growth algorithm was developed by Gandin and Rappaz (Ch.-A. Gandin, *et al.* 1997).

2.3.3.3 Decentred Square Algorithm

A 2D square growth algorithm was first introduced by Rappaz & Gandin (Rappaz, *et al.* 1993) to incorporate the crystallographic anisotropy and the growth kinetics of the dendrite tip in modelling grain growth during solidification. This approach was later extended to a 3D octahedron model (Ch.-A. Gandin, *et al.* 1993; Ch.-A. Gandin, *et al.* 1994b; Ch.-A. Gandin, *et al.* 1995). The 2D square algorithm cannot be easily adapted to situations of non-uniform temperature; it was modified to a 2D rectangular algorithm (Ch.-A. Gandin, *et al.* 1994a; Ch.-A. Gandin, *et al.* 1996). But the 2D rectangle algorithm is difficult to extend to 3D as the rectangular configuration would correspond to non-regular octahedral shapes, and for this reason, a 2D decentred square algorithm and its extension to 3D, the decentred octahedron algorithm, were finally developed (Ch.-A. Gandin, *et al.* 1997).

These models were developed for simulating growth of crystals that have four-fold symmetry (i.e. cubic metals). One of the basic assumptions in these algorithms is that, the growth velocity along the <100> directions is always $\sqrt{2}$ times that along the <110> directions. Hence, the grain will always grow into a square shape under isothermal condition. Under non-isothermal conditions, the growth velocity along different <100> directions could be different, but these fastest growth directions must be retained.

At the beginning of the simulations, all the cells start with a 'liquid' state. Through nucleation, some cells change into a 'solid' state. In the decentred square algorithm, a small square is then associated with each 'solid' cell. Then the solid growth is represented by enlargement of these squares. The KGT solution (Kurz, *et al.* 1986) is used to decide the growth rate. The half size of the 'growing' square at a time t is given by

$$L^t = L^0 + \frac{1}{\sqrt{2}} \int_{t_N}^{t} v[\Delta T(\tau)] \mathrm{d}\tau , \tag{2.38}$$

where t_N is the time when a nucleus forms or the cell is captured by a growing grain, ΔT is the undercooling at the cell centre. For nucleation, the initial length L^0 is set to zero. For cell capture it is decided by the relative position of the cell centre and the capturing square.

In a time-stepping calculation, from time t-δt to time t, the square envelope centred on C_ν captures the neighbouring cell μ, or the corresponding square of size L^t_ν has engulfed the cell centre μ, as shown in Fig. 2.9. Cell μ is then set to a 'solid' state by changing its state index to that of cell ν (in fact it is mushy, but, since diffusion is not solved, a cell only has two states, either 'liquid' or 'solid'). A new square is then associated with cell μ, and it is generated in such a way that it has the identical orientation of the one centred on C_ν, with one corner overlapping it, or, by shifting the centre of the old square along [100] direction from C_ν to C_μ, and reducing the size correspondingly (see Fig. 2.9).

If all the neighbours of cell ν have been captured by the square centred on C_ν, the growth of this square is finished, and from this time onwards, the growth of the square centred on C_μ then continues to capture more neighbours of cell μ. The growth of grains is represented by the successive growth of small squares associated with each cell, with the diagonals of each square oriented parallel to the <100> directions of a grain.

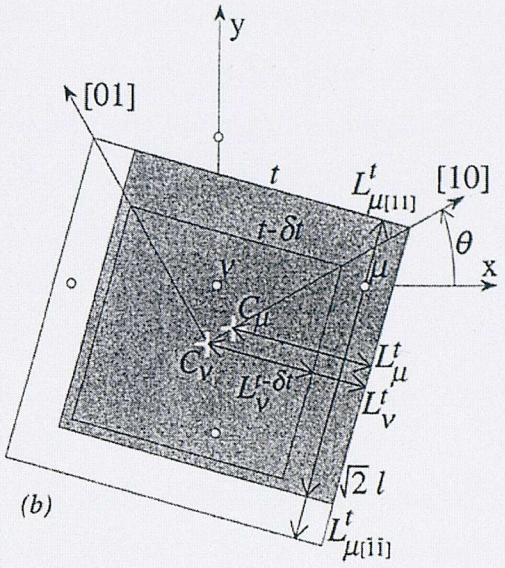

Fig. 2.9 Schematic diagram of 2D decentred square CA algorithm. For cubic metals, it is assumed the grain always grows into a square envelope. The square associated with cell ν, the half size of which is L_ν, is misoriented to the coordinates by an angle of θ. When the square grows big enough to touch the centre of its neighbouring cell μ, it is said that cell μ is captured, and a new square is associated with it. The new square is located inside the original square and is shifted toward the corner that is nearest to the centre of cell μ (Ch.-A. Gandin, *et al.* 1997).

These three algorithms (square, rectangle and decentred square) are all based on regular square grids. Although cellular automaton models can run on regular triangular (Brown, *et al.* 1989) or hexagonal grids (P. Zhu, *et al.* 1992), for crystals with four-fold symmetry a square grid is more convenient. A quite large grid size can be used when the solute diffusion and/or heat diffusion is not solved. The grid size used by Gandin and Rappaz (Ch.-A. Gandin, *et al.* 1994a) in the simulation of directional solidification of an organic alloy, coupled with the heat diffusion equation, varies between 24 and 141 μm; while in simulation of grain growth under Bridgman conditions, the grid size may go up to 300 μm (Ch.-A. Gandin, *et al.* 1997).

The 2D square algorithm is capable of simulating the selection and extension of columnar grains, and CET, under uniform temperature conditions (Rappaz, *et al.* 1993). The 2D rectangle and decentred square algorithm have broken the restriction of isothermal condition. They can simulate equiaxed grain growth or Directional Solidification under Bridgman conditions (Ch.-A. Gandin, *et al.* 1996); or coupled with Finite Element (FE) heat flow calculation, they can deal with more realistic thermal conditions (Ch.-A. Gandin, *et al.* 1994a). A 3D CA-FE model was also applied for the prediction of solidification grain structures in single crystal turbine blades (Desbiolles, *et al.* 1998; Ch. -A. Gandin, *et al.* 1998). These algorithms can predict the maximum growth envelope and keep the original misorientation of grains. However, since none of them solves the solute diffusion equation, therefore, they are not able to simulate the complex dendrite initiation and growth induced by solute diffusion.

2.3.4 Phase Field Models

An alternative technique for investigating solidification is the phase field method. Phase field models were firstly developed for simulating equiaxed growth under isothermal conditions (Braun, *et al.* 1994; Warren, *et al.* 1995). A desirable extension of the model was to study the effect of heat flow due to the release of latent heat. A simplified approach was proposed in which the temperature was assumed to remain spatially uniform at each instant, and a global cooling rate was imposed with consideration of the heat extraction rate and increase of the fraction of solid (Boettinger, *et al.* 1996). The attempt to model non-isothermal dendritic solidification of a binary alloy was made by Loginova *et al.* by solving both the solute and heat diffusion equations and considering the release of latent heat as well (Loginova, *et al.* 2001).

Besides equiaxed growth in the supersaturated liquid, the phase field model was also applied to the simulation of directional solidification, under well-defined thermal conditions (Boettinger, *et al.* 1999; H.-J. Diepers, *et al.* 2002). The phase field model has also been used to simulate the competitive growth between grains with different misorientation with respect to the thermal gradient (Tiaden, *et al.* 1999).

Further development in phase field models includes the extension into three dimensions (Karma, *et al.* 1996; Steinbach, *et al.* 1998a; Steinbach, *et al.* 1998b), and

multi-component systems (Steinbach, *et al.* 1996; Tiaden, *et al.* 1998). Usually a regular grid composed of square elements is used in the phase field models (Warren, *et al.* 1995; Boettinger, *et al.* 1996), but an unstructured mesh composed of triangular elements is also used (Provatas, *et al.* 1998), which enables the phase field method to be applicable in a domain with complex geometry shape and also in a large scale.

From a physical point of view, the phase field method requires knowledge of the physical nature of the liquid-solid interface. However, little is known about its true structure. Using Lennard-Jones potentials, molecular dynamics simulations of the transition in atomic positions across an interface have suggested that the interface width extends over several atomic dimensions (Broughton, *et al.* 1981). At present, it is difficult to obtain usable simulations of dendritic growth with interface thickness in this range due to the limitations of computational resources. Thus the interface width will be a parameter that affects the results of the phase field method. It should be realized that in the limit as the interface thickness approaches zero the phase field equations converge to the sharp interface formulation (Wheeler, *et al.* 1992; Caginalp, *et al.* 1993).

In contrast to CA models which adopt a pseudo-front-tracking technique, phase field models express the solid/liquid interface as a transitional layer which usually spreads over several cells. A phase field variable, ϕ, is defined in the simulation domain. It has a value of 1 in the solid and 0 in the liquid, and varies in a smooth, continuous manner in the transitional solid/liquid layer (Warren, *et al.* 1995; Loginova, *et al.* 2001). Using a free energy (Wheeler, *et al.* 1992; Ahmad, *et al.* 1998) or entropy (McFadden, *et al.* 1993; Warren, *et al.* 1995) formulation, two equations governing the evolution of solute concentration and the phase field variable can be derived.

The moving velocity of the solid/liquid interface, V_n, is related to the changing rate of ϕ by

$$V_n = \frac{\dot{\phi}}{|\nabla \phi|}. \tag{2.39}$$

Constitutional undercooling, curvature undercooling and kinetic undercooling are all taken into consideration when calculating the velocity. A rate equation for the phase field variable can then be obtained (Diepers, *et al.* 1998)

$$\dot{\phi} = \frac{\mu\sigma}{\Delta s_f}\left\{\nabla^2\phi - \frac{[(\nabla\phi)\nabla]|\nabla\phi|}{|\nabla\phi|}\right\} + \mu\left[T_{liq}^0 + m_l(C_L - C_0) - T_{\text{int}}\right]|\nabla\phi|. \qquad (2.40)$$

where μ the kinetic coefficient, σ the surface energy, and m_l the liquidus slope.

Equation (2.40) does not have a unique solution for a stationary front profile problem; hence this profile has to be specified separately. A convenient choice of the profile is given by the following function

$$\phi = \frac{1}{2}\left(1 - \tanh\frac{3x}{\delta}\right), \qquad (2.41)$$

where x is the coordinate normal to the interface and δ is the interface thickness, defined by condition of $0.05 < \phi < 0.95$.

Substituting equation (2.41) into (2.40), the rate equation for the phase field becomes (Diepers, *et al.* 2002)

$$\dot{\phi} = \frac{\mu\sigma}{\Delta s_f}\left\{\nabla^2\phi - \frac{36(1-2\phi)(1-\phi)\phi}{\delta^2}\right\} + \mu\left[T_{liq}^0 + m_L(C_L - C_0) - T_{\text{int}}\right]\frac{6\phi(1-\phi)}{\delta}. \qquad (2.42)$$

The effect of the crystallographic anisotropy on the solidifying interface is known to enter the liquid/solid interfacial energy, as well was the interfacial mobility. This anisotropy can be introduced in equation (2.42) by replacing σ with $\sigma(\theta)$,

$$\sigma(\theta) = \sigma_0\left[1 - \varepsilon_{\text{st}}\cos(n\theta)\right], \qquad (2.43)$$

where ε_{st} is the amplitude of surface energy anisotropy, and θ the angle between the crystallographic direction and the interface normal (Krumbhaar, *et al.* 1991), and replacing μ with $\mu(\theta)$,

$$\mu(\theta) = \mu_0\left[1 + \varepsilon_{\text{kin}}\cos(n\theta)\right], \qquad (2.44)$$

where ε_{kin} is the amplitude of anisotropy of mobility. For crystals with four-fold symmetry, n is 4; while for those having six-fold symmetry, n is 6 (Kobayashi 1993).

Compared to CA models, phase field models require a much smaller cell size. Warren and Boettinger (Warren, *et al.* 1995) used a cell size of 0.046 μm. Similar cell size was used by Semoroz *et al.*(Semoroz, *et al.* 2000), Δx = 0.05 μm. The value of cell size used by Loginova *et al.* (Loginova, *et al.* 2001) varies between 0.0023 and 0.052 μm. Diepers used a much larger cell size in his simulations, Δx = 2 μm (H.-J. Diepers, *et al.* 2002), but still could produce reasonably good dendritic structures.

2.3.5 Comparison between Different Models

Some simulation results of the averaging models, cellular automaton models and the phase field models are shown in this section for comparison.

Fig. 2.10 shows the simulation results using the averaging model by Rappaz *et al.* (Rappaz, *et al.* 1987a). Cooling curves, grain fraction and solid fraction for two nucleation undercoolings (i.e. A: 0 K, B: 2 K), are shown in this figure. The temperature drops down quickly before nucleation, then increases as nucleation starts, and finally drops down again after solidification process is finished. The prediction of recalescence agrees well with experimental measurements.

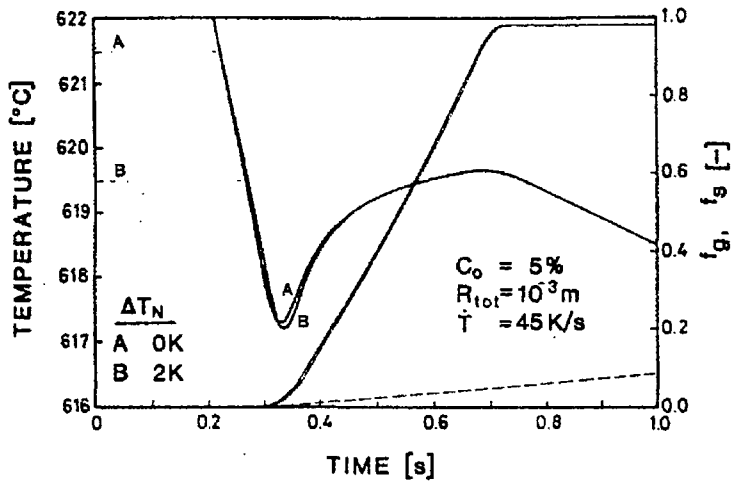

Fig. 2.10 Simulation results of deterministic model (Rappaz, *et al.* 1987a). Cooling curves, grain fraction and solid fraction for two nucleation undercoolings are shown in this figure.

Fig. 2.11 (a), (b), (c) and (d) are the CA simulation results of grain growth by choosing different types of neighbourhood configurations (Nastac, *et al.* 1997). It shows that the selection of different neighbourhood configurations has a direct effect on the final grain patterns.

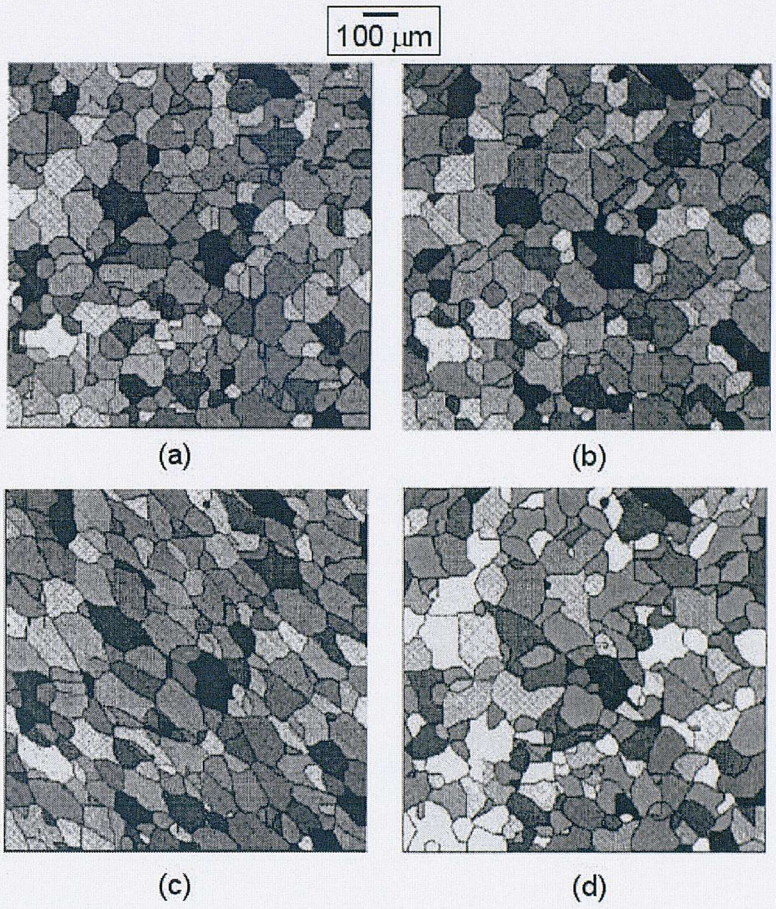

Fig. 2.11 CA Simulation results of grain growth by choosing different types of neighbourhood. Results (a), (b) and (c) are the simulation results by using the 4-cell, 8-cell and 6-cell left-hand neighbourhood configurations shown in Fig. 2.6. Result (d) is the result of random combination of these three types of neighbourhood configurations (Nastac, *et al.* 1997).

Fig. 2.12 (a) and (b) show the analytical and numerical predictions of the evolution of the envelope of a single grain growing in a Bridgman condition, using the 2D CA decentred square algorithm developed by Gandin *et al* (Ch.-A. Gandin, *et al.* 1997). The numerical predictions agree well the analytical results.

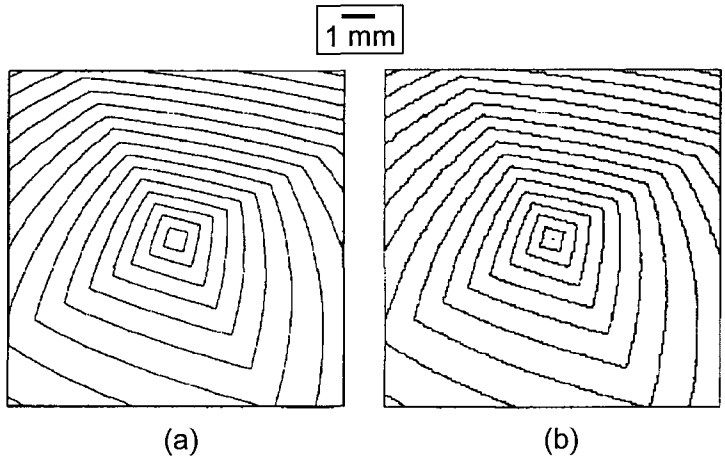

Fig. 2.12 Analytical (a) and Numerical predictions (b) using the 2D CA decentred square algorithm, of the evolution of the envelope of a single grain growing in a Bridgman condition. The grain envelope are drawn every 1s from the time of nucleation. The grain has a misorientation of 30°. KGT model is used to calculate the growth velocity. The parameters used in this simulation are referred to (Ch.-A. Gandin, *et al.* 1997).

Fig. 2.13 shows the phase field simulation of the microstructure of an equiaxed grain growing under isothermal condition. Both primary and secondary dendrites are clearly shown in the figure. The secondaries growing from different primary arms impinge into each other. The solute concentration is also shown in the figure. The concentration between secondary dendrites is much higher than in the solid.

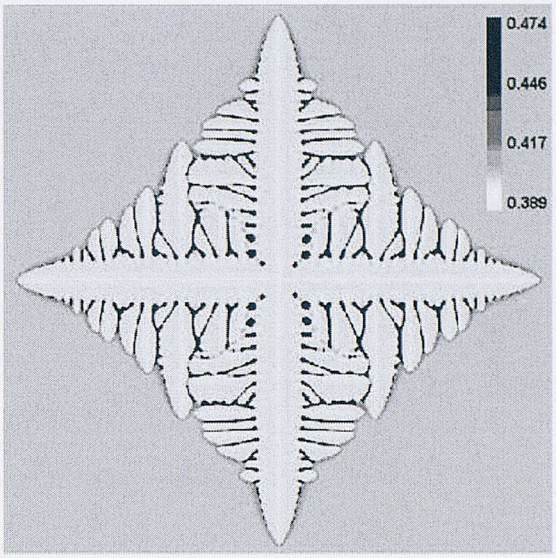

Fig. 2.13 Simulation of equiaxed growth under isothermal condition by the phase field method. Dimensionless parameters were used in the simulations (for details refer to (Loginova, *et al.* 2001)). A domain composed of 750×750 square cells was used in the simulations. The legend at the top-right corner shows the dimensionless concentration.

The averaging model is capable of tracking the evolution of the macro-scale or average variables, e.g. average temperature and the total fraction of solid, but it cannot simulate the structure of grains. The CA models can simulate the macro-scale and meso-scale grain structures, but it has difficulty to resolve the microstructure. The phase field method can well reproduce the microstructure of dendritic grains. However, with the current computational power, phase field models can only work well on a very small scale (up to hundreds of μm). The typical scale of laboratory experiments is 1 cm, and the scale of an industry problem can be up to 1 m. Both of them are beyond the capability of the phase field method. Therefore, a novel combination of these models should be developed. A combined CA-FD model with a novel adaptation of modified decentred square growth algorithm was developed during the course of this study, and is presented in the next chapter.

Chapter 3

Modelling Theory

A micro-scale model that combines a Cellular Automaton (CA) description of grain nucleation and growth with a Finite Difference (FD) computation of solute diffusion has been developed during the course of this study. Both the CA and FD components of the model run on the same regular spatial square grid and with the same time step. Each spatial cell represents a small amount of materials, and can have three states: liquid, solid and 'growing' (i.e. a mixture of liquid and solid). A real time scale is adopted in the model so that the numerical predictions can be compared directly with experimental observations.

The model begins with all the cells in a liquid state, and continues with nucleation and growth within and across cells. The cells may transform from liquid to the 'growing' state by a nucleation event. A 'growing' cell may 'melt' back to liquid state if the thermal condition is unfavourable for its growth, or start to grow if the condition is in favour. A 'growing' cell can 'capture' its neighbouring liquid cells, and will stop growing when it becomes fully solid.

In order to account for the crystallographic anisotropy of cubic metals, the decentred square/octahedron (in 2D/3D respectively) growth and cell 'capture' algorithm, firstly developed by Gandin and Rappaz (Gandin, *et al.* 1997), has been adopted and developed in this model.

Solute partitioning occurs in a 'growing' cell, where liquid and solid coexist, when the equilibrium coefficient is not equal to 1. When the equilibrium coefficient is less than 1, the extra solute will be rejected from the liquid and accumulate in front of the solid/liquid interface. Through diffusion, the accumulated solute can be transported to neighbouring cells, while a dynamic balance is maintained in the 'growing' cells. When the equilibrium coefficient is greater than 1, a solute depleted region will form in front of the interface, and the direction of solute diffusion is reversed.

In this chapter, the nucleation and growth of solid within a CA framework and the solute diffusion solved with FD method is described in turn.

3.1 Model Assumptions

The model was designed to simulate the process of nucleation and growth during the transformation from liquid to solid phase in a binary alloy system, and was based on several simplifying assumptions: no latent heat, linearised phase diagram, and constant diffusivity in both liquid and solid phases.

The problems of interest in the current study are to investigate the development of the solute diffusion controlled dendritic microstructures, the scale of which is about 10~1000 μm. Since the diffusivity of heat is usually several orders higher than that of solute, it will not introduce significant error to assume that the heat diffusion has reached an equilibrium state at the scale of dendrites. Instead of solving the heat diffusion equation and considering the release of latent heat, simple and well-defined thermal conditions are usually applied in CA models to facilitate the computation. In the current model Bridgman growth conditions are applied in the simulations of directional solidification, with a schematic illustration shown in Fig. 3.1: horizontal isotherms with a fixed gradient, G, are moving up at a constant velocity, V, giving a uniform cooling rate, $\dot{T} = G \cdot V$, in the whole simulation domain. At time t_0 the position of the liquidus T_{liq}^0 isotherm is given by an equation $y = y_0$; since it is moving up at a constant velocity of V, its position at time t is then given by $y = y_0 + V \cdot t$. Thus the thermal history at any point in the domain is then fully determined; for example, at a cell centre with coordinates of (x_i, y_j), the temperature at time t is given by

$$T_{ij}(t) = T_{liq}^0 + G \cdot (y_j - y_0 - V \cdot t). \tag{3.1}$$

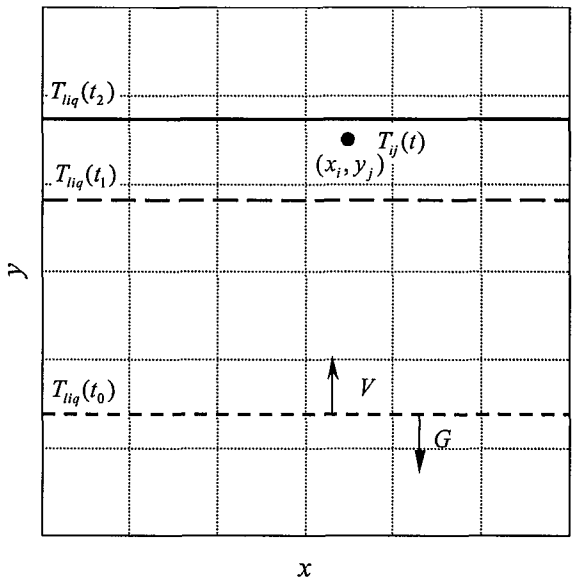

Fig. 3.1 Schematic illustration of the temperature field.

As shown in Fig. 3.1, at time t_1, the cell centre (x_i, y_j) is still above the liquidus isotherm, $T^0_{liq}(t)$, the temperature at centre is above the liquidus; but at time t_2 the liquidus isotherm has passed the centre, thus its temperature becomes below the liquidus, or it is at a undercooled state.

Fig. 3.2 is a schematic illustration of the linearised phase diagram of a binary alloy system A-B at the element A rich end. Both the liquidus and solidus are straight lines. The slope of the liquidus is m_l, and that of the solidus is m_s, and the ratio of them is defined as the equilibrium partition coefficient, $k = m_l / m_s$, which is constant in this case.

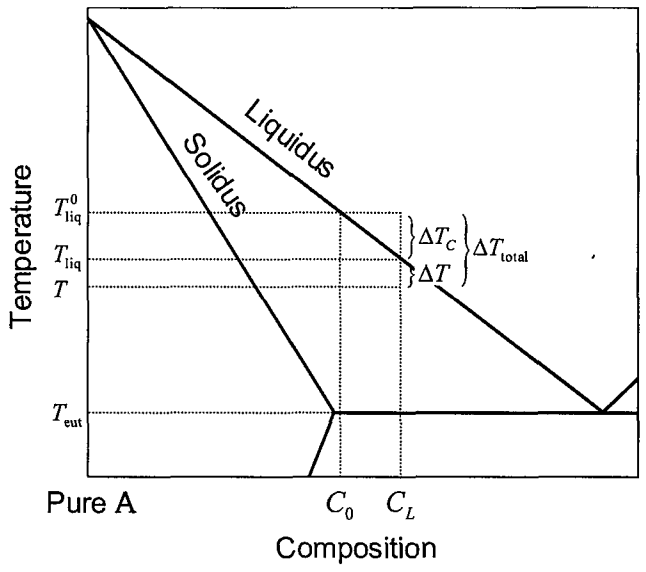

Fig. 3.2 Schematic illustration of the linearised phase diagram of a binary alloy system.

At the beginning of the simulations all the cells have the identical initial concentration, C_0, and the corresponding liquidus temperature is T^0_{liq}. When the temperature in a cell drops below the initial liquidus, it becomes undercooled. If a nucleus forms in this cell, according to the phase diagram, the concentration in the solid grain is $k \cdot C_0$. The rejected solute will be transported to the neighbouring cells by diffusion.

In this figure the liquidus has a negative slope, m_l, or the liquidus temperature, T_{liq}, decreases when concentration of element B, C_L, increases. Then the real undercooling, ΔT, is calculated by

$$\Delta T = \Delta T_{total} - \Delta T_C = T^0_{liq} + \frac{1}{m_l}(C_L - C_0) - T, \tag{3.2}$$

where ΔT_{total} is the total undercooling, ΔT_C the constitutional undercooling, C_0 the initial concentration and T^0_{liq} the liquidus at C_0. The calculated undercooling will be used when considering random nucleation process.

It is necessary to point out that the linearised approximation is only applicable when the concentration and temperature are within a certain range. Furthermore, because eutectic growth has not been incorporated yet, the model can only work properly above eutectic temperature.

One of the results of the linearisation of phase diagram is that the equilibrium partition coefficient, k, becomes independent of concentration, which will make it easier for programming. Another important simplification made to the model to facilitate programming is that diffusion coefficients in liquid and solid phases, D_L and D_S, were assumed to be independent of either concentration or temperature.

Latent heat is not considered in the model, because the micro-scale dendritic structure is more affected by diffusion of solute rather than heat. The diffusion coefficient of heat is usually several orders higher than that of solute, thus it is reasonable to assume an equilibrium condition has been reached in the thermal field at the dendritic tips. The model can deal with isothermal or constant temperature gradient conditions.

3.2 Nucleation

Two types of nucleation have been incorporated into the model: pre-determined nucleation at specific conditions and random nucleation. Pre-determined nucleation is usually used in test numerical runs to verify the model, or in simulations beginning with specified initial conditions. At the beginning of simulations, a few seed grains are specified in some cells with a temperature below the liquidus, or in other words, the state indices of these cells are assigned as 'growing', and the fraction of solid set to a small positive value. Although this nucleation process is not physically justified, it is useful when debugging programs, or in carrying out simulations with specified initial conditions, e.g. simulations of the growth of columnar dendrites with a specified primary dendrite spacing.

Unlike pre-determined nucleation, random nucleation is determined stochastically, representing the statistical and random process of generating nuclei in practice. This nucleation process requires a certain degree of undercooling, and the nucleation rate also depends on undercooling.

A Gaussian distribution is used to describe the grain density increase, $dn/d(\Delta T)$, which is induced by an increase in the undercooling, $d(\Delta T)$, and it is expressed as (Thevoz, *et al.* 1989; Gandin, *et al.* 1993)

$$\frac{dn}{d(\Delta T)} = \frac{n_{max}}{\sqrt{2\pi}\Delta T_\sigma} \exp\left[-\frac{(\Delta T - \Delta T_N)^2}{2(\Delta T_\sigma)^2} \right], \tag{3.3}$$

where ΔT_N is the mean nucleation undercooling, ΔT_σ the standard deviation of the distribution and n_{max} the maximum nucleation density. Therefore the total density of grains, $n(\Delta T)$, which have been nucleated at a given undercooling, ΔT, is given by the integral of this distribution (Rappaz, *et al.* 1993):

$$n(\Delta T) = \int_0^{\Delta T} \frac{dn}{d\tau} d\tau . \tag{3.4}$$

During one time-step of CA method the undercooling in a cell increases an amount, $\delta(\Delta T)$, and accordingly, the density of new grains nucleated is given by (Rappaz, *et al.* 1993)

$$\delta n = n[\Delta T + \delta(\Delta T)] - n(\Delta T) = \int_{\Delta T}^{\Delta T + \delta(\Delta T)} \frac{dn}{d\tau} d\tau . \tag{3.5}$$

The grain density increment, δn, multiplied by the volume of the cell, V_{CA}, gives the probability of nucleation in a cell, p, during the time step (Rappaz, *et al.* 1993)

$$p = \delta n V_{CA} . \tag{3.6}$$

A random number, r, is generated for each cell ($0 \le r < 1$), and nucleation will occur in the cell only if the following condition is satisfied:

$$r \le p . \tag{3.7}$$

The probability that a nucleus forms in a cell is affected by the undercooling in that cell through a deterministic relationship, but whether the nucleus does form or not is decided by generating a random number, which is stochastic.

Through either pre-determined or random nucleation, if a cell effectively transforms from the liquid to the 'growing' state, a grain number is then associated with it and the fraction solid in it is changed from zero to a small positive value. The nucleated grain could either melt back into liquid if the temperature in that cell increases well beyond liquidus later, or start to grow if the thermal condition is in favour of its growth.

3.3 Diffusion Controlled Growth

Since the model has been used to investigate the diffusion-controlled growth of dendritic grains, solute diffusion and grain growth are interlaced, and thus are described together in this section.

3.3.1 Diffusion Analysis

Solute diffusion is calculated by solving the diffusion equation on a two-phase domain with a moving solid/liquid boundary. The continuous concentration distribution is discretised upon the CA network; a one-dimension schematic is shown in Fig. 3.3.

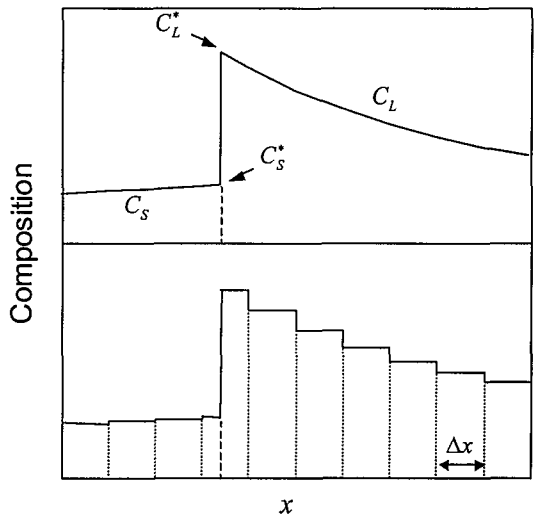

Fig. 3.3 A schematic illustration of discretisation of the solute distribution profile upon a one-dimensional CA grid.

Assuming the partition coefficient (k) is less than unit, and the solid/liquid interface is moving from left to the right. The solute is partitioned at the interface, where the solid in liquid is C_L^* and that in solid is C_S^*. Since the partition coefficient (k) is a constant, their relationship can be expressed as

$$C_S^* = kC_L^*. \tag{3.8}$$

The x-axis is divided into a number of small sections (or cells), with a uniform size of Δx. The solid/liquid interface is in the fourth cell, which is called the 'growing' cell. All the cells to the left are fully solid, and those to the right are purely liquid. In a purely solid or liquid cell there is only one phase and the average concentration is presented either as C_S or C_L. But in the 'growing' cell solid and liquid phases coexist, and the average concentration is calculated as

$$C^* = C_L^*(1-f_S) + C_S^* f_S = C_L^*\left[1-(1-k)f_S\right], \tag{3.9}$$

where f_S is the fraction of solid in the 'growing' cell.

If an equivalent concentration in liquid, C_L, is defined for those solid cells, which satisfies the following requirement,

$$C_S = kC_L, \tag{3.10}$$

the definition of average concentration in 'growing' cell can also be extended to other purely solid or liquid cells as

$$C = C_L\left[1-(1-k)f_S\right]. \tag{3.11}$$

When f_S is zero, C equals C_L; when f_S is unit, C equals C_S.

A general diffusion equation in the liquid and solid phases, as well as across the solid/liquid boundary, can then be derived as

$$\frac{\partial C}{\partial t} = \nabla\cdot\left(D\nabla C_L\right), \tag{3.12}$$

where D is defined as

$$D = D_L(1 - f_S) + kD_S f_S . \tag{3.13}$$

It is noticed that only ∇C_L appears in the right-hand side of equation (3.12). In the solid phase where f_S is one, D equals kD_S, and the term in bracket at right-hand side of equation (3.12) becomes $D_S k \nabla C_L$, which is equal to $D_S \nabla C_S$ (since k is constant).

By solving the general diffusion equation (3.12) using an explicit finite difference method, the rate of the change of concentration in each cell can then be obtained. However, in the 'growing' cell, the rate of the change of fraction solid has yet been decided. Equation (3.9) can be transformed into

$$\frac{\partial f_S}{\partial t} = \frac{1}{C_L^*(1 - f_S)}\left[-\frac{\partial C^*}{\partial t} + [1 - (1-k)f_S]\frac{\partial C_L^*}{\partial t}\right]. \tag{3.14}$$

It is assumed that a local equilibrium condition is always maintained at the solid/liquid interface. Thus the concentration of liquid at the solid/liquid interface (C_L^*) can be derived from the equilibrium phase diagram. When such a linearised phase diagram as that in Fig. 3.2 is used, since the kinetic undercooling is neglected in the model, the real undercooling at the interface (ΔT) must equal zero, and the concentration in the liquid at the interface can then be derived as

$$C_L^* = C_0 - \frac{T_{\text{liq}}^0 - T}{m_l}. \tag{3.15}$$

By adding a small modification to equation (3.15) the effect of interfacial curvature can also be included:

$$C_L^* = C_0 - \frac{1}{m_l}\left[T_{\text{liq}}^0 - T - \Delta T_R\right] = C_0 - \frac{1}{m_l}\left[T_{\text{liq}}^0 - T - \Gamma\kappa\right], \tag{3.16}$$

where ΔT_R is curvature undercooling, Γ the Gibbs-Thomson coefficient, and κ the average curvature of the solid/liquid interface, which is calculated by an approximate method described by Nastac (Nastac 1999)

$$\kappa = \frac{1}{\Delta x}\left\{1 - \frac{2}{N+1}\left[f_S + \sum_{j=1}^{N} f_S^j\right]\right\}, \tag{3.17}$$

where N is the number of neighbouring cells taken into account. The values of κ calculated with the above equation vary from a maximum of $1/\Delta x$ to zero for convex surfaces, and from zero to a minimum of $-1/\Delta x$ for concave surfaces.

It needs to be pointed out that the curvature calculated by equation (3.17) is not very accurate. But for dendrites growing at high velocities, the curvature undercooling is much smaller than the constitutional undercooling; hence such approximation can still produce reasonable results.

After the variation of concentration in the 'growing' cell is determined by equation (3.12), by solving equation (3.14), the rate of change of the solid fraction in the 'growing' cells can be calculated, with the consideration of the effect of both solute diffusion and interfacial curvature. This diffusion analysis can easily be extended into two- and three-dimensions.

3.3.2 Growth Algorithm

The 2D/3D decentred square/octahedron algorithm developed by Gandin and Rappaz (Gandin, *et al.* 1997) is not directly applicable for simulating grain growth from the liquid when solute diffusion is considered. In order to solve the diffusion equation, the solid fraction within cells must be allowed to change continuously and smoothly from 0 to 1 if numerical instabilities are to be avoided. The KGT solution (Kurz, *et al.* 1986) that shows the growth velocity to have a power-law relationship to the total undercooling is no longer appropriate since it can only predict the growth velocity of dendrite tips, but not the whole solid/liquid interface. Therefore, a novel modified 2D/3D decentred square/octahedron growth algorithm, has been developed to overcome these problems. Details are presented below.

A schematic illustration of the modified 2D decentred square growth algorithm is shown in Fig. 3.4. Only nine cells of a whole CA network are displayed for clarity. A grain with misorientation angle, θ, has nucleated at the central cell and is growing in a

square shaped envelope. The increment of the half width of the square is related to the increment of fraction solid by:

$$\Delta L = \Delta x \cdot \Delta f_S . \tag{3.18}$$

When the misoriented square envelope associated with the solid in the central cell touches its four neighbouring cells, their state indices will be changed from 'liquid' to 'growing' as that of the original. In each of these 'touched' neighbouring cells, a new square is created with the same orientation as the solid cell that grew into it. One corner of each of the new squares overlaps the original square, hence the term "decentred square" method. The growth velocities of these new squares can be different from the original square depending on the solute diffusion or local temperature. Parts of the growing new squares are shown in Fig. 3.4 (b). The misoriented solid squares progressively encroach on more reference cells, as illustrated in Fig. 3.4 (c).

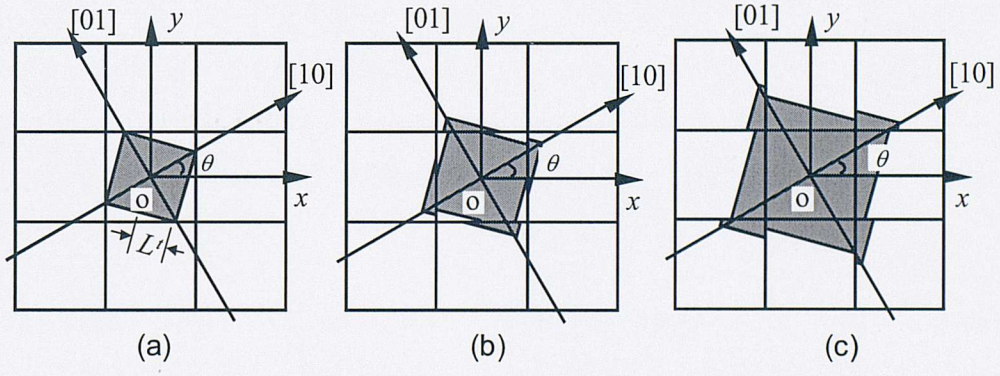

Fig. 3.4 Schematic of the modified 2D decentred square algorithm. A grain that has a misorientation angle θ, is nucleated at the central cell. When it grows big enough to touch the side of neighbouring cells, it is said that they are captured, and newly generated squares are associated with them. Only the overlapped parts of the squares and corresponding cells are shown in the picture.

The 2D modified decentred square growth technique was also extended into three dimensions, termed the 3D modified decentred octahedron growth technique. The underlying approach is the same. A misoriented grain is considered to nucleate and grow within a regular array of cubic cells having an octahedral shape. When the solid grows along one of the crystallographic cube directions to touch any of the six neighbouring cubic cells, growth continues from that point along <100> directions into the captured cells by generating a new octahedron. Shifting the original octahedron along the diagonal towards the corner point that touches the neighbouring cell generates the new octahedron that can keep growing along the same <100> directions as the nuclei.

Thus, constitutional and curvature undercooling, together with crystallographic orientation, are all incorporated in the model through the application of this modified decentred square/octahedron technique within a CA-FD framework.

3.4 Boundary Conditions

The 2D model runs on a regular square grid, and the initial and boundary conditions need to be defined for this domain. Usually simulations start with conditions that all the cells are in a liquid state and have a uniform initial concentration. Two types of boundary conditions are most often used: periodic boundary condition and zero-flux boundary condition.

Again a 9- cell domain is taken as an example to illustrate how boundary conditions are incorporated in the simulation domain, as shown in Fig. 3.5 (a). Periodic boundary conditions are applied to the sides A-B and C-D, while zero-flux boundary conditions are placed at the sides A-D and B-C. During the run of the program, a temporary buffer array, the size of which is bigger than the original domain, is then generated in the following two steps: (i) 'copy' the left row of cells and 'paste' them to the right of the original domain, and 'copy' the right row and 'paste' to the left of the original domain; a 5×3 cell domain is then obtained, as shown in Fig. 3.5 (b); (ii) based on the 5×3 cell domain, 'copy' the top layer and 'paste' to the top of it, and 'copy' the bottom layer and 'paste' to the bottom of it. Through the two-step 'copy' and 'paste'

manipulation, a 5×5 cell domain is obtained, as shown in Fig. 3.5 (c), with the original domain marked out by a dashed box.

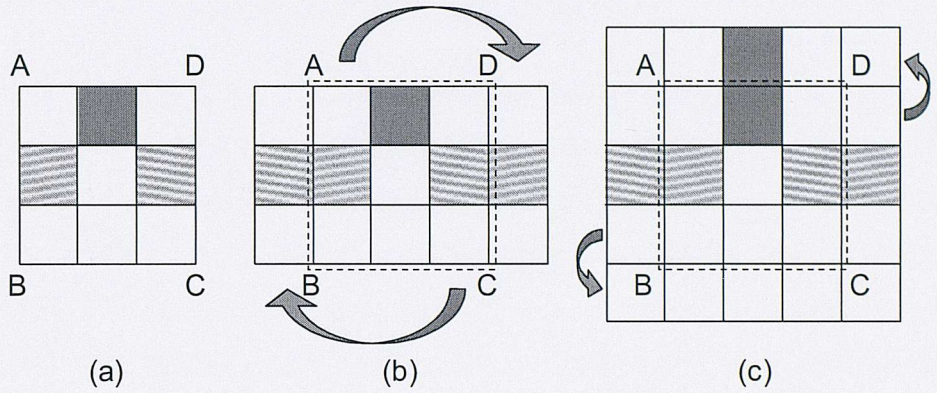

Fig. 3.5 Schematic illustration of two-step 'copy' and 'paste' manipulation to apply boundary conditions to the domain: (a) the original domain with boundary ABCD; (b) 'copy' the left row of cells and 'paste' them to the right of the original domain, and 'copy' the right row and 'paste' to the left of the original domain; (ii) 'copy' the top layer and 'paste' to the top of it, and 'copy' the bottom layer and 'paste' to the bottom of it.

We now consider the effect of this manipulation on the neighbourhood configuration of the original cells in the enlarged domain. Every cell within the dashed box has exactly four neighbouring cells; the boundary conditions at the sides A-B and C-D are identical, resulting in a periodic pattern; at the sides A-D or B-C, the layers of cells above or below the side have the same the concentration and state indices, which means that neither can the solute diffusion nor the grain growth can cross the side. Thus a zero-flux boundary condition is in effect. This manipulation can be extended to a domain composed of $m \times n$ cells, and a temporary buffer array of $(m+2)\times(n+2)$ cells will be obtained.

For the 3D model a regular cubic grid is used, the 'copy' and 'paste' method can also be used to apply boundary conditions, but it becomes a three-step manipulation. This manipulation is used to facilitate the programming and computation. Within the

enlarged domain, all the original cells have an identical neighbourhood configuration that can be treated in the same way when calculating diffusion and growth. This can save much more computational time than that required for the two- or three-step 'copy' and 'paste' manipulation. Both the periodic and zero-flux boundary conditions will be used in the simulations presented in the following chapters.

Although a regular rectangular grid is used in the model, the model is not constrained by this simple geometry. Complex dendrite morphology can be reproduced, providing that the scale of the grid is much smaller than the microstructural features. The model can also deal with the problems of solidification in a complex shape mould, such as that in Fig. 3.6 (a), by introducing a special kind of invariant cells: 'mould cell'. The complex shape mould is discretised using a regular square grid, with an amplified section shown in Fig. 3.6 (b). Those cells filled with grey colour, represent the mould, which means neither solute diffusion nor grain growth can happen in them; therefore they are assigned a special state indices, usually set as '-1', to be distinguished from liquid cells (with a state index '0'), and 'growing' or solid cells 'with an index greater than 0).

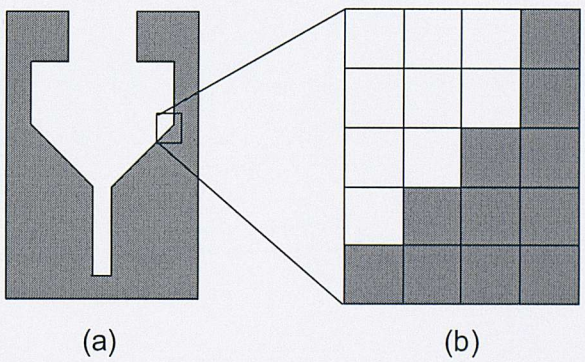

Fig. 3.6 (a) Schematic illustration of a complex mould; (b) sectional enlargement of meshing the mould using a regular square grid.

During the computational loop at each time step in calculation, the state index of each cell is first checked, and diffusion and growth will only be considered for those cells with an index equal or greater than zero. Thus these 'mould cells' are skipped over.

When a liquid, 'growing' or solid cell is in contact with a 'mould cell', a zero solute flux condition is applied between them. 'Mould cells' will be utilised in the simulation of dendritic growth in the platform region of single crystal superalloy turbine blades, which will be presented in Chapter 7.

3.5 Solution Techniques

The framework of the model has been presented above. Now parameters for the simulated alloy system and numerical computation need to be selected. The parameters which include the materials properties will be given in the following chapters. The two of the most important computational parameters for simulations are cell size, Δx, and time step, Δt, both of which will profoundly affect the computational time.

For the 2D simulations, if the cell size (Δx) is reduced, while maintaining the size of the model domain, the total number of cells will be increased, in inverse proportion to $(\Delta x)^2$. For the 3D cases, the total number of cells is inversely proportional to $(\Delta x)^3$. Therefore the computer memory required for the simulations will be increased by a factor of 4 if the cell size is halved, and the computation time will increase by an even greater factor.

According to the Courant stability requirement (Anderson, *et al.* 1984), the time step should be chosen such that

$$\Delta t \leq A \frac{(\Delta x)^2}{\max(D_L, D_S)}, \tag{3.19}$$

where the coefficient A is 1/2 for a 1D case, 1/4 for a 2D case, 1/6 for a 3D case. If maintaining the same solidification time in the simulations, the total time step is inversely proportional to $(\Delta x)^2$. During the computational loop at each time step, each cell will be checked, thus the computation time required for each step is roughly proportional to the total number of cells, which is inversely proportional to $(\Delta x)^2$ for the 2D case, and $(\Delta x)^3$ for the 3D case. Therefore, the total computational time for simulations in a given size domain for a given solidification time, is inversely

proportional to $(\Delta x)^4$ for the 2D case, and $(\Delta x)^5$ for the 3D case. For example, if Δx is halved, the computational time will increase by a factor of 16 (2D) or 32 (3D); if Δx is reduced to 1/5 its original value, the computational time will increase by a factor of 625 for the 2D case. This means that if a 2D simulation using a 5 μm cell takes one day to finish, it will take about two years if using a cell size of 1 μm. It is tempting to use a large cell size in simulations in order to save computational time, but critical information about the dendritic microstructure will be lost if the cell size is too big. The effect of cell size and time step will be discussed in detail with some examples in Chapter 4.

A moving frame of reference technique has been applied in the simulations of directional solidification. When the temperature at the bottom decreased to a predetermined value, the bottom layer of cells is removed from the simulation domain. All the other layers are then shifted down by one cell and a new layer with the initial concentration added to the top of the simulation domain. This technique allows the dendrites to grow to a sufficient length to ensure a stable state is reached, without increasing the domain size and hence reducing the computational resources required.

The model has been applied to simulate columnar growth in directional solidification in both 2D and 3D, solidification at geometrical discontinuities, and competitive growth. The results are presented and discussed in the following chapters.

Chapter 4
Two Dimensional Simulation of Directional Solidification

Many multi-component industrial alloys are solidified in conditions that produce a complex array of columnar dendrites where microsegregation of alloying elements occurs. For face centred cubic (fcc) alloys this segregation pattern is characterized by primary dendrites parallel, and secondary dendrites perpendicular to, the <100> directions closest to the macroscopic solidification direction; these features can have significant effects on the mechanical properties of solidified products (Flemings 1974; Kurz, *et al.* 1992). In case of the nickel-based superalloys used for gas turbine blades and discs, these features are of particular importance as their influence can persist through the subsequent themo-mechanical and/or heat treatment process (McLean 1983). In order to improve the properties of the cast alloys, as well as controlling the formation of solidification defects, a fundamental knowledge of the growth of the initial dendritic microstructure during solidification is required. Numerical investigation of the influence of the processing parameters upon the dendritic structure formed during directional solidification was carried out using the model described in Chapter 3. Process operational parameters such as pulling velocity and thermal gradient were studied. Perturbation of these parameters was also taken into consideration, to simulate the variations that occur in practical casting processes. The simulations were performed in both two and three dimensions, with results presented in this chapter and the following one, respectively.

4.1 Simulation Parameters

Nickel-based superalloys have a fcc austenitic solid-solution matrix phase, which has the capability of maintaining good tensile, rupture and creep properties to a very high temperature (e.g. 0. $7T_m$ according to (Bradley 1988; Tien, *et al.* 1989)). Alloy 718 is one of the most frequently used superalloys for gas turbine discs. The chemical composition of alloy 718 is listed in Table 4.1.

Table 4.1 Chemical composition of alloy 718 (ESPI 2003)

Element	Concentration (wt%)	Element	Concentration(wt%)
Ni	50-55	Cr	17-21
Fe	Balance	Co	1
Mo	2.8-3.3	Nb	4.75-5.5
Ti	0.65-1.15	Al	0.2-0.8
C	0.08	Mn	0.35
Si	0.35	B	0.006
Cu	0.3		

In this study alloy 718 is approximated as a Ni-Nb binary alloy demonstrating the effect of dendritic growth without high computational cost of considering the multi-component system. Nb is selected due to its combination of a partition coefficient far from one, relatively large concentration and high liquidus slope. This combination will make the largest impact on diffusion-controlled growth of dendrites in solidification. The properties of the approximated Ni-Nb binary alloy are listed in Table 4.2.

Table 4.2 Material properties of the Ni-Nb binary alloy (Nastac 2000; Xu, *et al.* 2002)

Property	Variable	Value
Liquidus temperature	T_{liq}	1609 K
Initial concentration	C_0	4.85 wt%
Liquidus slope	m_l	-10.9 K/wt%
Equilibrium partition coefficient	k	0.48
Diffusion coefficient in liquid	D_L	3.0×10^{-9} m^2/s
Diffusion coefficient in solid	D_S	3.0×10^{-12} m^2/s
Gibbs Thomson coefficient	Γ	1.0×10^{-7} K·m

4.2 Model Verification

Firstly, a qualitative comparison is carried out between the simulations and experimental results. Fig. 4.1 (a) shows the simulated dendritic structure for conditions of a pulling velocity (V) of 150 μm/s and a thermal gradient (G) of 12 K/mm. At the beginning of the simulations, 12 seeds are evenly placed at the base, and with the preferred growth directions, <100>, perfectly aligned with the grid. The resultant primary dendrites are parallel to the macroscopic solidification direction, and have a uniform spacing of 250 μm. And the secondary dendrites are also reproduced in the simulations. Unlike the primary dendrites, the secondary dendrites are not identically arranged nor are they of uniform size, indicating a degree of randomness in their formation and competition in their growth. This result is compared to the actual microstructure obtained in solidifying IN718 under similar conditions (V = 145 μm/s and G = 14 K/mm) (Wang, *et al.* 2001), and good correlation is found between them. Compared to previous CA models (Gandin, *et al.* 1997; Xu, *et al.* 2000), one of the major improvements of the current model is the capacity to reproduce the dendritic microstructures.

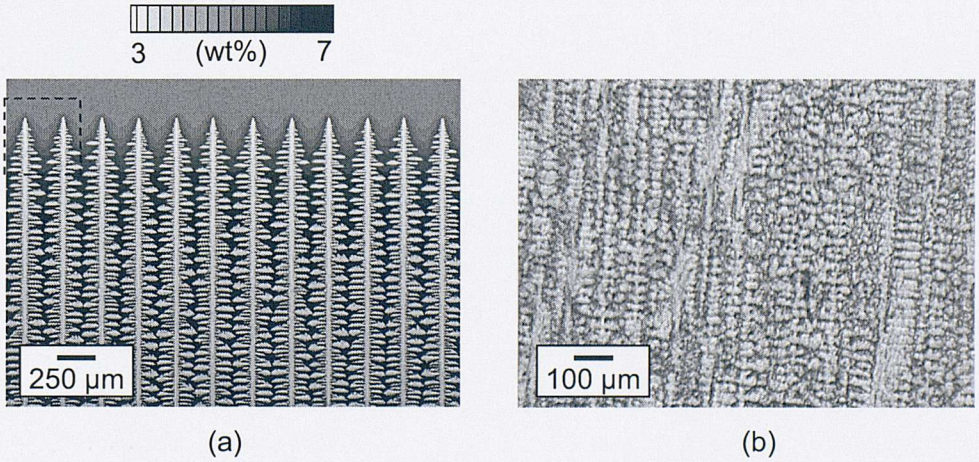

Fig. 4.1 Longitudinal profiles of columnar dendritic grains: (a) predicted by micro-model simulation under a pulling velocity of 150 μm/s and a thermal gradient of 12 K/mm; and (b) obtained experimentally for alloy 718 under a pulling velocity of 145 μm/s and a thermal gradient of about 14 K/mm (Wang, *et al.* 2001). The region in the small dashed box is magnified in Fig. 4.2 (a).

4.2.1 Concentration Profiles

A small region is taken from Fig. 4.1, marked by a small dashed box, for further investigation of the concentration profiles. As shown in Fig. 4.2 (a), the dendrite tips have an approximately parabolic shape, as predicted by other simulations (Hunt 1991; Beltran-Sanchez, *et al.* 2002) and observed experimentally (Somboonsuk, *et al.* 1985; Huang, *et al.* 1993).

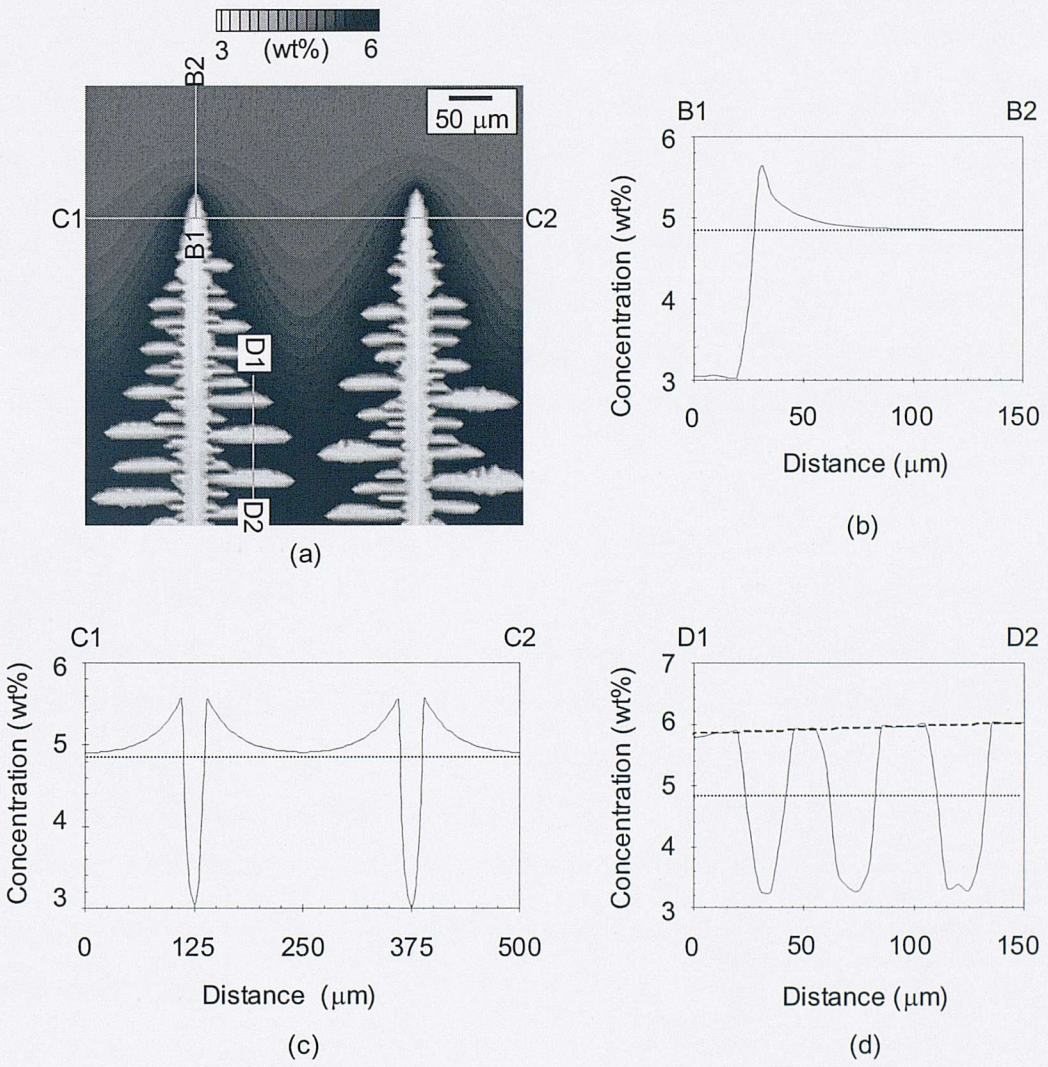

Fig. 4.2 (a) An amplification of the region marked by the small dash box in Fig. 4.1; (b) shows the predicted concentration profile along line 'B1-B2'; (c) along line 'C1-C2'; and (d) along line 'D1-D2'.

The Nb concentration profiles along lines 'B1-B2', 'C1-C2' and 'D1-D2' are shown in Fig. 4.2 (b), (c) and (d), respectively. As shown in Fig. 4.2 (b), the concentration of Nb has a discontinuity at the solid/liquid interface. The concentration is about 3 wt% in the solid, increases sharply to 5.6 wt% at the interface, and then decreases gradually in the liquid to 4.85 wt%, approaching the initial concentration (C_0), which is denoted by the dotted line in the figure. The predicted concentration profile agrees well with the theoretical analysis (Tiller, *et al.* 1953), but the jump at the solid/liquid interface is not absolutely vertical and the maximum concentration in the liquid at the interface is less than that predicted based on the assumption of equilibrium partitioning ($C_L^* = C_S^* / k = 3\text{wt}\% / 0.48 = 6.3\text{wt}\%$). This discrepancy is due to the averaging effect in the 'growing' cell which contains the interface (each small graduation on the 'distance' axis represent the cell size, Δx, in the CA model).

Fig. 4.2 (c) shows the concentration profile along line 'C1-C2' crossing the tips of the two dendrites. The rejected solute forms a pileup layer ahead of the interface, and decreases smoothly as the distance increases. At the interface, the concentration is about 0.7 wt% higher than C_0, and at the mid-point between the two dendrites, it is only about 0.06 wt% higher.

Fig. 4.2 (d) shows the concentration profile along line 'D1-D2' crossing three secondary dendrites. Equilibrium partitioning has almost been reached between the concentration in the solid and liquid, and the ratio approximates the equilibrium partition coefficient (k = 0.48). It is also noted that the concentration in the liquid increases with the distance behind the tip, which agrees well with the theoretical analysis that, the equilibrium concentration in the liquid (C_L) is a function of the distance from the liquidus line (z), $C_L = C_0 - (G/m_l)z$ (Warren, *et al.* 1993) (plotted as the dashed line in Fig. 4.2 (d), and the initial concentration C_0 is plotted as a dot line in this figure).

4.2.2 Effect of Cell Size

The typical scale of primary dendrite spacing is 100 – 1000 μm and the scale of secondary dendrite spacing is 50 – 100 μm in nickel-based superalloys (Pollock, *et al.* 1992; Zou, *et al.* 1992). The domain size must be chosen at a scale of millimetre if

simulations are to be performed for the growth of several dendrites at the same time. The cell size needs to be much smaller than 50 μm in order to reproduce the morphology of secondary dendrites. As mentioned in Chapter 3, for CA models the computational time increases dramatically when the cell size (Δx) decreases for a given domain size; it is inversely proportional to $(\Delta x)^4$ for 2D simulations. Thus the largest cell size which still captures the critical physics is preferred, to reduce the computational time. However, if the cell size exceeds a critical value, some important aspects of the dendritic microstructure (i.e. secondary dendrites) may not be reproduced. Therefore, the effect of cell size on the simulation results has been studied.

A series of simulations were carried out for the growth of columnar dendrites under the same condition, $G = 12$ K/mm and $V = 150$ μm/s. As shown in Fig. 4.3, simulations (a) – (d) were run in a domain of 1.5×1.5 mm^2, and simulation (e) in a smaller domain of 0.75×0.75 mm^2 (only half of the domain is shown in these figures). Different cell sizes were used in these simulations: (a) $\Delta x = 20$ μm, (b) $\Delta x = 10$ μm, (c) $\Delta x = 5$ μm, (d) $\Delta x = 2.5$ μm, and (e) $\Delta x = 1$ μm. Simulations (a) – (d) started with 6 seeds evenly placed at the bottom of the domain, and simulation (e) started with 3 seeds. In all these cases the initial dendrite spacing was 250 μm, and it remained unchanged in the 40 s of growth.

It can be seen form Fig. 4.3 that the simulations with different cell size can all generate dendritic microstructures. As shown in Fig. 4.3 (a) and (b), when cell size is 20 and 10 μm, the resolution of secondary dendrites is not good enough; when it is 5 μm or even smaller, a typical dendritic microstructure can be well reproduced (see Fig. 4.3 (c), (d) and (e)). However, the morphology of the structures is affected by the cell size. As Δx decreases further, the thickness of both the primary and secondary dendrites is reduced. It could be possibly due to the factor that in CA models the amplitude of numerical noise is inversely proportional to the cell size. Earlier studies (Kobayashi 1993) showed that the simulated dendritic structures could be affected by the numerical noises introduced in the calculations.

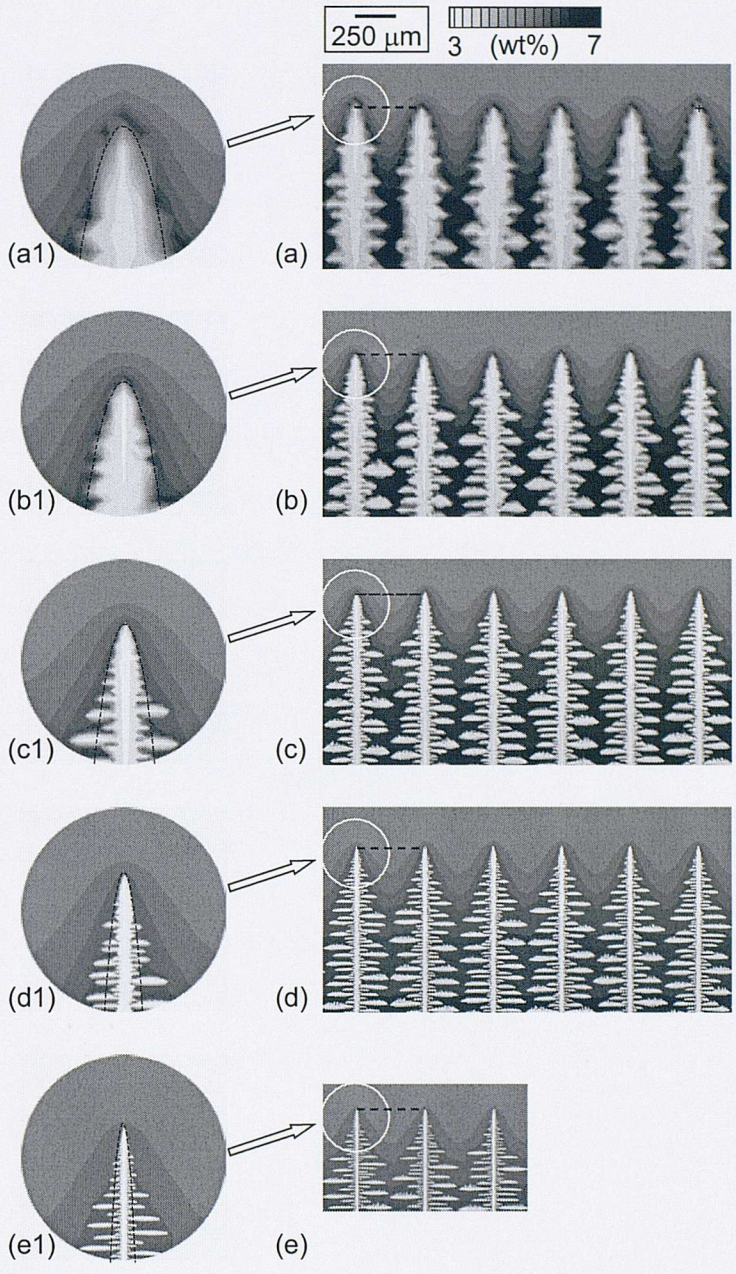

Fig. 4.3 Predicted dendritic morphology using different cell size: (a) 20, (b) 10, (c) 5, (d) 2.5 and (e) 1 μm. (a1), (b1), (c1), (d1) and (e1) are 3× magnifications of the dendrite tips. Simulations (a)-(d) were run in a domain of 1.5×1.5 mm^2 (only half of the domain is shown in the figures), and simulation (e) in a domain of 0.75×0.75 mm^2. All the simulations were run under the same conditions of V = 150 μm/s and G = 12 K/mm. The concentration profiles along the dashed lines are plotted in Fig. 4.5.

Fig. 4.3 (a1) – (e1) are the magnifications of the primary dendrite tips in each cases. All the dendrite tips have approximately a parabolic shape. If a tip approaches a parabolic line expressed as, $y = Ax^2$, the tip radius can be approximately evaluated as, $R = 1/(2A)$. The values of the tip radius are plotted against the cell size in Fig. 4.4 (a). The tip radius increases with the cell size, scaling almost linearly for $\Delta x > 5$ μm. The theoretical analysis proposed by Burden and Hunt (Burden, *et al.* 1974), $R = \sqrt{2\Gamma D_L / m_l V(k-1)C_0}$, would predict a tip radius of 0.38 μm with the same calculation parameters. The numerical model of single dendrite developed by Hunt and Lu (Hunt, *et al.* 1996) would give a tip radius of 0.48 μm. Both of these values are much smaller than the simulated tip radius using the current model (when Δx = 1 μm the simulated R = 0.71 μm). This could be due to the fact the cell size used in the simulations is not small enough. From the trend shown in Fig. 4.4 (a), it is likely that the current model would also predict a tip radius less than 0.5 μm if a cell size smaller than 0.6 μm is used. However, this also requires a dramatically increase in computational time.

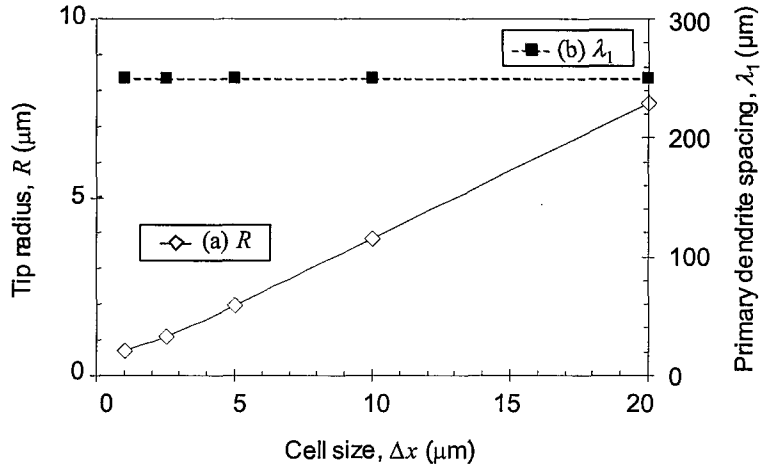

Fig. 4.4 The relationships between the predicted (a) tip radius, R, and (b) primary dendrite spacing, λ_1, with the cell size, Δx, in the simulations shown in Fig. 4.3.

These results show that the model is not entirely network size independent. Beltran-Sanchez and Stefanescu (Beltran-Sanchez, *et al.* 2002) have also found a similar characteristic that tip radius is affected by the grid size in their CA models. However, the main interest of the current study is to explore the influence of processing parameters on the spacing between primary dendrites. Thus it is necessary to examine the influence on the predicted primary dendrite spacing when the cell size changes.

As shown in Fig. 4.4 (b), the dendrites have a primary spacing of 250 μm in all the simulations. However, all these simulations started with the same initial condition that all the seeds were evenly placed at the base, which may have an artificial effect on the final spacing. The profiles of concentration variation, defined as $(C_L - C_0)/(C_L^* - C_0)$, at the primary dendrite tips along the direction parallel with the isotherms (along the dashed lines in Fig. 4.3) are plotted against the distance/λ_1 in Fig. 4.5. Because of the symmetry of these concentration profiles, only half of these curves, from primary dendrite tip to the midpoint between it and its adjacent tip are shown in this figure. It can be seen from this figure that all the profiles follow the same trend, i.e. decreasing approximately exponentially as the distance increases from the tip, and the slope becomes zero as it approaches the midpoint. These profiles show more differences at smaller distance from the tip than at larger distance, which is because the diffusion field near to the primary dendrite tip is more affected by the tip shape than far away from it.

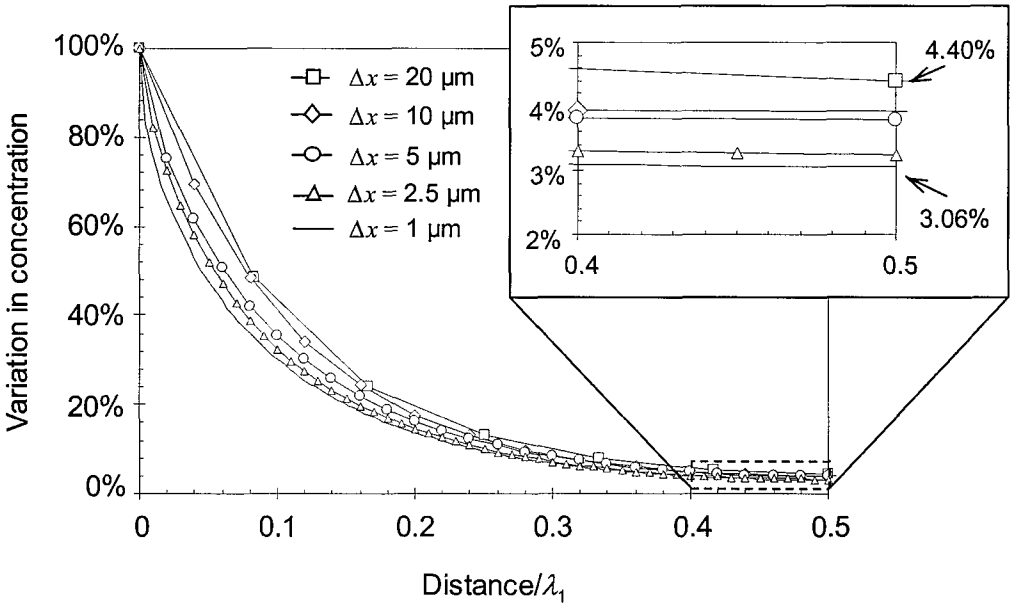

Fig. 4.5 The profiles of the variation in concentration at primary dendrite tips along the direction parallel with the isotherms.

Further examination was carried out for the concentration profiles near the midpoint. The concentration variation decreases from 4.40% to 3.06%, as the cell size decreases from 20 to 1 μm. This variation in concentration can be regarded as the interaction of diffusion fields between two neighbouring dendrites. Hunt and Lu (Hunt, *et al.* 1996) proposed an axisymmetric model to determine the stable limit of primary spacing. Later Wan *et al.* (Wan, *et al.* 1997) further developed this model. Two primary dendrite tips cannot interact with one another when the two tips are so far apart, or the primary dendrite spacing is so large, that the composition at the midpoint between the tips is still the initial concentration. The spacing where interaction first takes place was arbitrarily taken to be when $(C_L - C_0)/(C_L^* - C_0)$ reached 2%. It corresponds to the 2% interaction limit line in Fig. 4.6. The minimum observed primary dendrite spacing is expected to follow this limit line for high dimensionless velocities ($> 4\times10^{-6}$). The experiments carried out by Wan *et al.* (Wan, *et al.* 1997) showed that for high dimensionless pulling velocities ($> 4\times10^{-6}$), the minimum spacings agree very well with the 2% interaction limit line, and maximum spacings are a few times higher than the minimum. The dimensionless pulling velocity used in the simulations shown in

Fig. 4.3 is 9.47×10^{-5}, and the dimensionless primary spacing is 1.32×10^{-5}. This results is plotted as the triangular point (c) in Fig. 4.6. It is above the limit line, but is in the stable range.

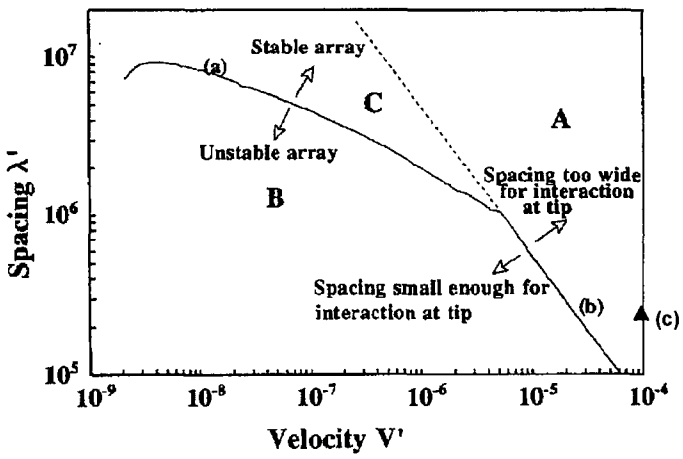

Fig. 4.6 Plot of numerically calculated minimum spacings, the array stability limit line (a) and the 2% interaction limit line (b) (after (Wan, *et al.* 1997)). Point (c) corresponds to the simulations in Fig. 4.3.

It is shown in Fig. 4.6, the point corresponding to the simulations in Fig. 4.3 is above the 2% interaction limit line, which means that at a dimensionless spacing of 9.47×10^{-5} (or dimensional spacing of 250 μm in the current simulations), the interaction of the diffusion field of neighbouring dendrites should be less than 2%. However, as shown in Fig. 4.5, the interaction varies between 3.06% and 4.40 %. This is possibly due to the factor that the model developed by Hunt and his co-workers is an axisymmetric model while the current model is in two dimensions.

Fig. 4.5 shows that when the cell size increases from 1 to 20 μm, $(C_L - C_0)/(C_L^* - C_0)$ at the midpoint increases from 3.06% and 4.40 %. This means the primary dendrite spacing in simulations with larger cell size could be a little higher than in simulations with smaller cell size. However, this effect is not reflected in the simulations shown in Fig. 4.3. This could be due to the influence of the initial conditions - all these

simulations started with 6 seeds evenly placed at the bottom. Therefore, more simulations were carried out with different initial conditions. A range of stable primary spacing was obtained for simulations with different cell size. The results are plotted on a logarithmic scale in Fig. 4.7. The solid line represents the mean value for the spacings, which has a power-law relationship with the cell size, $\overline{\lambda_1} \propto (\Delta x)^{0.15}$. All the points are located within a narrow band demarcated by two dashed lines parallel with the solid line. The upper limit is approximately twice the lower limit.

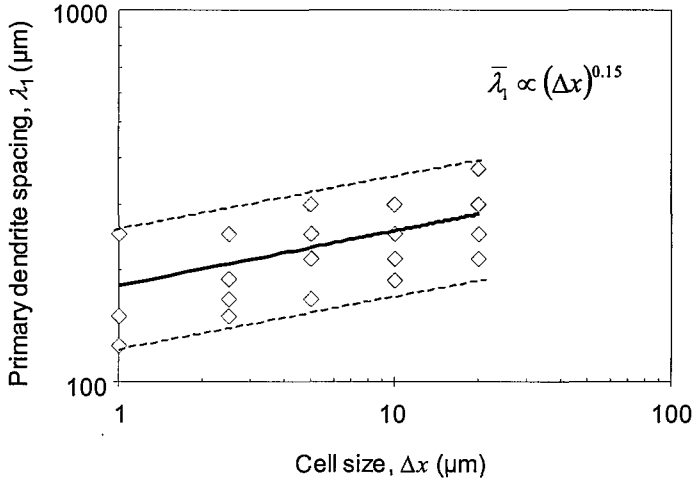

Fig. 4.7 The relationship between the predicted stable band of primary dendrite spacings, λ_1, with the cell size, Δx. The dashed lines are the upper and lower limits of the stable spacings, and the solid line is the average value.

Comparing Fig. 4.7 with Fig. 4.4 shows that the predicted primary dendrite spacing is less dependent on the cell size than the tip radius does. When Δx = 20 μm, the average spacing is about 295 μm; when Δx = 1 μm, it is about 188 μm. Or, in other words, when the cell size is reduced by a factor of 20, the average spacing decreases by a factor of 1.6.

The current model fails to predict the correct tip radius because of its dependence of the cell size. However, it can provide reasonable predictions of the selection of primary spacings. The deviation in the predicted spacing can be evaluated as a function of the

cell size. If the same cell size is used in all of the simulations, the effect of the cell size can be minimized.

Running on an IRIX 195 MHz server, simulations (a) – (c) shown in Fig. 4.3 were all computed within a few hours time, simulation (d) finished within 2 days, but simulation (e) took about 2 weeks (it should be pointed out that simulation (e) was run on a domain only of a quarter area as in other simulations). Taking into consideration both the quality of the results and the computational time, a cell size of 5 μm was adopted in the following simulations.

4.2.3 Effect of Time Step

In order to ensure the numerical stability of the finite difference computation of solute diffusion, the time step, Δt, has to be small enough to satisfy the requirement, $\Delta t \leq 1/4\left(\Delta x^2/D_L\right)$, in 2D simulations. If the cell size is chosen as 5 μm, this requirement becomes $\Delta t \leq 2.1\times10^{-3}$ s. A series of simulation were then carried out for dendrite growth under conditions of G = 12 K/mm and V = 150 μm/s, using different values for the time step, ranging from 1×10^{-4} to 3×10^{-3} s. It was found that the computation of solute diffusion was unstable in the simulation with 3×10^{-3}. All the other simulations were stable, and produced similar results. The relationship between predicted tip undercooling and time step is shown in Fig. 4.8. It can be seen from this figure that the tip undercooling decreases with the time step decreases, and approaches a constant as the time step approaches 1×10^{-4} s. When the time step increases by a factor of 10 from 1×10^{-4} to 1×10^{-3} s, the tip undercooling changes only about 1 per cent. To ensure that the simulations are stable when there is a change in the processing parameters, a time step of $\Delta t = 1\times10^{-3}$ s, was used in the following simulations.

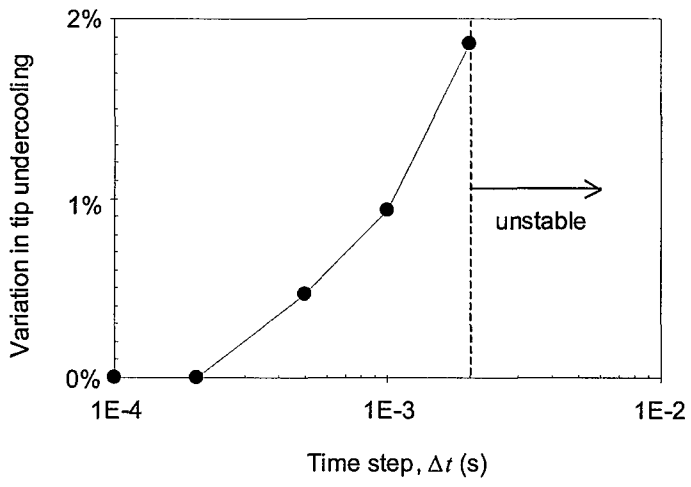

Fig. 4.8 Relationship between predicted tip undercooling and time step.

4.3 Influence of Processing Parameters upon Dendritic Structure

Previous theoretical analysis has predicted that the stable primary dendrite spacing λ_1 in directional solidification is dependent on processing parameters such as pulling velocity, V, and thermal gradient, G, (Flemings 1974; Hunt 1979; Kurz, *et al.* 1981). However, experiments using transparent organic analogues showed that instead of a single value, there exist a range of stable values for λ_1 under given growth conditions (Somboonsuk, *et al.* 1985; Huang, *et al.* 1993; Ma 2002). This gives rise to the following two questions:

- Can columnar dendrites with different spacings grow in a stable state under the same processing conditions; if yes, what is the maximum range of allowable spacings?
- What are the effects of processing parameters upon the selection of stable dendrite spacing(s)?

4.3.1 Selection of Stable Primary Dendrite Spacing

In the following simulations the same imposed solidification conditions were used: G = 12 K/mm, and V = 150 μm/s (giving a cooling rate of -1.8 K/s). It was assumed that no nucleation occurs in the bulk liquid; only the growth of the seeds placed at the base of the directionally solidified ingot is considered. Therefore the final microstructure develops only by branching and overgrowth mechanisms from these initial seeds. The undercooling for the nucleation of the seeds was taken to be 4K throughout this work. Several simulations were run for directional solidification from different numbers of seeds (from 2 to 60) and the preferred growth direction of all the seeds, <100>, were perfectly aligned with the grid. Different growth phenomena are observed in the simulations with different numbers of seeds, which can be roughly divided into three categories: i) steady growth; ii) dendrite branching; and iii) competitive growth.

Fig. 4.9 shows the dendritic structure after 40 s of growth in these simulations with: (a) 8 seeds (375 μm initial spacing); (b) 12 seeds (250 μm initial spacing); and (c) 20 seeds (150 μm initial spacing). In case (a), where the primary dendrite spacing is 375 μm, some tertiary dendrites are observed emanating from secondary dendrites and growing in the same direction of the primary dendrites. However, they are all blocked by other later developed secondary dendrites, with an example shown in Fig. 4.9 (a1). In case (b), no apparent tertiary dendrites are observed due to the smaller primary dendrite spacing (250 μm). In case (c), where the initial primary spacing is even smaller (150 μm), the secondary dendrites are less developed and have a smaller spacing than in case (b). In these simulations, there is no indication of dendrite branching or overgrowth and, consequently, no noticeable deviation from the initial spacings during 40 s of solidification. The primary spacings remained unchanged when the three simulations were continued to 200 s.

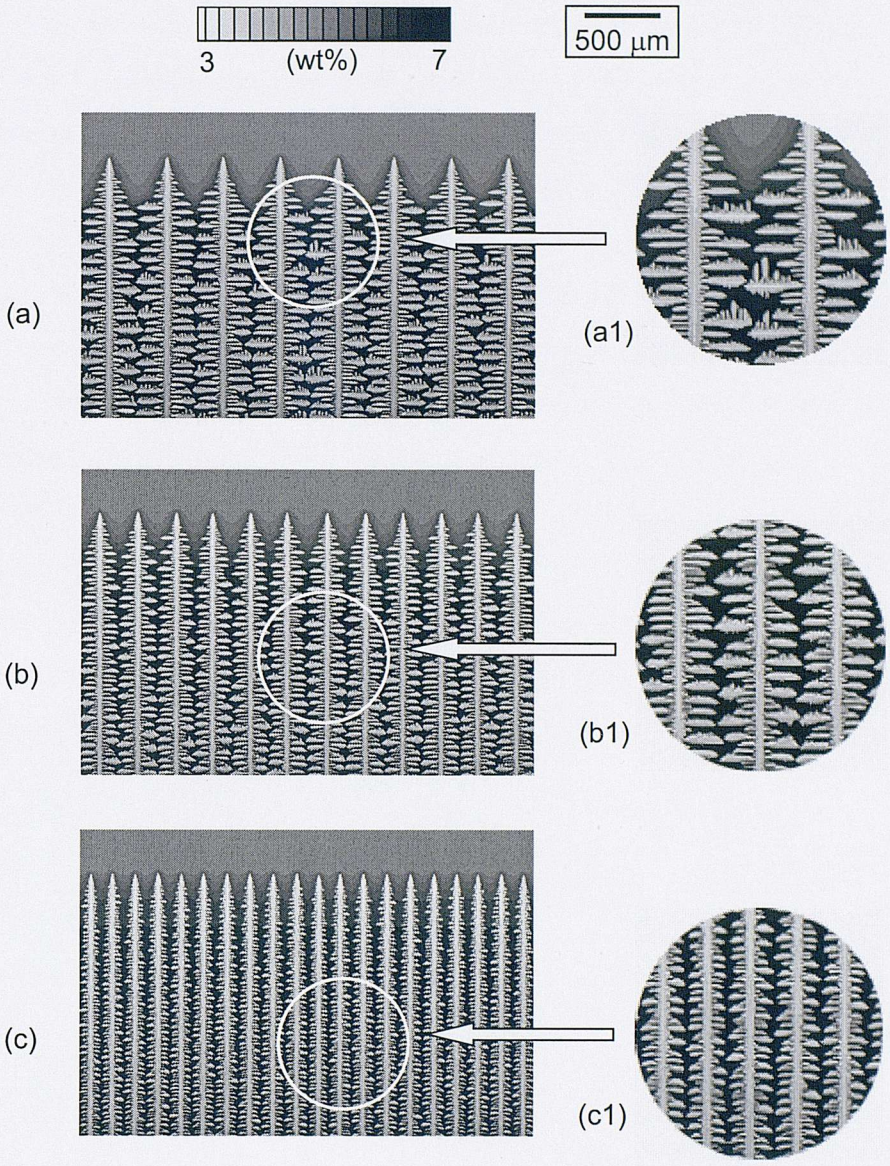

Fig. 4.9 Simulation results of columnar dendrites developing form (a) 6, (b) 12 and (c) 20 seeds after 40 s of growth, under conditions of G = 12 K/mm and V = 150 μm/s. (a1), (b1) and (c1) are 2× magnifications of dendritic structures in each case.

From Fig. 4.9 it can be concluded that the model predicts that columnar dendrites can grow in a stable state 40 s after initiation with a wide range of primary spacings, from 150 to 375 μm for the same thermal conditions. This raises the question of how wide a range is possible, and what will happen if the initial seed spacing is outside this range. Fig. 4.10 (a) and (b) show the dendrite development during the initial growth stage in

two simulations from 2 and 60 seeds respectively. In Fig. 4.10 (a) the dendrites develop from a sparse distribution of seeds with an initial spacing of 1500 μm. As solidification proceeds, many small tertiary dendrites emanate from the secondary dendrites where the undercooling is progressively increased. Some of the tertiary dendrites grow very quickly and catch up with the two original primaries. As a result, λ_1 is significantly reduced, reaching 214 μm after 40 s. Fig. 4.10 (b) shows the dendrite development from a much more closely spaced set of seeds that have an initial spacing of 50 μm. Within 12s, a few dendrites have grown ahead the others blocking their growth by the formation of secondary dendrites. After 40s of growth the dendrite spacing λ_1 increases also to 214 μm. When the two simulations continue to 200 s, λ_1 in case (a) increases slightly to 231 μm while in case (b) it remains unchanged. Although the initial spacings in the two simulations are very different, one is 1500 μm and the other only 50 μm, the final dendritic structures show little difference, and have similar primary dendrite spacings.

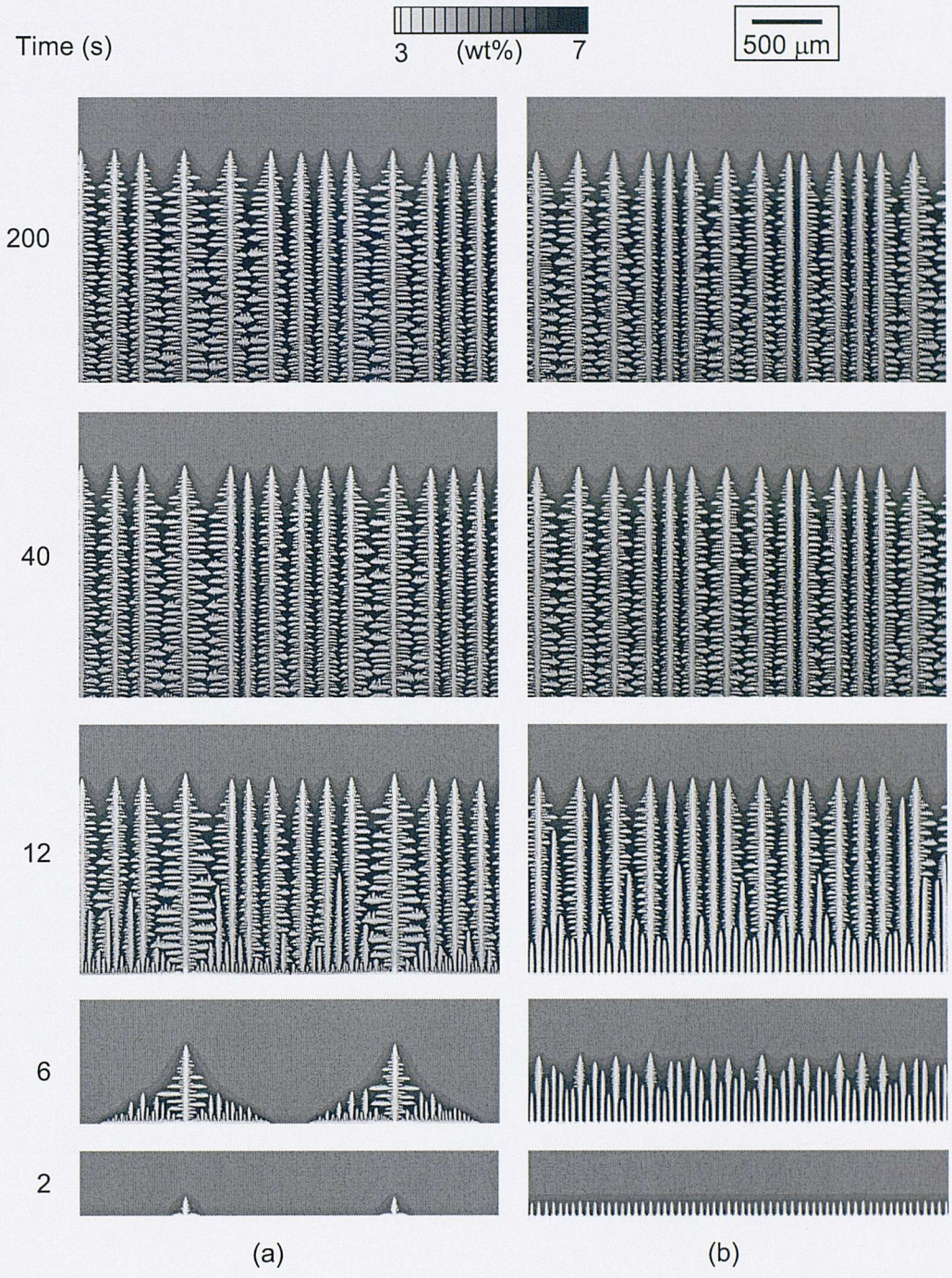

Fig. 4.10 Predicted evolution of dendritic structure in directional solidification processes with (a) 2 and (b) 60 seeds placed at the bottom under conditions of G = 12 K/mm and V = 150 μm/s.

More simulations with different initial seed spacings (λ_1^0) were run to explore the relationship between the final primary dendrite spacing and the initial seed spacing, with the results given in Fig. 4.11. The initial seed spacings ranged from 50 to 1500 μm, resulting in predicted final stable primary dendrite spacings (λ_1^s) of 130 to 380 μm, or an upper limit of approximately 3 times the lower limit. The stable spacing can be divided into three categories:

i. $\lambda_1^s > \lambda_1^o$: when λ_1^o is less than 130 μm, the diffusion field interaction of neighboring dendrites is so strong that competitive growth occurs, with the spacing increasing by an overgrowth mechanism.

ii. $\lambda_1^s = \lambda_1^o$: when λ_S falls between 130 to 380 μm, the simulation results show no change in primary spacing, with a final λ_1 equal to λ_1^o; therefore, the initial spacing is stable for the given thermal conditions.

iii. $\lambda_1^s < \lambda_1^o$: when λ_S is larger than 380 μm, the gaps between the original dendrites are so large that tertiary dendrites can form reducing the spacing by a branching mechanism.

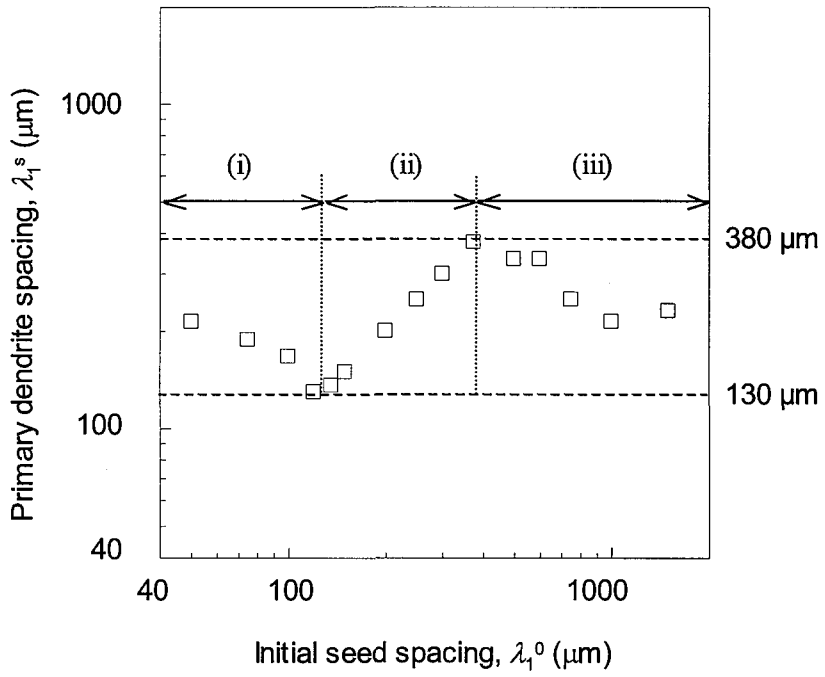

Fig. 4.11 Final stable primary dendrite spacing (λ_1^S) versus the initial seed spacing (λ_1^0).

4.3.2 Effect of Pulling Velocity

It is shown in Fig. 4.9 (c) that under conditions of G = 12 K/mm and V = 150 μm/s, dendrites developing from 20 seeds at the bottom can grow for 40 s without any indication of dendrite branching or overgrowth, maintaining a stable primary dendrite spacing of 150 μm. A question then arises whether such a stable growth state can be maintained if the growth conditions are changed. The effects of pulling velocity and thermal gradient on the growth of columnar dendrites are investigated below.

Fig. 4.12 shows two simulations of dendrites that are growing under different pulling velocities: (a) V = 30 μm/s and (b) V = 75 μm/s, while the thermal gradient and initial seed density are the same as in the simulation in Fig. 4.9 (c). Quite different results are obtained when the pulling velocity is reduced: dendrite overgrowth is observed in both simulations. As shown in Fig. 4.12 (a), when V = 30 μm/s, 11 dendrites stop growing after the solidification front proceeds by a distance of 2.5 mm, and λ_1 increases to 333

μm. As shown in Fig. 4.12 (b), when V = 75 μm/s, the overgrowth process is much slower; after the solidification front moves forward 5 mm, 9 dendrites are blocked out, resulting in λ_1 = 273 μm. Both simulations of growth were then continued for another 6 mm, but no further overgrowth was observed. The simulation results show that a wider λ_1 is likely to be selected at lower V.

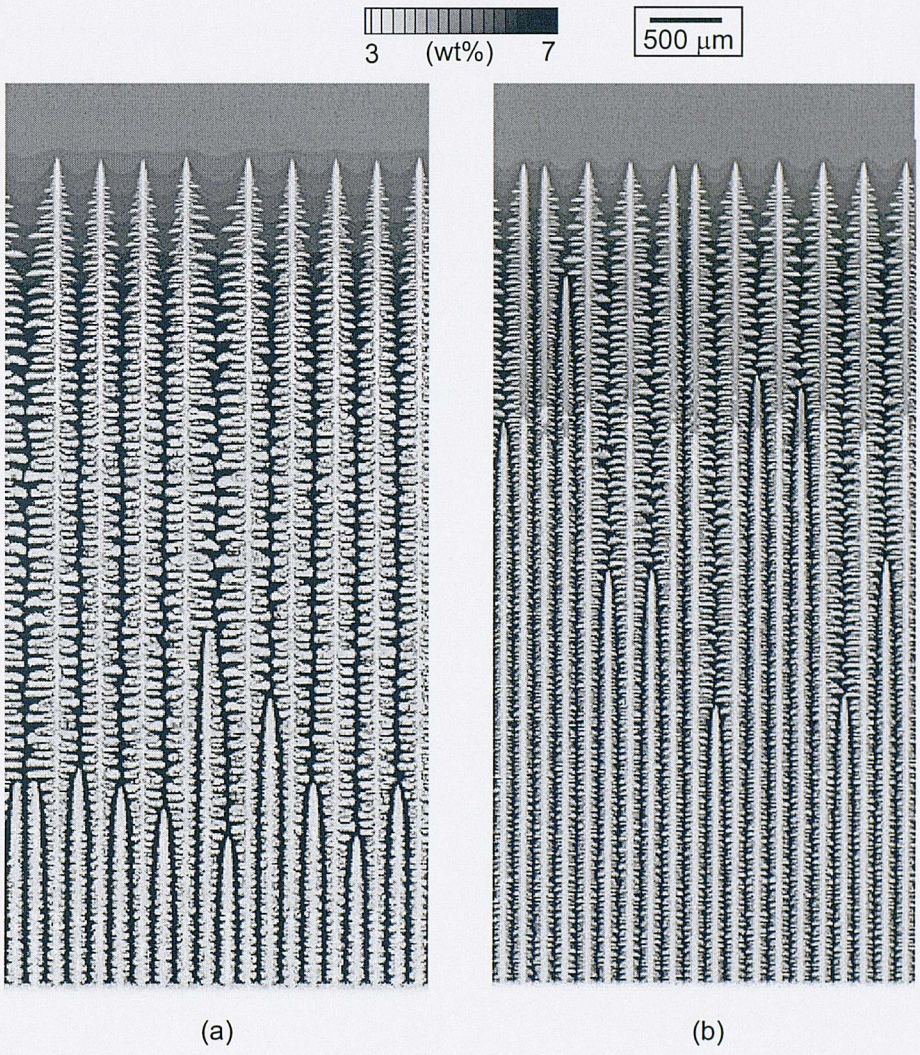

Fig. 4.12 Simulated dendrite structures developing from 20 seeds placed at the bottom at conditions of G = 12 K/mm and different pulling velocities: (a) V = 30 μm/s and (b) V = 75 μm/s.

It has been shown in Fig. 4.11 that simulations starting with different numbers of seeds (2 to 60) predict that columnar dendrites can grow in a stable state with a wide range of λ_1 (from 130 to 380 μm), under a pulling velocity of 150 μm/s. A series of simulations with the same initial nucleation and thermal conditions were then performed for different pulling velocities, from 10 to 300 μm/s. The simulation results show that at each velocity, there is a range of stable values of λ_1 for columnar dendrites. The distribution of the dimensionless average primary dendrite spacing ($\lambda_1' = \lambda_1 m C_0 / \Gamma$) against dimensionless pulling velocity defined as ($V' = V\Gamma / (D_L m C_0)$) is shown in Fig. 4.13. The graph is plotted on a logarithmic scale, with two sets of axes, one for dimensionless values and the other for dimensional values. The points at each pulling velocity represent the final stable primary dendrite spacing in the simulations with different numbers of seeds. It is noted in the figure that fewer points are obtained at some solidification rates that others, because simulations starting with different numbers of seeds can result in the same final primary dendrite spacing.

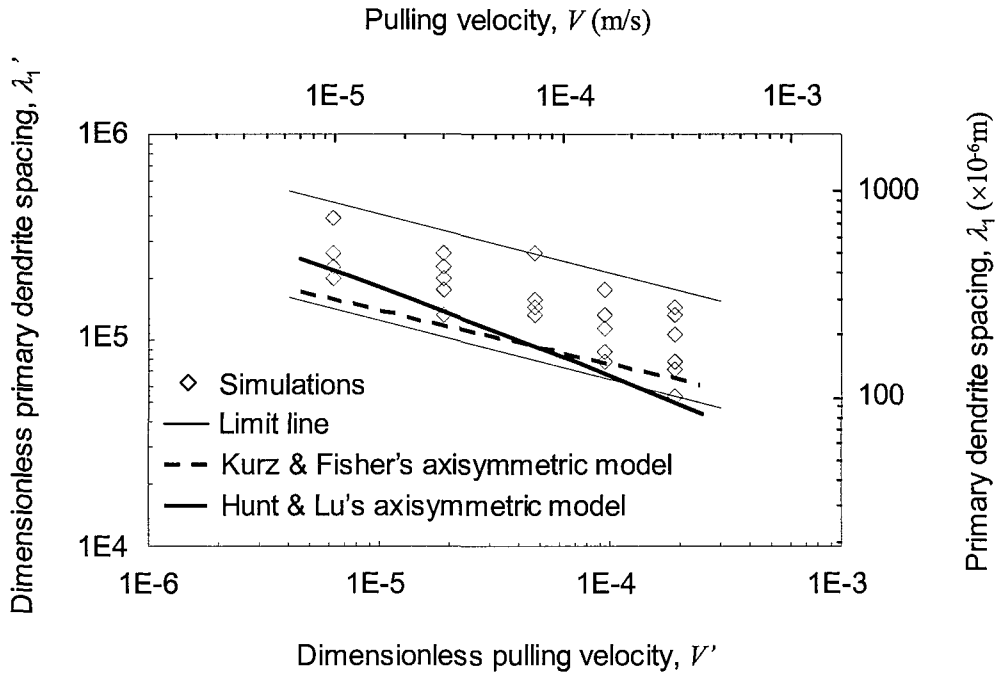

Fig. 4.13 Distribution of primary dendrite spacing against pulling velocity, with comparison to the analytical solution of Kurz and Fisher (Kurz, *et al.* 1992), and also the trend predicted by the numerical model of Hunt and Lu (Hunt, *et al.* 1996).

A notable characteristic of the results is that all of these points are located within a narrow band demarcated by two parallel lines:

$$\begin{aligned} \lambda'_{1\max} &= 1.54\times10^{4}\left(V'\right)^{-0.29} \\ \lambda'_{1\min} &= 4.72\times10^{3}\left(V'\right)^{-0.29} \end{aligned} \quad . \tag{4.1}$$

These two lines give the upper and lower limits of the allowable primary dendrite spacing, both of which are power functions of solidification rate. The value of the exponent is marginally higher than the value of 0.25 predicted by early analytical solutions of dendrite growth (Kurz, *et al.* 1992), but slightly lower than the range of values predicted by Hunt and Lu (Hunt, *et al.* 1996) using a quasi-3D simulation (i.e. axisymmetric). The upper limit of the λ'_1 distribution is about three times that of the lower limit, whereas Hunt and Lu (Hunt, *et al.* 1996) suggested a factor of approximately two. In practical solidification there are inevitable fluctuations in the

processing conditions, which may affect the stable growth of columnar dendrites. The effect of perturbation of the pulling velocity on the selection of the stable primary dendrite spacing will be considered later in this chapter. It is also noted that the average primary dendrite spacing predicted by the simulations is larger than that obtained by the numerical model of Hunt and Lu (Hunt, *et al.* 1996). This is probably because their model is a quasi-3D one, while the current simulations are in 2D. Thus, it is necessary to carry out 3D simulations of directional solidification, which will be presented in the next Chapter.

4.3.3 Effect of Thermal Gradient

The simulations in the previous section have shown that there exists a range of stable spacings for columnar dendrites growing at different velocities, and in this section the effect of thermal gradient will be studied.

In the following simulations the same pulling velocity of 150 μm/s was used, and the thermal gradient varied from 1 to 18 K/mm (giving a cooling rate from -0.15 to -2.7 K/s). Several simulations with different numbers of seeds (from 2 to 30) were carried out for each thermal gradient. Fig. 4.14 shows a series of simulations all starting from 2 seeds but under different thermal gradients: (a) 1, (b) 3, (c) 6 and (d) 18 K/mm. All the simulations were continued for 40 s of solidification. The simulation results show a big variation in primary dendrite spacing: when G increases from 1 to 18 K/mm, λ_1 decreases from 1500 to 176 μm, or decreases by a factor of eight.

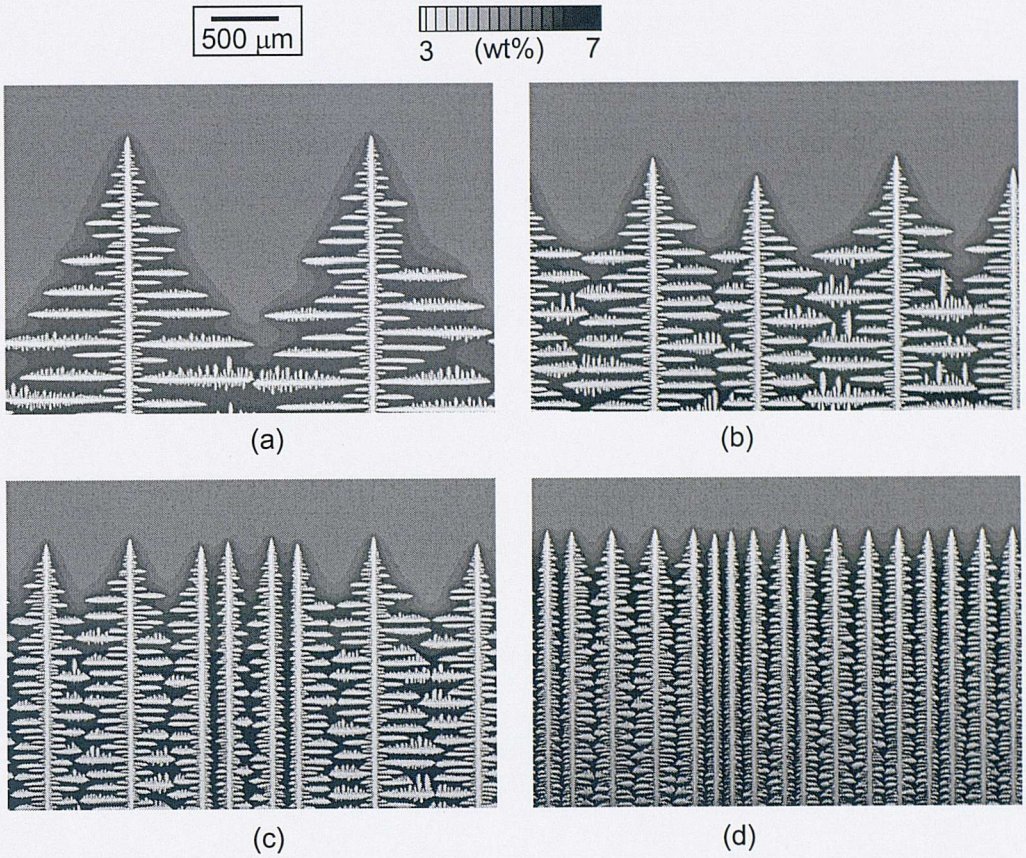

Fig. 4.14 Simulations starting from 2 seeds under conditions of V = 150 mm/s and different thermal gradient: (a) 1, (b) 3, (c) 6 and (d) 18 K/mm.

Similar trends of decreasing λ_1 with increasing G have also been found in other simulations with different numbers of seeds (4, 8, 12, 20 and 30). The distribution of dimensionless average primary dendrite spacing (λ_1') with dimensionless thermal gradient ($G' = G\Gamma/(mC_0)^2$) is shown in Fig. 4.15.

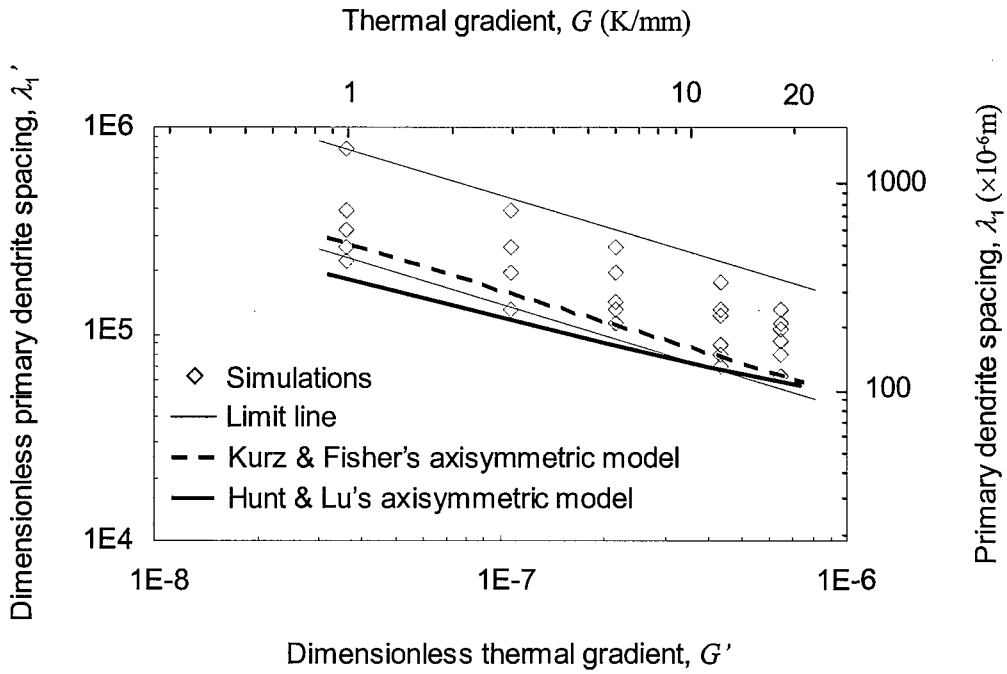

Fig. 4.15 Distribution of primary dendrite spacing against thermal gradient, with comparison to the analytical solution of Kurz and Fisher (Kurz, *et al.* 1992), and also the trend predicted by the numerical model of Hunt and Lu (Hunt, *et al.* 1996).

Similar to the results shown in Fig. 4.13, these points are also all located within a narrow band demarcated by two parallel lines:

$$\begin{aligned} \lambda_{1\max}' &= 1.28\times10^{2}\left(G'\right)^{-0.51} \\ \lambda_{1\min}' &= 3.92\times10^{1}\left(G'\right)^{-0.51} \end{aligned} \quad . \tag{4.2}$$

These two lines giving the upper and lower limits of the allowable primary dendrite spacings, are both power-law functions of thermal gradient. The value of the exponent is almost equal to the value of 0.5 predicted by the analytical solutions (Kurz, *et al.* 1992), and slightly higher than the range of values predicted by the numerical model of Hunt and Lu (Hunt, *et al.* 1996). The upper limit of the λ_1' distribution is again about three times that of the lower limit.

The above simulations have shown that under given growth conditions there exists a range of values for the stable primary dendrite spacing, and both the upper and lower limits of the stable values have a power-law relationship to the pulling velocity and thermal gradient, given by equations (4.1) and (4.2), respectively. If any mutual interaction of pulling velocity and thermal gradient upon the selection of stable primary dendrite spacings is neglected, these two equations can be combined to give

$$\begin{aligned} \lambda'_{1\max} &= 8.75(G')^{-0.51}(V')^{-0.29} \\ \lambda'_{1\min} &= 2.67(G')^{-0.51}(V')^{-0.29} \end{aligned}. \tag{4.3}$$

This result can be compared with Kurz and Fisher's analytical solution, which is also transformed into a dimensionless expression as

$$\lambda'_1 = 5.27(G')^{-0.5}(V')^{-0.25}. \tag{4.4}$$

This constitutes a very good correlation between the analytical and numerical results.

4.4 Perturbations of Processing Parameters

Since perturbations of the control parameters in practical solidification are usually unavoidable, artificial perturbations have been incorporated in the simulations to investigate theirs effect. Perturbations of the pulling velocity and thermal gradient are considered in turn.

4.4.1 Perturbations of Pulling Velocity

In the simulation shown in Fig. 4.16, the pulling velocity underwent the following cycle of perturbation: (i) $t = 0$ s, $V = 150$ μm/s; (ii) $t = 10$ s, $V = 300$ μm/s; (iii) $t = 20$ s, $V = 75$ μm/s; and (iv) $t = 30$ s, $V = 150$ μm/s. The initial primary dendrite spacing is 500 μm (see Fig. 4.16 (a)). Doubling the solidification rate causes almost immediate dendrite branching and a rapid increase in the density of primary dendrites reducing λ_1 from 500 to 188 μm (see Fig. 4.16 (b)). Subsequent reduction in the growth rate to half of the original value, leads to a very slow increase in dendrite spacing, which continues on returning to original growth velocity to approach a stable state spacing of 231 μm

(see Fig. 4.16 (c) and (d)). Fig. 4.16 (e) shows the global structure, from which the generation and annihilation of dendrites can be clearly observed.

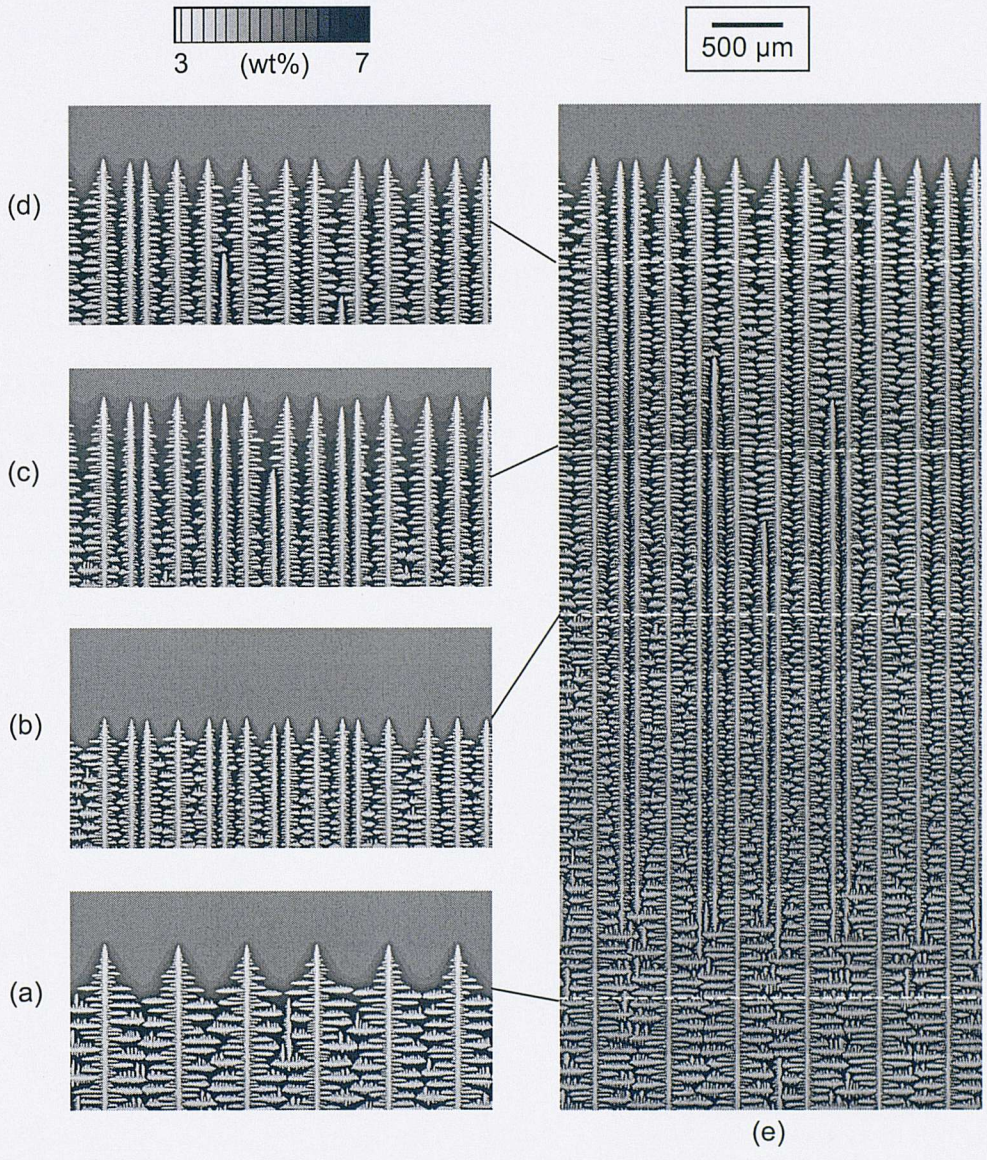

Fig. 4.16 Simulated dendrite structures undergoing a cycle of perturbation of the pulling velocity around a mean value. (a) t = 0s, V = 150 μm/s; (b) t = 10s, V = 300 μm/s; (c) t = 20s, V = 75 μm/s; (d) t = 30s, V = 150 μm/s; (e) the global structure.

Similar perturbations of the pulling velocity were then applied to all the simulations with different numbers of seeds at each pulling velocity. The predicted dimensionless average primary dendrite spacings (λ_1') against dimensionless pulling velocity (V') after perturbations of the pulling velocity are plotted in Fig. 4.17. The upper and lower limits of the λ_1' distribution after perturbation of the solidification rate are expressed as

$$\begin{aligned} \lambda_{1\max}' &= 1.22\times10^{4}(V')^{-0.29} \\ \lambda_{1\min}' &= 5.24\times10^{3}(V')^{-0.29} \end{aligned} \quad (4.5)$$

Comparing the results with those without perturbation (equation (4.1)), the values of the exponents are the same, but the upper limit is now about twice that of the lower limit, which is in better agreement with the values suggested by Hunt and Lu (Hunt, *et al.* 1996). The change in the ratio between the upper limit and the lower limit shows that perturbation of the growth rate reduces the dendrite spacing to a narrower range than the steady state growth condition.

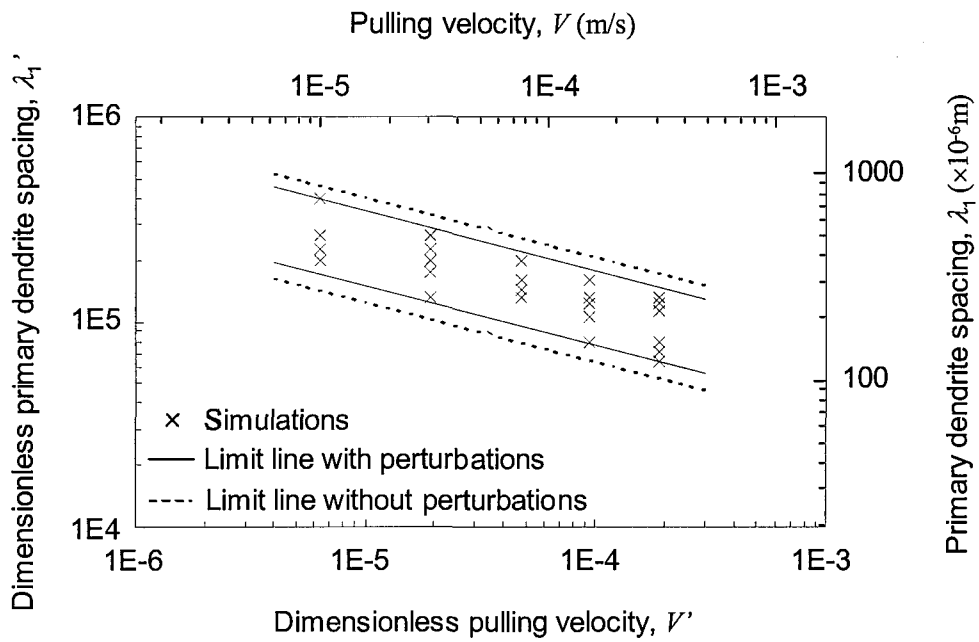

Fig. 4.17 Distribution of primary dendrite spacing against solidification rate after a cycle of perturbation of the withdrawal velocity.

4.4.2 Changing Thermal Gradient

The effect of perturbations in pulling velocity upon the selection of stable primary dendrite spacing has been shown in the previous section, and in this section the effect of changing thermal gradient is studied. In the following simulations, the thermal gradient undergoes a cycle of variation, increasing from 1 to 18 K/mm and then decreasing back to its original value. As shown in Fig. 4.18, the thermal gradient changes in small steps; either increases by 10% in the ascending period or decreases by about 9% in the descending period. At each step the thermal gradient is kept constant for 10 s, except for the last few steps which are 20 s.

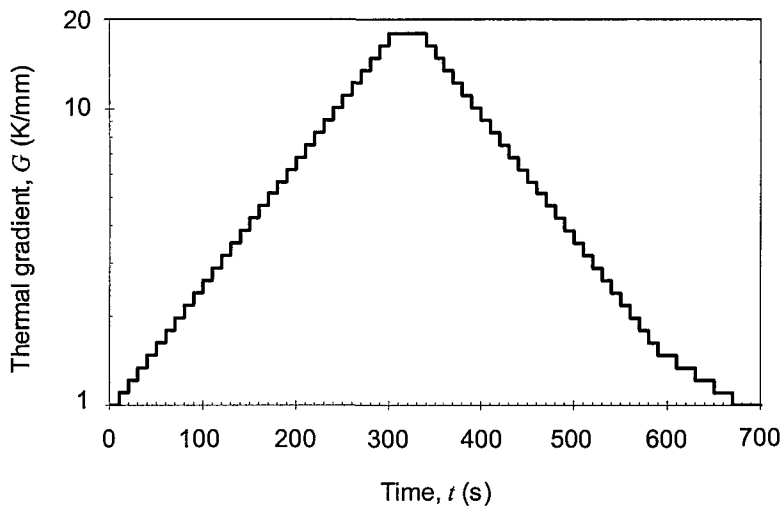

Fig. 4.18 Time dependence of thermal gradient in the simulations.

The values of the average primary dendrite spacing in response to the changing thermal gradient are plotted in Fig. 4.19, together with the limit lines described by equation (4.2). The dendrite structures corresponding to points 'a' to 'h' in Fig. 4.19 are shown in Fig. 4.20 (a) to (h), respectively.

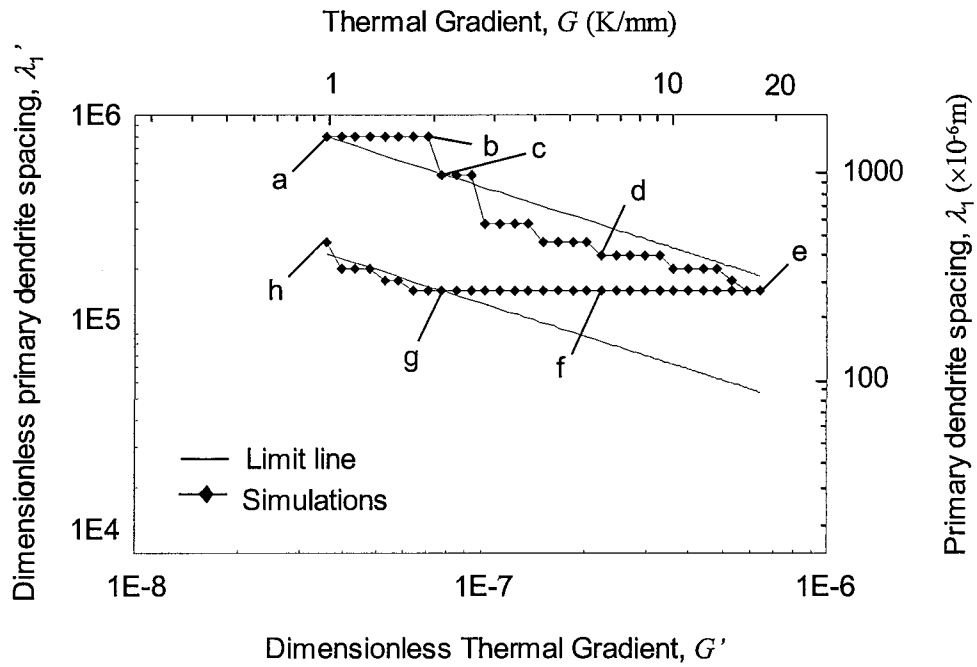

Fig. 4.19 Response of the average primary dendrite spacing to the changing thermal gradient. The dendrite structures corresponding to points (a) to (h) are shown in Fig. 4.20.

The simulations start at point 'a' with a coarse dendrite spacing, λ_1 = 1500 μm, with a thermal gradient of G = 1 K/mm (see Fig. 4.20 (a)). The spacing does not adjust immediately as G increases. In this stall stage, more and more small tertiary dendrites emanate from the secondary dendrites, but are all blocked by other secondary dendrites formed at a position closer to the primary tips (see Fig. 4.20 (b)). When G increases to 2.16 K/mm, one tertiary dendrite successfully penetrates the blockage of secondary dendrites, or dendrite branching happens, and λ_1 is reduced to 1000 μm (see Fig. 4.20 (c)). As G further increases, more and more dendrites are created, and λ_1 decreases correspondingly. When G increases to 6.24 K/mm, λ_1 is reduced to 429 μm (see Fig. 4.20 (d)). At point 'e' the maximum G is achieved and the number of dendrites becomes 10, 5 times as many as in the initial stage, and λ_1 becomes 300 μm, only one fifth of the initial spacing.

Point 'e' is the maximum of the G – variation. During the subsequent decrease in G, from point 'e' to point 'h' in Fig. 4.19, the variation of λ_1 undergoes firstly a hysteresis

period without any change. G decreases to 1.62 K/mm before the first elimination of existing dendrites takes place. During the further decrease in G more and more dendrites are eliminated, leading to a corresponding increase in spacing. At point 'h' G is restored to its original value, but λ_1 doesn't return to its initial value. The final value of λ_1 is 500 μm, only one third of the initial value.

As can be seen in Fig. 4.19, the spacing changes in a discontinuous rather than smooth manner, especially during the early of stage of increasing G. The reason is that in the initial stage of the simulations only two dendrites are present in the domain, which is insufficient for proper statistics. However, the trend in the variation of the dendrite spacing against changing thermal gradient over a wide range is clearly present. It is also noted in Fig. 4.19 that the points are not strictly located between the two limit lines. This deviation happens at low thermal gradients. A possible reason could be that under conditions of low thermal gradient, the dendrite selection process, either branching or overgrowth, is very slow, and a stable state has not yet been reached within 10 s (or 20 s for the decreasing G stage). If a larger domain consisting more dendrites could be used, and the dendrites were allowed to grow for a longer time until a stable state is reached at each step during the G-variation, a better quantitative relationship between λ_1 and G might be able to be obtained. However, this requires much longer computational time (the current simulations took more than one month when running on a IRIX 195 MHZ server).

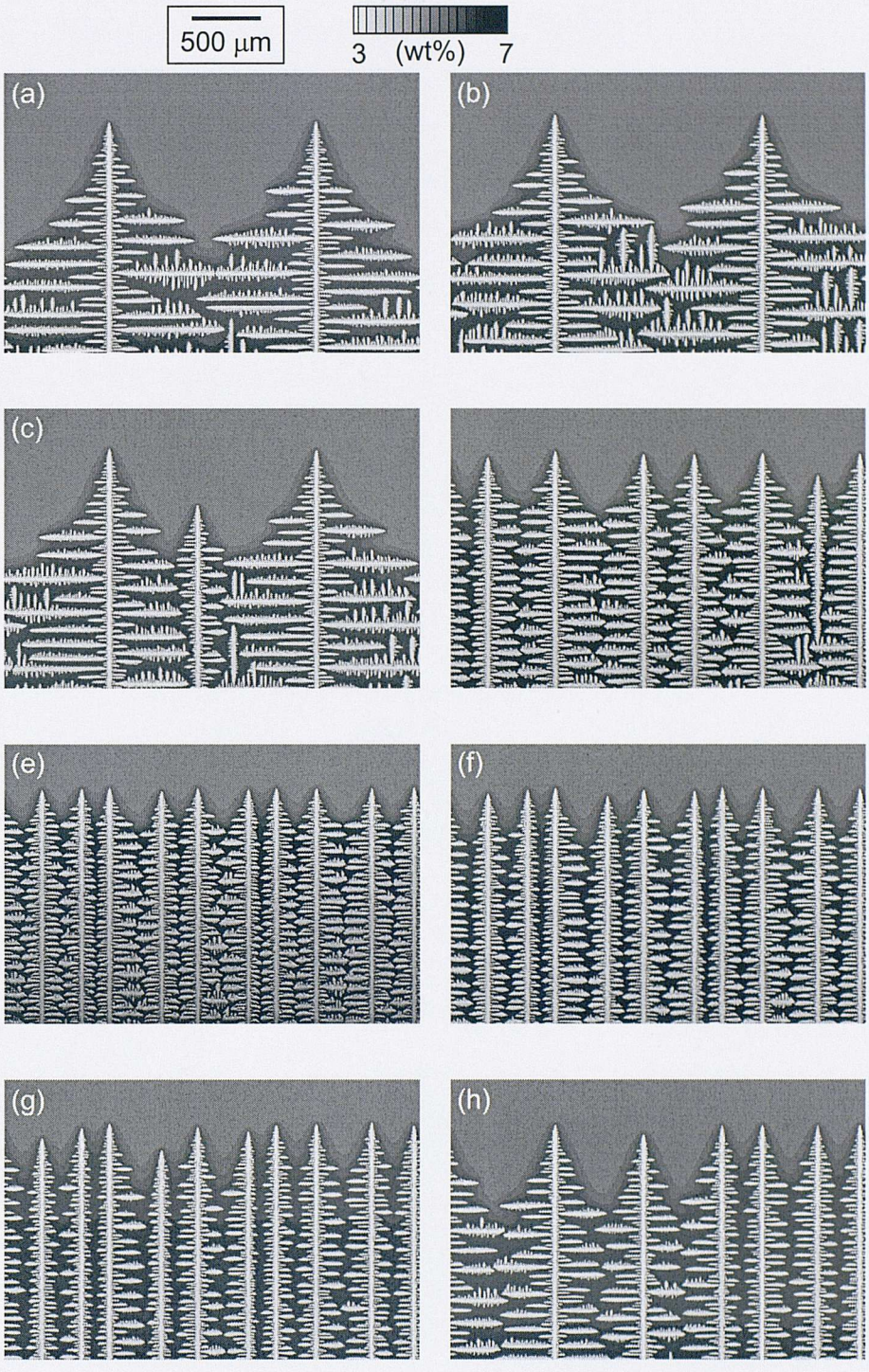

Fig. 4.20 Dendrite structures when thermal gradient undergoes a loop variation: (a) 1.00, (b 1.96, (c) 2.16, (d) 6.24, (e) 18.00, (f) 6.24, (g) 2.16 and (h) 1.00 K/mm.

4.5 Columnar-to-Equiaxed Transition

It was found in the pervious simulations that the stable primary dendrite spacing is affected by the pulling velocity (see Fig. 4.13). The tip undercooling (the concept of total undercooling is used here) of columnar dendrites is also dependent on pulling velocity. The predicted tip undercooling is plotted against velocity in Fig. 4.21. A minimum tip undercooling appears when the pulling velocity is around 30 μm/s; and when the velocity is greater than this value, the points can be fitted by an approximate power relationship:

$$\Delta T'_{tip} = 14.1(V')^{0.48}. \tag{4.6}$$

This equation can also be written as

$$V' = 4.0\times10^{-3}(\Delta T'_{tip})^{2.1}, \tag{4.7}$$

which is in good correlation with KGT model (Kurz, *et al.* 1986).

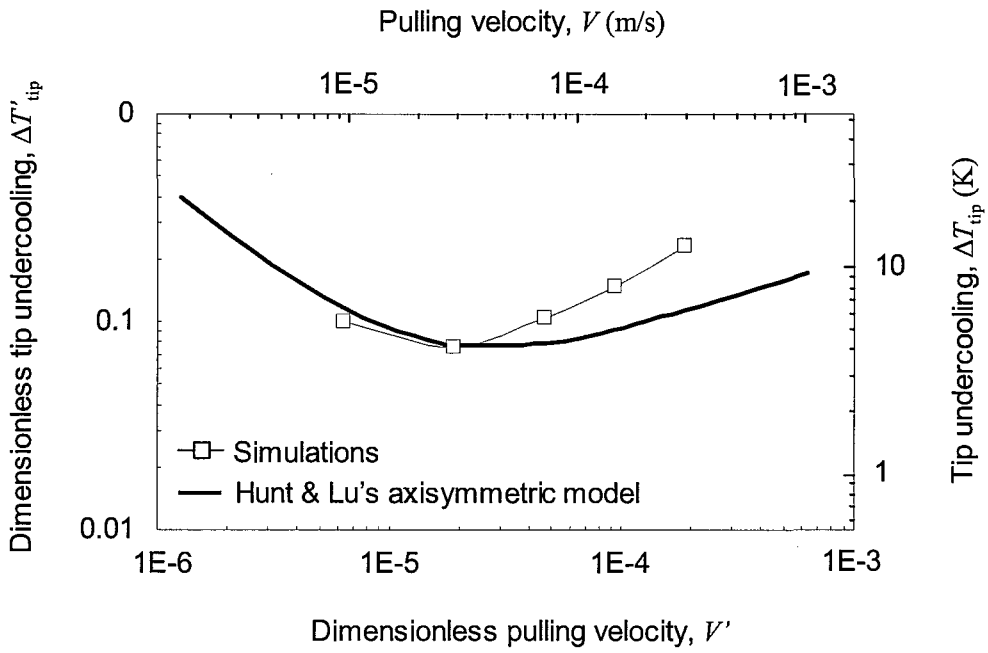

Fig. 4.21 Relationship between pulling velocity and tip undercooling. The thick solid line is the trend predicted by the numerical model of Hunt and Lu (Hunt, *et al.* 1996).

The simulation results are also compared with the prediction of Hunt and Lu's model (Hunt, *et al.* 1996), which is plotted as the thick solid line in Fig. 4.21. The trends are similar, but the power index is higher in the present simulations. It should also be kept in mind that the values of the predicted tip undercooling could be wrong because, as stated in the beginning of this chapter, the model cannot predict the correct tip radius when running on a coarse grid. However, it can at least predict the trend that the tip undercooling increases with increasing pulling velocity.

Nucleation in the bulk liquid was not included in the earlier simulations. It is now considered in the following section, and the effect of changing velocity on the nucleation in front of primary dendrites will be investigated. The parameters for nucleation used in the simulations are list in Table 4.3.

Table 4.3 Nucleation parameters used in the simulations

Parameter	Variable	Value
Nucleation curve centroid	ΔT_N	11 K
Nucleation curve distribution	ΔT_σ	1 K
Maximum grain density	n_{MAX}	4.0×10^{13} /m^3

It can be seen from Fig. 4.21 that when the pulling velocity increases to the range of greater than 30 μm/s, the degree of undercooling at the dendrite tips increases correspondingly, and it will become more favourable for nucleation to occur near the dendrite tip. This effect is accentuated when there is a sudden change in pulling velocity, as the solute distribution at the tips requires time to respond to this change in growth conditions. In the following simulations, the initial pulling velocity of 30 μm/s, is then step-increased by different factors, with the results shown in Fig. 4.22: (a) 2, (b) 3, (c) 4 and (d) 5 times. Quite different results are obtained in these simulations.

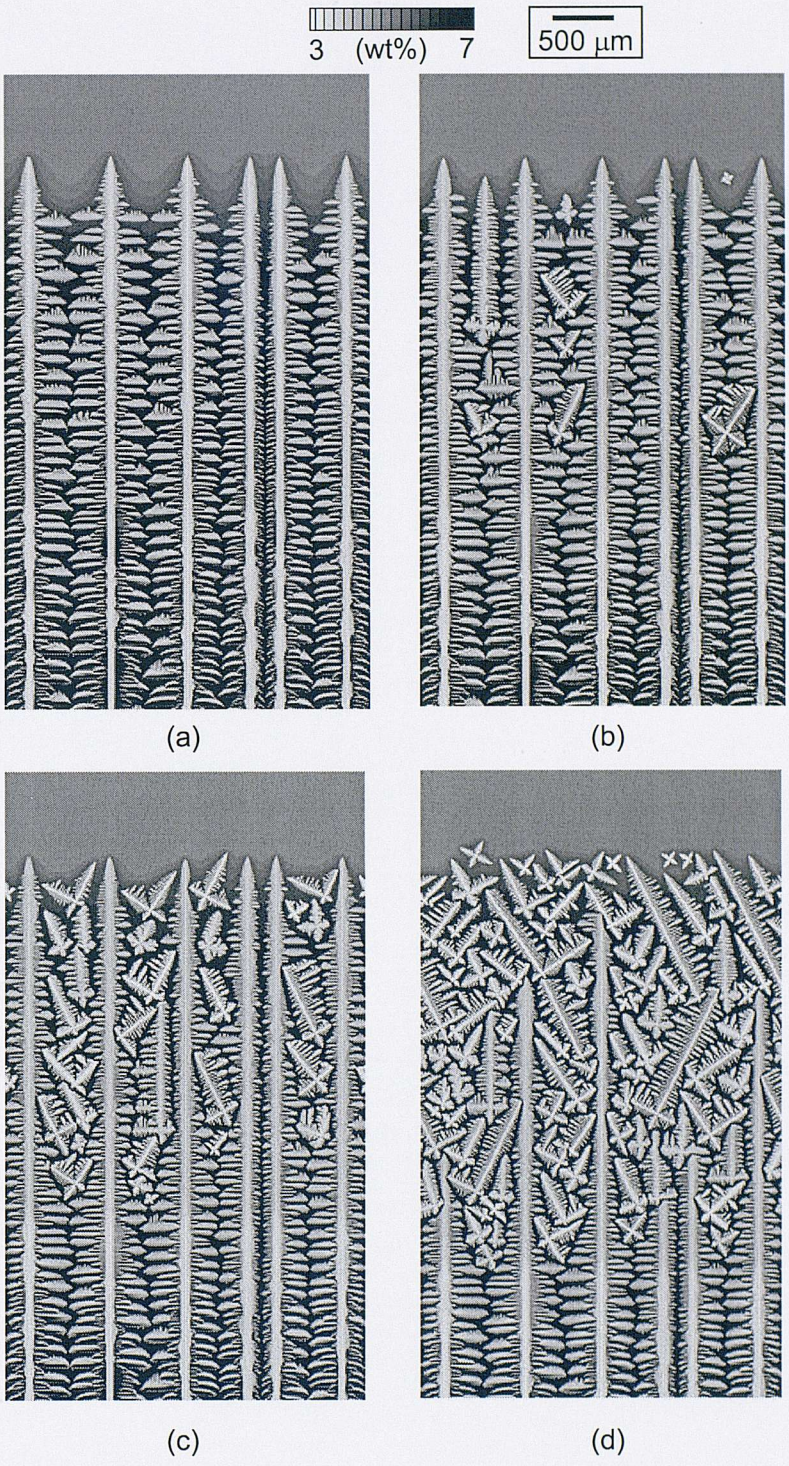

Fig. 4.22 Response of crystal growth and nucleation under conditions that the pulling velocity is step-increased by a factor of (a) 2, (b) 3, (c) 4 and (d) 5.

When the velocity is doubled, no obvious change in the dendrite structures is observed (see Fig. 4.22 (a)). When the velocity is increased by a factor of three to 90 μm/s, some nucleation occurs between the primary dendrites, as shown in Fig. 4.22 (b); when it is increased by a factor of four to 120 μm/s, more nucleation forms between the primary dendrites (see Fig. 4.22 (c)). However, the original primary spacing still persists in growing because of their favourable growth direction. When the velocity is increased by a factor of five to 150 μm/s, many equiaxed grains formed ahead of the columnar dendrites, and finally totally block their growth, or Columnar-to-Equiaxed (CET) transition happens, as shown in Fig. 4.22 (d).

4.6 Summary

The two questions posed early this chapter have now been answered: (i) there is a range of stable spacings for columnar dendrites growing under given conditions, and (ii) the upper limit of the stable spacing is about three times the lower limit under constant conditions, and this ratio can be reduced to about two by perturbations of pulling velocity. Both the upper and lower limits exhibit a power relationship with the pulling velocity and thermal gradient.

The simulations also show that the primary dendrite spacing is not only dependent on the current processing parameters, but also dependent on the processing history. A hysteresis phenomenon has also been observed; that is the primary dendrite spacing doesn't always change immediately when the processing parameters are changed, but there is an incubation period. Variations in the thermal gradient can affect the primary spacing, while perturbations of pulling velocity will affect both primary spacing and tip undercooling. When the pulling velocity increases, the degree of undercooling near the dendrite tips in response can facilitate the nucleation of small equiaxed grains in these regions, or, eventually, cause columnar-to-equiaxed transition.

These conclusions suggest some potential applications of the model. One of these applications is to tailor the primary spacing during directional solidification, by adjusting the pulling velocity and/or thermal gradient.

The simulations were found to correlate well with previous analytical and numerical predictions. However, some discrepancies were also noted. For example, the simulated primary dendrite spacing is larger than that obtained by the numerical model of Hunt and Lu (Hunt, *et al.* 1996). Therefore, it is necessary to carry out some 3D simulations, which will be presented in the next chapter.

Chapter 5
Three Dimensional Simulation of Directional Solidification

The influence of processing parameters on directionally solidified dendritic structures was investigated by carrying out two dimensional simulations, as presented in Chapter 4. It was predicted that there is a range of stable primary dendrite spacings for any given growth condition and that both upper and lower limits of this range have a power law relationship with the pulling velocity and the thermal gradient. The simulations were found have good correlation with previous predictions by other researchers (Hunt, *et al.* 1996; Kurz, *et al.* 1992) but some discrepancies were noted such as the fact that the average value of primary dendrite spacing is higher in the current simulations than in the axisymmetric predictions by Hunt and Lu (Hunt, *et al.* 1996). To gain a better understanding of the solidification process, 3D simulations were carried out and the results are presented in this chapter. The 3D results are compared with the 2D simulations, and also with previous experimental and computational results.

5.1 Model Verification

A 3D simulation was first performed for a single grain growing at a temperature gradient of 12 K/mm and a constant cooling rate of -1.8 K/s. The simulation was run on a regular grid composed of 100×100×100 cubic cells of size 5 μm. The grain is nucleated at the centre of the box at an undercooling of 5 K, with an initial misorientation characterised by three Euler angles (0°, 20°, 0°). The dendritic morphology of the grain after 1 s of growth is shown in Fig. 5.1 (c). The envelope of the dendritic grain is in excellent accord with the analytical and numerical predictions of Gandin and Rappaz (Gandin, *et al.* 1997) for a dendritic grain envelope as shown in Fig. 5.1 (a) and (b). A cell size of 100 μm was used in their simulations in which solute diffusion was not solved.

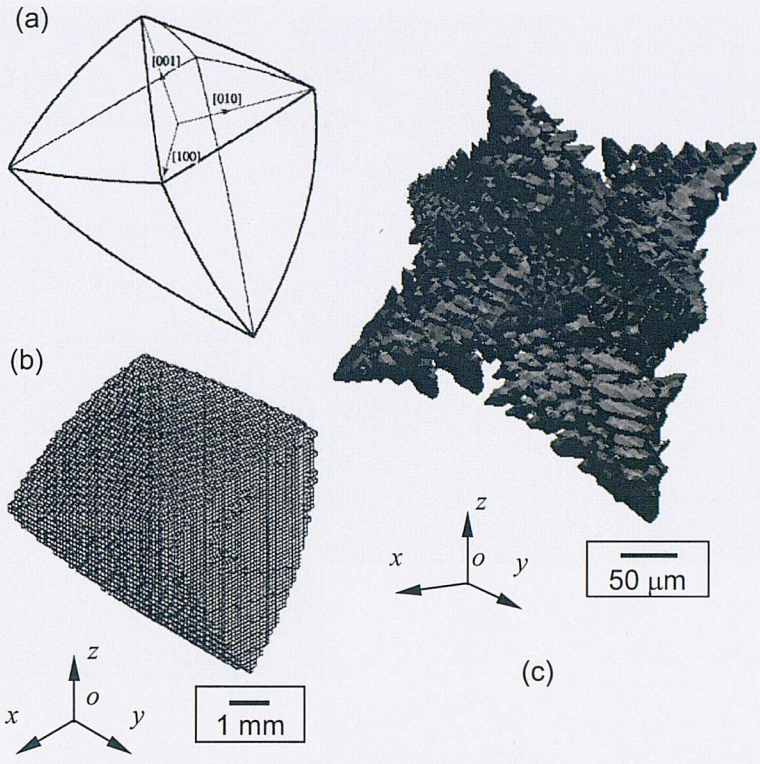

Fig. 5.1 3D views of (a) analytical and (b) numerical predictions for a dendritic grain envelope without taking solute diffusion into consideration (Gandin, *et al.* 1997), and (c) simulated dendritic structure coupled with solute diffusion. Simulation (c) was run on a regular cubic grid with a cell size of 5 μm at a temperature gradient of 12 K/mm and a cooling rate of -1.8 K/s. The original misorientation of the grain is characterized by three Euler angles (0°, 20°, 0°).

The model was then applied to the simulation of directional solidification in three dimensions. The relationship between tip undercooling and pulling velocity is shown in Fig. 5.2. Tip undercooling reaches its minimum at a velocity of about 30 m/s; when the velocity is greater than this the tip undercooling has a power-law relationship with the velocity, which can be expressed as

$$\Delta T'_{\text{tip}} = 7.03(V')^{0.49}, \tag{5.1}$$

or

$$V' = 1.87 \times 10^{-2} (\Delta T'_{tip})^{2.0} . \qquad (5.2)$$

This relationship is very similar to that obtained in 2D simulation (see equations (4.6) and (4.7)), but the tip undercooling values are about 50 % lower than those in 2D simulations. The slope of the ascending section of this curve however is higher than that predicted by Hunt and Lu's model (Hunt, *et al.* 1996) which may be due to the dependence of the tip radius upon the grid size in the current model and this has been addressed in Chapter 4.

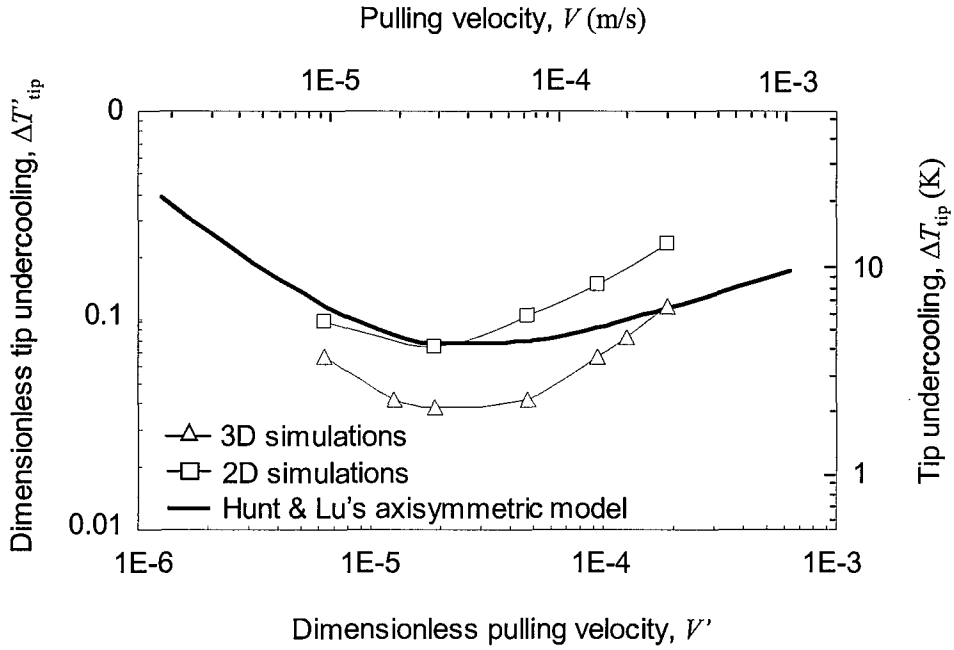

Fig. 5.2 Relationship between tip undercooling and pulling velocity obtained in 3D simulations compared with 2D simulations and Hunt and Lu's predictions (Hunt, *et al.* 1996).

The above simulations show that the predicted tip undercoolings in the 3D simulations are lower than those obtained in the 2D simulations under the same growth conditions. A question then arises as to the relationship between the stable dendrite spacings in 3D and 2D simulations.

5.2 Square Packing of Dendrites

The 2D simulations of directional solidification outlined in Chapter 4 have shown that there is a range of stable primary dendrite spacings for columnar dendrites under given growth conditions. When the initial spacing is outside this range, columnar dendrites can adjust the spacing through branching and/or overgrowth mechanisms. In 2D simulations each columnar dendrite has two nearest-neighbour dendrites, whereas in 3D simulations it can have more than two nearest neighbours. If the columnar dendrites have a regular square packing pattern each dendrite will have four nearest neighbours, and if they have a regular hexagonal packing pattern each will have six nearest neighbours making the interaction between the dendrites much more complex in 3D simulations.

5.2.1 Effect of Initial Seed Density

In the following simulations a regular grid is used consisting of 150×50×250 cubic cells of size 5 μm. For convenience the sizes along the x, y and z directions are called respectively the width, thickness and height of the domain. The imposed solidification conditions in the simulations are: $G = 12$ K/mm, and $V = 150$ μm/s. All the simulations started with an array of existing seeds placed at the base and the macroscopic solidification direction along the z direction. Zero-flux boundary conditions were applied to the top and bottom surfaces, and periodic boundary conditions applied respectively to the left and right sides, and the front and back sides.

Fig. 5.3 shows the development of three dendrites at different time steps: (a) 2, (b) 4, (c) 6 and (d) 40 s. Three seeds are placed at the bottom, centred in the y direction, equally spaced along the x direction, and with the [100] directions perfectly aligned with the z axis. Although some tertiary dendrites are seen to emanate from the secondary arms at the initial growth stage, they are blocked by the secondary dendrites growing from the primary dendrites, as shown in Fig. 5.3 (a1). The three primary dendrites proceed at the same velocity along the z direction, and their spacing remains unchanged (see Fig. 5.3 (b1), and (c1)). At 6 s the moving frame of reference technique is activated, and the whole domain is cooled down at a constant rate of –1.8 K/s. The dendrites keep growing, but their tip position remains roughly unchanged

relative to the moving reference frame. This simulation was continued until 40 s from the start of growth, and no apparent change was observed in the primary dendrite spacing (see Fig. 5.3 (d1). Because of the periodic boundary conditions along the x and y directions, these primary dendrites are arranged quadratically in the transverse section perpendicular to the macroscopic solidification direction. This can be viewed by replicating to infinity the transverse slide shown in Fig. 5.3 (d2) along both the x and y directions. The primary dendrite spacing along the y direction is equal to the domain thickness, 250 μm, and that along the x direction is equal to a third of the width which is also 250 μm.

When only one seed is placed at the bottom, it grows freely along all the directions at the initial solidification stage (see Fig. 5.4 (a1)). The secondary dendrites along the x direction grow faster than in the z direction, because of greater tip undercooling. Many small tertiary dendrites emanate from the fast growing secondary dendrites, growing in the same direction as the original primary dendrite. The newly formed tertiary dendrites have a random initial spacing, and some of them grow very quickly at the expense of others (see Fig. 5.4 (b1)). After 6 s of solidification only 6 primary dendrites survive the competitive growth; among which 5 have developed from the tertiary dendrites and 1 directly from the seed (see Fig. 5.4 (c1)). The 6 dendrites all continue to grow for 40 s, without any obvious change in the structure (see Fig. 5.4 (d1)), resulting in an average spacing along x direction of about 125 μm.

Fig. 5.4 gives an example of solidification with sparse nucleation, during which both branching and competitive growth phenomena are observed. A contrary example with dense nucleation is shown in Fig. 5.5, where 15 seeds are set at the bottom (50 μm initial spacing). Because of the dense packing along the x direction, the growth of secondary dendrites is suppressed, and the secondary dendrites show severely asymmetrical development along both the x and the y directions (see Fig. 5.5 (a2)). As solidification continues, the growth velocities of the 15 dendrites begin to vary, leading some of them to slow down (see Fig. 5.5 (c1)). This competitive growth results in only 10 dendrites surviving after 40 s of solidification (see Fig. 5.5 (d1)), which gives an average primary dendrite spacing along the x direction of about 75 μm, while the spacing along the y direction still 250 μm.

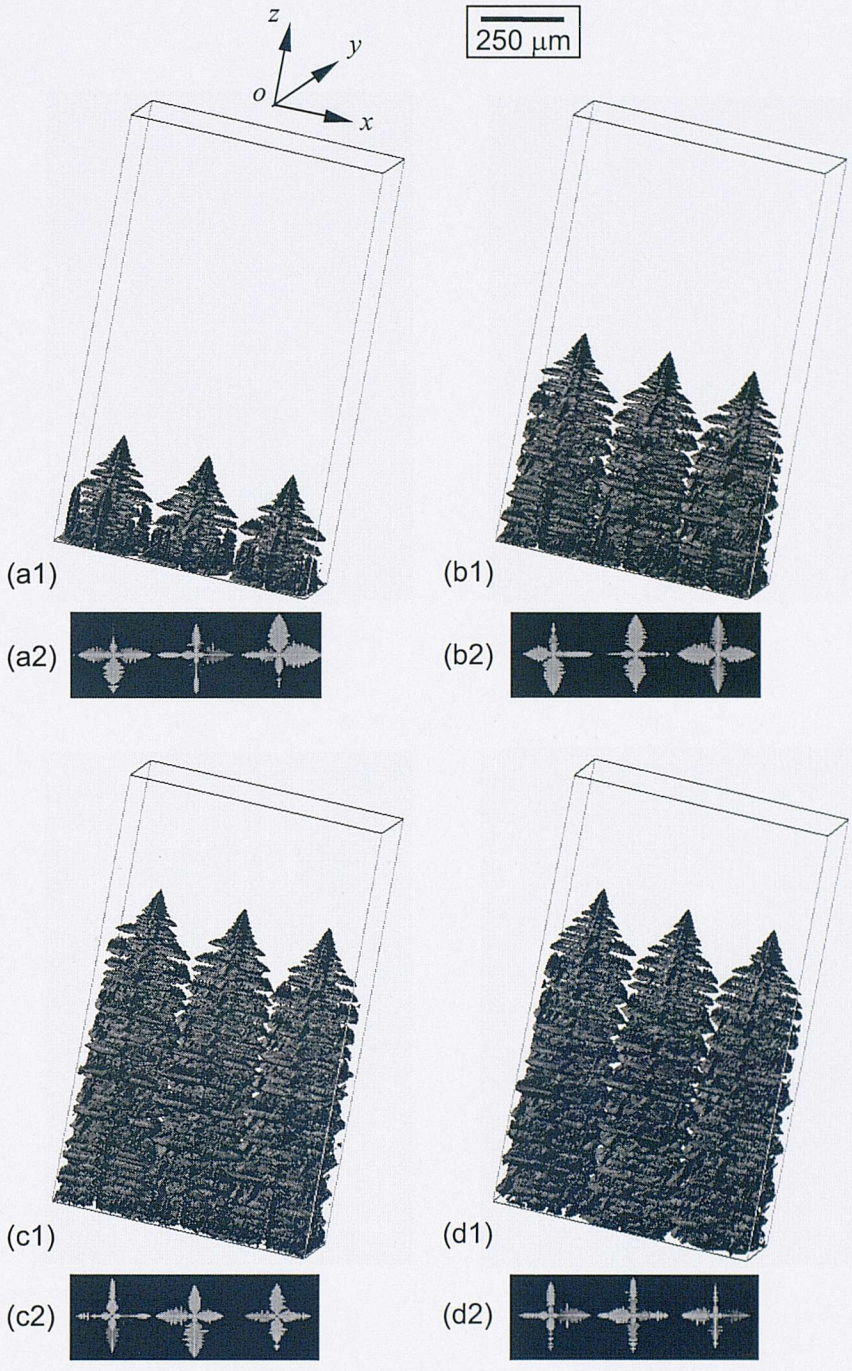

Fig. 5.3 3D simulation for 3 seeds at a solidification time of (a1) 2, (b1) 4, (c1) 6 and (d1) 40 s. (a2) transverse slice at z = 150μm, t = 2 s, (b2) transverse slice at z = 450 μm, t = 4 s, (c2) transverse slice at z = 750 μm, t = 6 s, and (d2) transverse slice at z = 750 μm, t = 40 s.

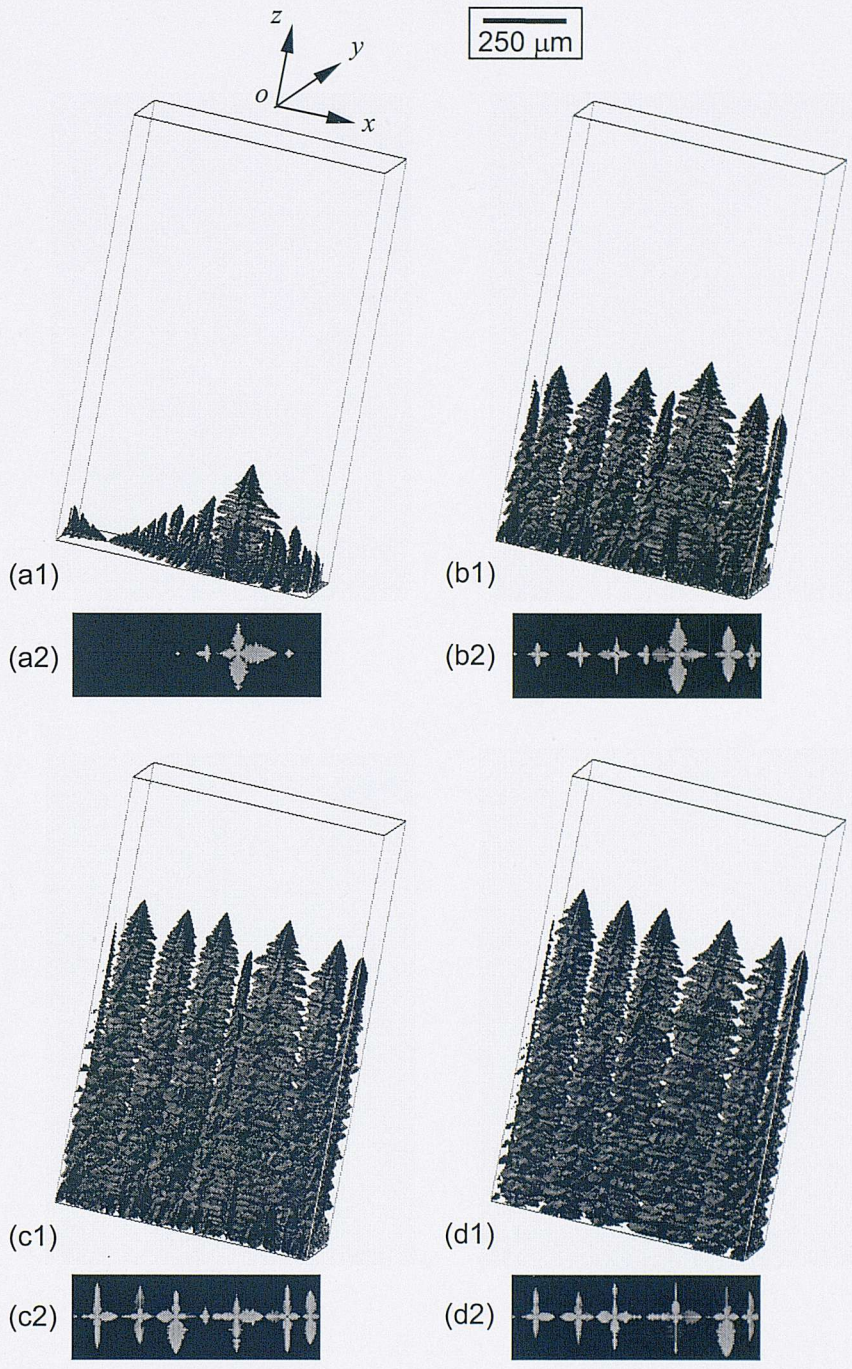

Fig. 5.4 3D simulation for 1 seed at a solidification time of (a1) 2 s (b1) 4, (c1) 6 and (d1) 40 s. (a2) transverse slice at z = 150μm, t = 2 s, (b2) transverse slice at z = 450 μm, t = 4 s, (c2) transverse slice at z = 750 μm, t = 6 s, and (d2) transverse slice at z = 750 μm, t = 40 s.

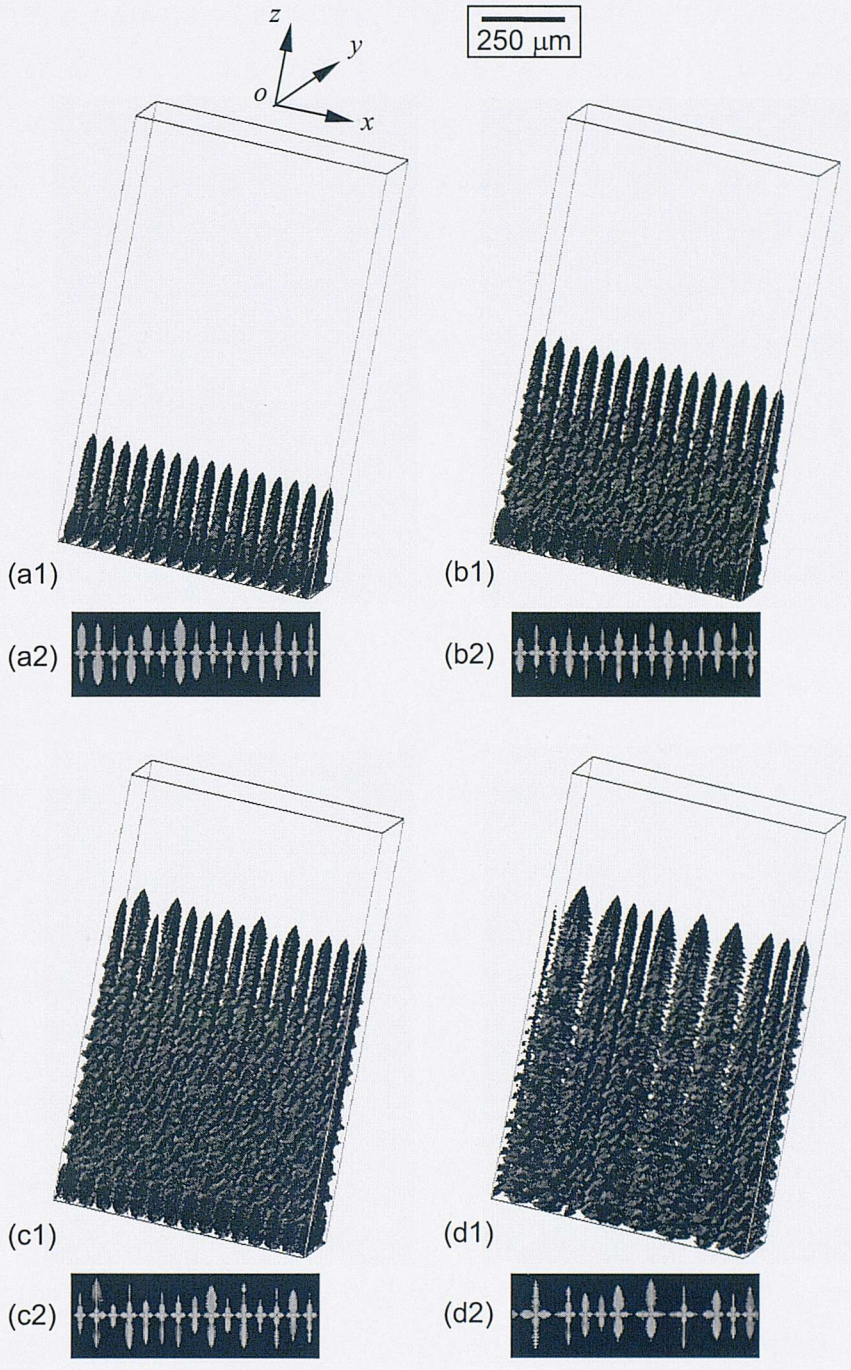

Fig. 5.5 3D simulation for 15 seeds at a solidification time of (a1) 2 s, (b1) 4 s, (c1) 6 s, and (d1) 40 s. (a2) transverse slice at z = 150μm, t = 2 s, (b2) transverse slice at z = 450 μm, t = 4 s, (c2) transverse slice at z = 750 μm, t = 6 s, and (d2) transverse slice at z = 750 μm, t = 40 s.

In the above three simulations all the seeds are centred along the y direction and thus the trunks of the primary dendrites developing from them lie in a plane parallel to the x- and z-axes. The simulations show that the initial seed density has an effect on the final dendrite spacing along the x direction, which varies from 75 to 250 μm, however, the spacings along the y direction are all equal to the domain thickness, 250 μm. The question then arises as to whether the domain size gives rise to artificial effect on the selection of primary dendrite spacing. Simulations in a domain with an adjustable size were carried out, and the results are presented in the following section.

5.2.2 Effect of Domain Size

In the following simulations only one seed was placed at the centre of the base. The domain has a square cross section and the width and the thickness of the domain are equal. Periodic boundary conditions were applied to the side surfaces: all the simulations start with a square packing of dendrites, and the spacings along the x and y directions are the same, which is equal to the domain width/thickness.

Fig. 5.6 (a1) shows the growth of one dendrite in a domain with a width/thickness of 250 μm. No branching is observed in the 40 s of growth, and the resultant structure resembles the dendrites shown in Fig. 5.3 (b1), growing under almost identical conditions. The final spacings along the x and y directions are both equal to the size of the cross section of the domain which is 250 μm.

The width/thickness of the domain is then increased. As shown in Fig. 5.6 (b1), the size of the cross section of the domain is 300 μm, dendrite branching occurs and two new dendrites are generated. If replicating the transverse slide shown in Fig. 5.6 (b2) along both the x and the y directions infinitely, the dendrites no longer form a regular square packing pattern. An average primary dendrite spacing is used to quantify the mean distance between the dendrites, defined as $\lambda_1 = \sqrt{A/n}$, where A is the cross sectional area, and n the number of primary dendrite trunks. In this case, A is 300×300 μm^2 and n is 3, giving an average spacing of 173 μm.

When the cross section of the domain is increased to 350×350 μm^2, 4 new dendrites form by branching (see Fig. 5.6 (c1)), and the resulting average spacing is 157 μm.

When the cross section is increased to 500×500 μm^2, 10 new dendrites are generated (see Fig. 5.6 (d1)), resulting in a final average spacing of about 151 μm.

The simulation results in Fig. 5.6 show that when the size of the cross section is larger than 250 μm, the growth of one dendrite is no longer stable and branching occurs, reducing the average primary dendrite spacing to a smaller value. This poses another question: what will happen if the side size of the cross section of the domain is reduced. If one seed is still used in the simulations, dendrite overgrowth phenomena will not occur and therefore in subsequent simulations four seeds were placed at the base to form an initial square packing pattern.

As shown in Fig. 5.7, the width/thickness of the domain varies from 300 to 100 μm, with the initial value of the average spacing ranging from 150 to 50 μm. When the initial spacing is 150, 100 and 75 μm, the four dendrites can grow in a stable state, maintaining the initial spacing (see Fig. 5.7 (a1), (b1) and (c1)) but when the initial spacing is less than 75 μm, overgrowth occurs as shown in Fig. 5.7 (d1) and (e1). In Fig. 5.7 (d1), it can be seen that when the initial spacing is 60 μm, two of the four dendrites are annihilated after 40 s of growth, resulting in an average spacing of 85 μm. In Fig. 5.7 (e1), when the initial spacing is 50 μm, three of the four dendrites are blocked out, and the average spacing is increased to 100 μm.

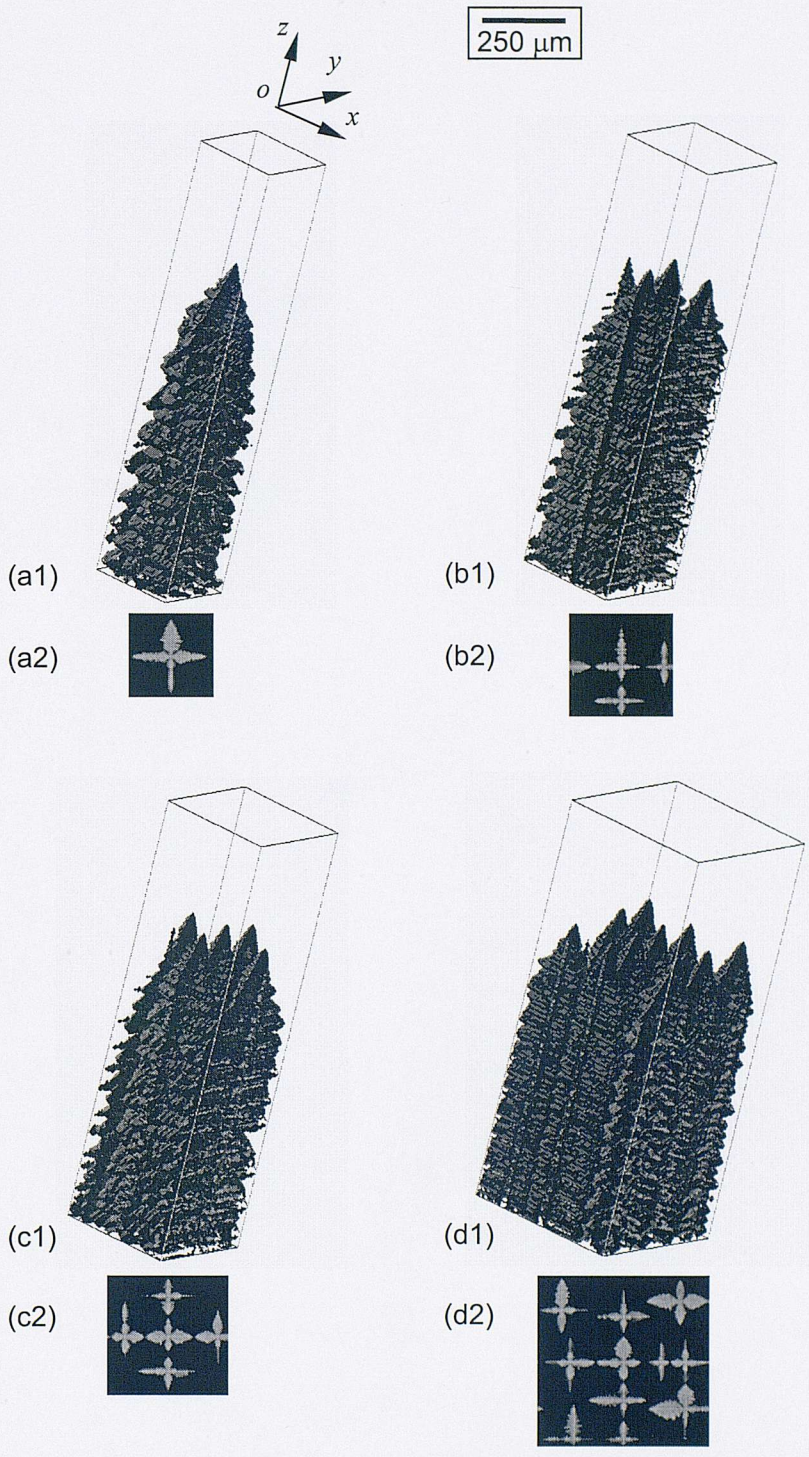

Fig. 5.6 3D simulation results for 1 seed in domains with different transverse section area: (a1) 250×250 μm^2, (b1) 300×300 μm^2, (c1) 350×350 μm^2 and (d1) 500×500 μm^2. (a2), (b2), (c2) and (d2) are transverse slices at z = 750 μm, t = 40 s.

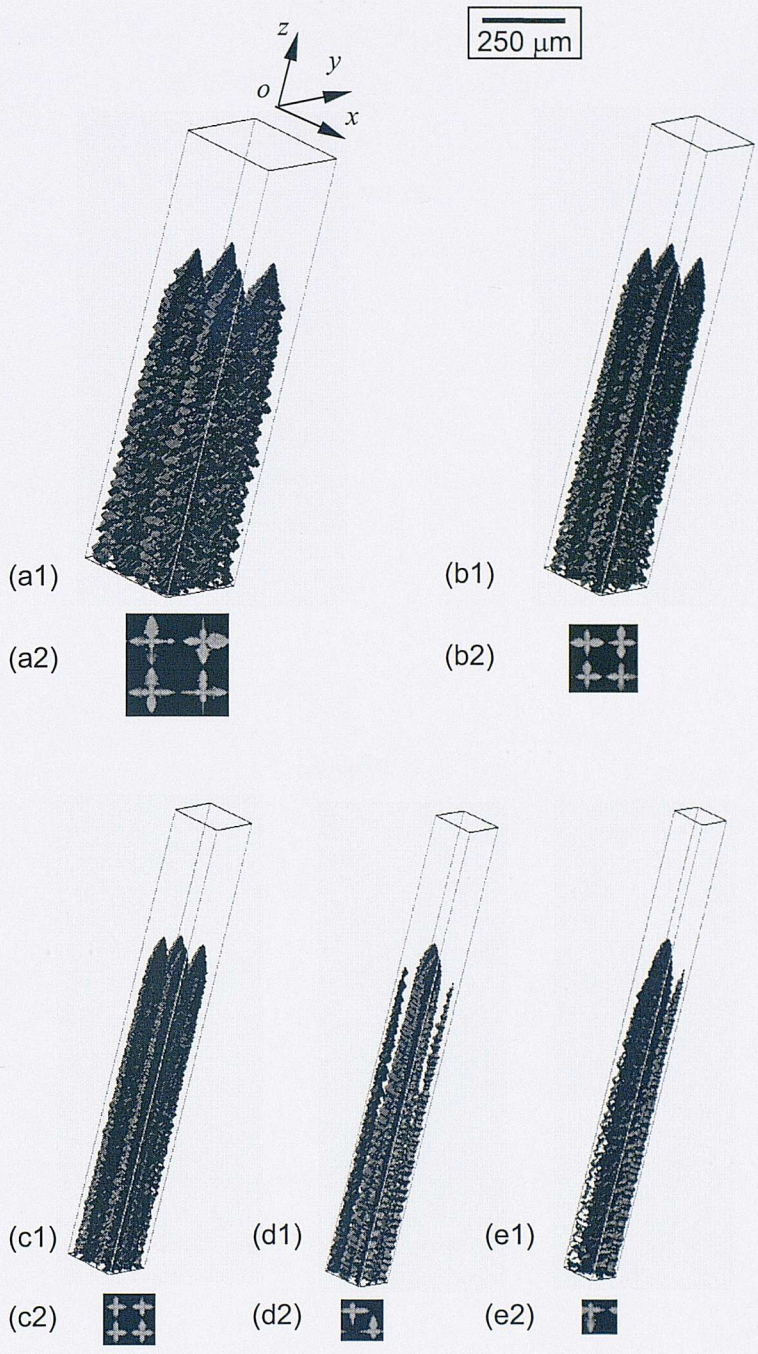

Fig. 5.7 3D simulation results for 4 seeds in domains with different transverse section area: (a1) 300×300 μm^2, (b1) 200×200 μm^2, (c1) 150×150 μm^2, (d1) 120×120 μm^2 and (d1) 100×100 μm^2. (a2), (b2), (c2), (d2) and (e2) are transverse slices at z = 750μm, t = 40 s.

The relationship between the final average primary dendrite spacing and the initial seed spacing (which is equal to the width/thickness of domain when only one seed is placed at the base, or to half of the width/thickness when four seeds are placed at the base) is shown in Fig. 5.8. The initial seed spacing ranges from 50 to 500 μm, and the final average primary dendrite spacing varies between 75 and 250 μm. The upper limit is approximately three times the lower limit.

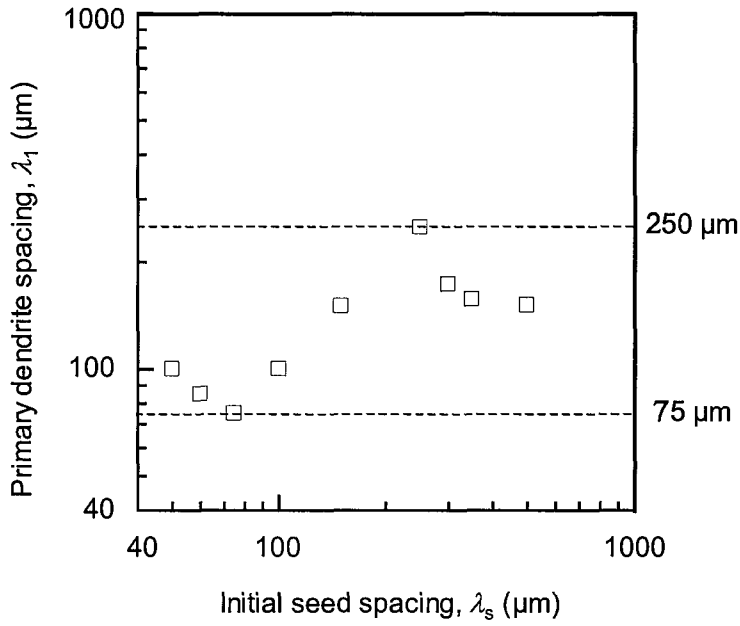

Fig. 5.8 Final stable primary dendrite spacing (λ_1^s) versus the initial seed spacing (λ_1^0) in 3D simulations with adjustable domain.

Since dendrite branching and overgrowth are both random processes, simulations starting with regular square-packed dendrites may not result in the same packing pattern. In the practical solidification process square packing can rarely be achieved and close or hexagonal packing is often obtained for directionally solidified dendrites. Simulations starting with hexagonally packed dendrites were also carried out, and will be presented in the next section.

5.3 Hexagonal Packing of Dendrites

The following simulations were run on a regular grid composed of 150×50×250 cubic cells with a cell size of 5 μm. The imposed solidification conditions in the simulations are: G = 12 K/mm, and V = 150 μm/s. Periodic boundary conditions were applied to the side surfaces. Only growth from existing seeds at the base was considered, and the sites of these seeds were chosen in such a way that the columnar dendrites developing from them would be approximately hexagonally packed.

5.3.1 Effect of Initial Seed Density

Simulations with different numbers of seeds were run to study the effect of the nucleation density on the final solidified structure. Two examples of simulations, one with sparse seeding and one with dense seeding are shown in Fig. 5.9 and Fig. 5.10, respectively. In Fig. 5.9 (a1) only 2 seeds are placed at the bottom giving an initial spacing of approximately 306 μm and their positions are staggered so as not to lie on the same line, parallel to either the x- or the y-axis. As initially the seed spacing is very large, and the solute fields do not interact and so they grow in all directions (see Fig. 5.9 (a1)). After a short time (see Fig. 5.9 (b1)) the solute fields of the secondary arms (perpendicular to the macro solidification direction) interact, slowing their growth. Ternaries grow from these secondaries, in a direction parallel to the primaries, and are initially very closely spaced. Competitive growth caused by solute field interaction result in only a few being selected so that only 6 tertiary dendrites surviving at a solidification time of 6 s, their tips having caught up with the 2 seed primaries (see Fig. 5.9 (c1)). With a new total of 8 primaries, the average spacing has been reduced to 153 μm. This spacing remains stable at a solidification time of 40 s as shown in Fig. 5.9 (d2).

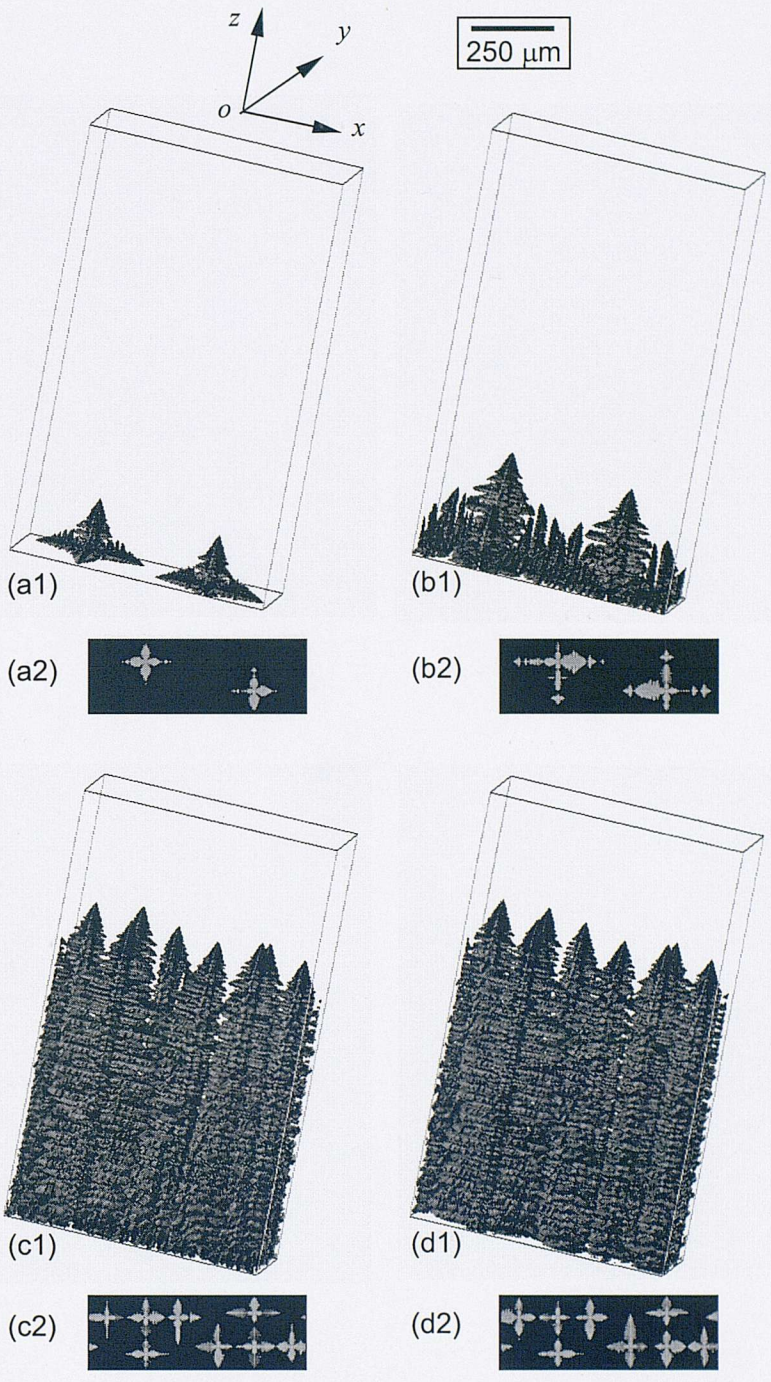

Fig. 5.9 Simulation for 2 seeds at a solidification time of: (a1) 1, (b1) 2, (c1) 6 and (d1) 40 s. (a2) transverse slice at $z = 50\mu m$, $t = 1$ s, (b2) transverse slice at $z = 150$ μm, $t = 2$ s, (c2) transverse slice at $z = 750$ μm, $t = 6$ s, and (d2) transverse slice at $z = 750$ μm, $t = 40$ s.

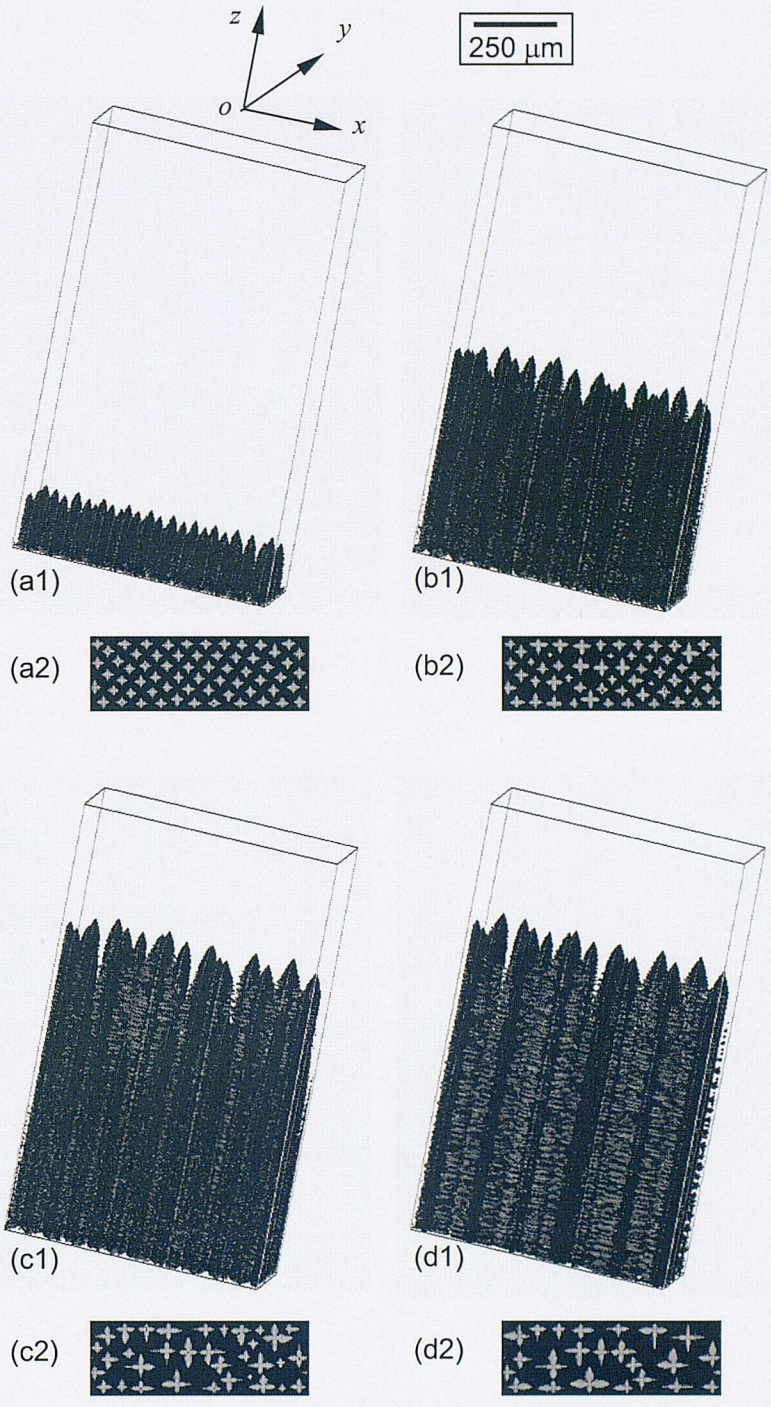

Fig. 5.10 Simulation for 64 seeds at a solidification time of: (a1) 1, (b1) 4, (c1) 6 and (d1) 40 s. (a2) transverse slice at z = 50 μm, t = 1 s, (b2) transverse slice at z = 450 μm, t = 4 s, (c2) is transverse slice at z = 750 μm, t = 6 s, and (d2) transverse slice at z = 750 μm, t = 40 s.

The converse situation, competitive growth of primaries from an initially dense number of nuclei, is shown in Fig. 5.10 where 64 seeds are nucleated at the bottom, giving an initial seed spacing of approximately 54 μm (see Fig. 5.10 (a1)). With such a fine spacing the solute fields overlap so far that the formation of secondary dendrites is almost completely suppressed. Minor variations in the initial spacing cause some of the more restricted dendrites to have a greater tip undercooling (see Fig. 5.10 (b1) and (b2)), with the result that the spacing slowly increases because of competitive growth. This process continues with more and more dendrites being eliminated, as shown in Fig. 5.10 (c1) and (c2) with a stable primary dendrite spacing of approximately 90 μm being reached after 40 s (Fig. 5.10 (d1) and (d2)).

A series of simulations with different initial seed spacings (λ_1^0) were run to explore the relationship between this and the final primary dendrite spacing, with the results plotted as the solid points in Fig. 5.11. The initial seed spacing ranges from 50 to 310 μm, and the final spacing (λ_1^s) varies between 80 and 220 μm, with an upper limit of approximately 3 times the lower limit.

This relationship was compared with that obtained in the simulations starting with square-packed dendrites (see the hollow square points in Fig. 5.11) and it was found that the upper limit of the stable spacing obtained in the simulations starting with hexagonally packed dendrites (220 μm) is slightly lower than with square-packed (250 μm), but the lower limit in hexagonally packed growth (80 μm) is slightly higher that in square-packed growth (75 μm).

The range of values of stable primary dendrite spacings in 3D hexagonally packed growth (80 – 220 μm) was also compared with that obtained in previous 2D simulation (130 – 380 μm), which is plotted as crossing points in Fig. 5.11. Dividing the upper limit of stable spacings in 2D simulations by that in 3D simulations gives a factor of, 380/220 = 1.73, and the factor between the low limit in 2D and 3D simulations is, 130/80 = 1.63. It can therefore be seen that the range of stable spacings shifts to the smaller values in the 3D simulations by a factor of about 1.7 relative to 2D simulations.

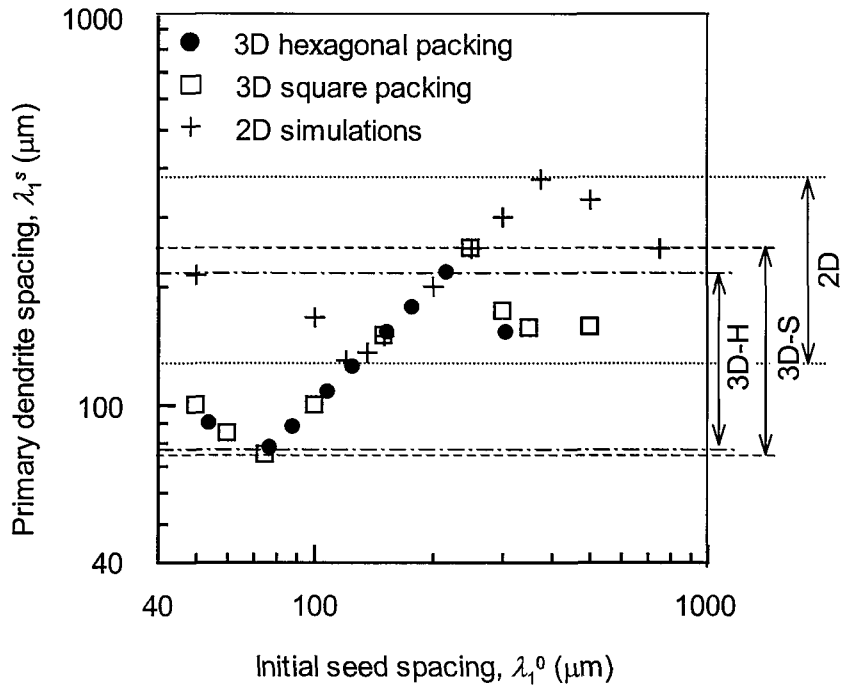

Fig. 5.11 Final stable primary dendrite spacing (λ_1^s) versus the initial seed spacing (λ_1^0) in 2D and 3D simulations.

5.3.2 Effect of Perturbation on Pulling Velocity

It has been demonstrated in Chapter 4 that perturbation of the pulling velocity can reduce significantly the range of the stable primary dendrite spacing. After a cycle of perturbation of the pulling velocity around a mean value, the upper limit of the stable spacing becomes about twice the lower limit. For conditions of G = 12 K/mm, and V = 150 μm/s, the upper and lower limits of stable spacings are 300 and 150 μm respectively.

Similar perturbation of the pulling velocity was also applied to the 3D simulation starting with hexagonally packed dendrites. Fig. 5.12 shows the typical effects of such a perturbation on the predicted results. Initially four dendrites were growing in a stable state with an average spacing of 217 (see Fig. 5.12 (a1). A cycle of perturbation was then applied to the pulling velocity: (i) t = 0 s, V = 150 μm/s; (ii) t = 10 s, V = 300 μm/s; (iii) t = 20 s, V = 75 μm/s; and (iv) t = 30 s, V = 150 μm/s. As shown in Fig. 5.12

(b1) and (b2), the effect of increase in pulling velocity is dramatic with tertiary dendrites forming in the gaps between the primaries. These tertiaries grow fast until their tips almost catch up with those of original primaries from which they branched (see Fig. 5.12 (c1)). The effect of decreasing pulling velocity has less impact, its main effect being to stabilise the tertiaries through overgrowth. After the perturbations the predicted primary dendrite spacing is reduced to about 164 μm, and remains stable after the velocity returns to its pre-perturbation value (see Fig. 5.12 (d2)).

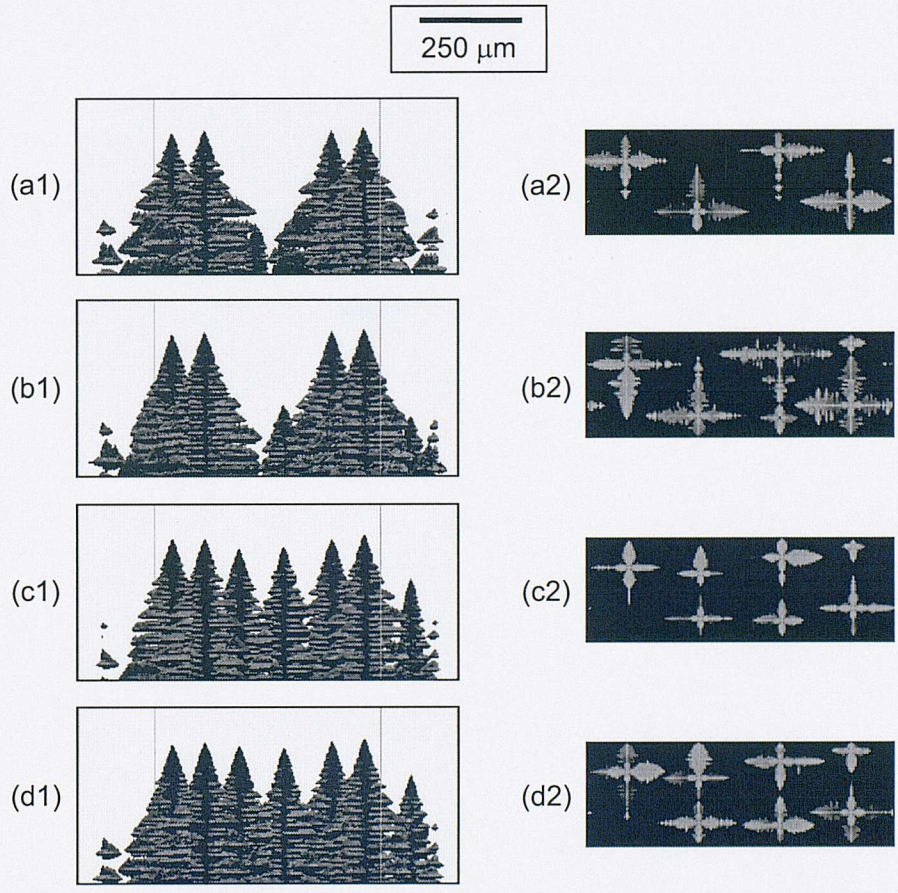

Fig. 5.12 Tip region of a simulation for 4 seeds and a perturbation of the pulling velocity, at a solidification time of: (a1) 40, (b1) 50, (c1) 60, and (d1) 75 s. (a2) transverse slice at z = 750μm, t = 0 s, (b2) transverse slice at z = 500 μm, t = 10 s, (c2) transverse slice at z = 875 μm, t = 20 s, and (d2) transverse slice at z = 750 μm, t = 30 s.

The same perturbation sequence was applied to the entire range of initial seed spacings (see Fig. 5.13), resulting in the stable primary dendrite spacing being reduced from 80 – 220 μm to 95 – 180 μm. The resulting upper limit is about twice the lower limit – i.e. the primary dendrite spacing has reached a much narrower distribution after undergoing a cycle of perturbation of the pulling velocity. Compared with the stable range obtained under the same conditions in 2D simulations (150 – 300 μm), it was again found that both the upper and lower limits shifted to the smaller values by a factor of approximately 1.7.

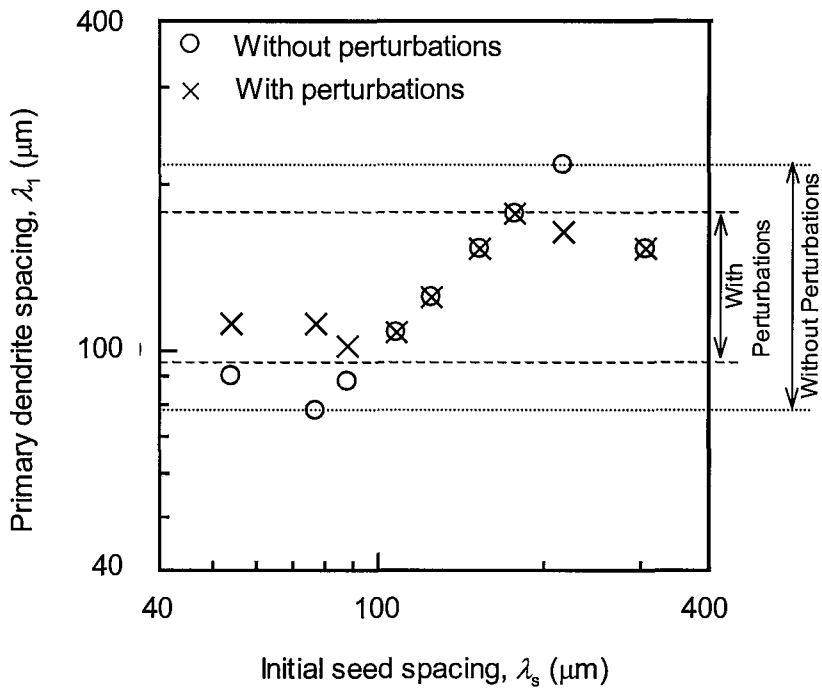

Fig. 5.13 Final stable primary dendrite spacing (λ_1^s) versus initial seed spacing (λ_1^0) in 3D simulations without and with perturbation of the pulling velocity.

5.4 Comparison with Experiments

The simulations under conditions of G = 12 K/mm and V = 150 μm/s suggests that the range of stable spacing is reduced by a factor of approximately 1.7 in 3D relative to in 2D. The 2D simulations show that both the upper and lower limits of stable primary dendrite spacings have a power-law relationship with the pulling velocity, and the upper limit is about twice the lower limit when the solidification undergoes a cycle of perturbation of pulling velocity, as given in equation (4.5). Assuming that this relationship is still true in 3D, and that the power index remains the same, the relationship between λ_1' and V' in 3D can be obtained by reducing the coefficients in equation (4.5) by a factor of 1.7:

$$\begin{aligned} \lambda'_{1\max} &= 7.17\times10^{3}\left(V'\right)^{-0.29} \\ \lambda'_{1\min} &= 3.08\times10^{3}\left(V'\right)^{-0.29} \end{aligned} \quad . \tag{5.3}$$

These two lines are plotted in Fig. 5.14, together with 3D simulation results (triangular points). They are found have very good correlation with Kurz and Fisher's analytical solution (Kurz, *et al.* 1992) and Hunt and Lu's prediction (Hunt, *et al.* 1996). Kurz and Fisher's solution is approximately a midline between the predicted upper and lower limit lines, but the slope is slightly more gradual. Hunt and Lu's prediction fits well between the two limit lines with the slope a little steeper. The predictions are also compared with the experimental results obtained by (Davies, *et al.* 1980; Kermanpur, *et al.* 2000; Wang, *et al.* 2001) and are found to be in good agreement apart from the fact that, at low pulling velocity, some points of experimental results drop below the lower limit.

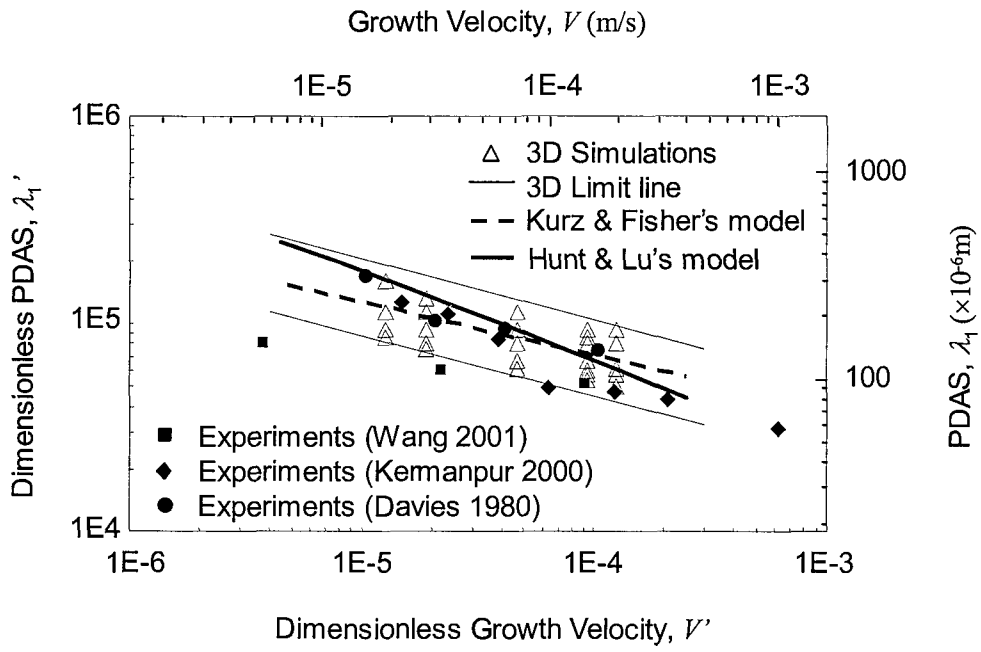

Fig. 5.14 Predicted 3D upper and lower limits of the distribution of primary dendrite spacing, with the 3D simulation results. They are compared with Kurz and Fisher's solution (Kurz, *et al.* 1992) and Hunt-Lu's prediction (Hunt, *et al.* 1996) and previous experimental results (Davies, *et al.* 1980; Kermanpur, *et al.* 2000; Wang, *et al.* 2001).

5.5 Summary

As with 2D, the 3D simulations show that there is a range of stable spacings for columnar dendrites in directional solidification. Perturbation on the pulling velocity affects both the primary dendrite spacing and the tip undercooling. The primary dendrite spacing has a much narrower distribution after perturbation and the upper limit of the distribution of primary spacing is about twice the lower limit. Unlike the 2D simulations, the whole range of stable spacings shifts towards smaller values by a factor of about 1.7. The results show good correlation with earlier computational and experimental results.

Chapter 6
Simulation of Solidification at Geometrical Discontinuities

Single crystal (SX) nickel-based superalloys are the current state-of-the-art for producing gas turbine blades that satisfy the stringent quality required to ensure mechanical integrity at the high operating temperature of modern engines. The final casting integrity of these parts, which are produced by the unidirectional solidification process, depends upon their microstructures and inherent defects (McLean 1983). Many types of performance-limiting crystal defects, such as freckles, stray grains, recrystallised grains, low-angle boundaries and microporosity can occur in a SX part. Some of these defects are difficult to eliminate in large, complex shaped blades. The mechanisms for formation of these defects are known in a general sense and some progress has been achieved in identifying their origins and quantifying their causes (Meyer ter Vehn, *et al.* 1996; Schaefer, *et al.* 1997; D'Souza, *et al.* 2000). Given the cost constraints associated with design and manufacture of the SX parts, casting designers have become increasingly reliant on modeling and simulation of the casting process in order to be able to produce defect-free components.

6.1 Introduction

It is known that some types of defects in SX parts are related to the curvature of the liquidus isotherm while it is passing through enlargements in the cross section of the component (e.g. the platform of a turbine blade) (Paul, *et al.* 1993). This condition is exacerbated when several blades are cast in a cluster (Copley, *et al.* 1970; Napolitano, *et al.* 2000). Fig. 6.1(a) schematically depicts the liquidus isotherm plane in a turbine blade being cast as part of a cluster of blades (Napolitano, *et al.* 2000). The through-thickness thermal gradient can be seen from the outward facing side (side A) to the inward facing side (side B). It has already been observed that freckle channels tend to occur at the steepest regions of the solid-liquid interface, i.e. towards side A (Copley, *et al.* 1970). Indeed, this type of asymmetric concave upward solidification, interacting with the platform geometry, can result in increasing defects. The longitudinal section of the blade is shown in Fig. 6.1(b). As the solidification front approaches the platform at time of t_1, a significant degree of undercooling develops in the liquid within the platform on the side A (i.e. dark grey region in Fig. 6.1(b)). As the front passes the mould corner, $t=t_2$, lateral growth of secondaries from the original primary dendrite

into the platform is very fast due to the high undercooling (i.e. light grey region in Fig. 6.1(b)). This can generate a complex branching pattern of the dendritic structure, such as that at time of t_3. Alternatively, when there is a sufficient undercooling, new grains may nucleate stray grain defects, which grow into the undercooled melt. On the inward side B of the casting, a quite different situation is observed. The undercooling in the platform is only that necessary to drive the motion of the dendrite tips. The front is free to follow the isotherm and is never constrained geometrically, as it is on side A. The result in this case should be a well-ordered dendritic structure. Clearly, it can be concluded that the probability of the formation of structural defects is largely dependent on the curvature of the solidification front, which in turn depends on the geometrical arrangement of the cluster. Prior models presented so far (e.g. (Napolitano, *et al.* 2000)) have not been able to simulate the full dendritic microstructure in such conditions.

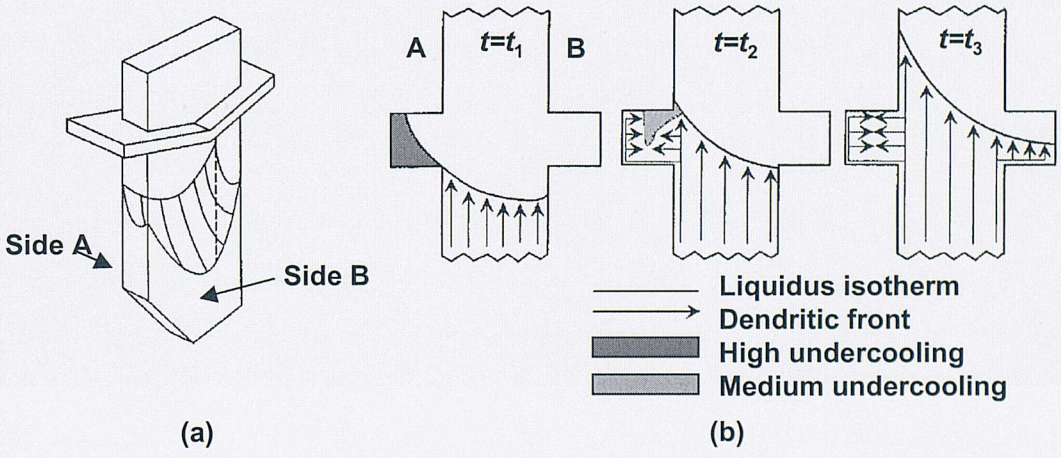

Fig. 6.1 (a) Schematic of the isotherms estimated from the microstructure by Napolitano et al. for a SX blade cast in a cluster. (b) Schematic of the growth into the platform region, illustrating the difference in the dendritic patterns due to the effect of the platform geometry and the through-thickness gradient. Side A is outward facing, while side B is inward facing (after (Napolitano, *et al.* 2000)).

The CA-FD model presented in Chapter 3 has been used to investigate the effect of changes in both the cross sectional area (i.e. geometrical discontinuities) and the shape of isotherms on dendrite growth during SX solidification of a binary approximation of a nickel-base superalloy. The dendritic structure formed in SX solidification when passing an increase in cross-sectional area was simulated with a range of different imposed isotherm shapes. The simulation results were compared with the experimental observations of Napolitano et al. (Napolitano, *et al.* 2000).

6.2 Results and Discussions

In order to demonstrate the effect of mould geometry on dendritic growth, the platform region of a turbine blade (see Fig. 6.2) was chosen as the simulation domain. The domain is 5.5 mm wide and 8 mm high containing a mould wall (the hatched zone in Fig. 6.2) with a thickness of 0.5 mm. The domain was then discretised using a regular grid of 5 μm square cells. A zero-flux boundary condition was applied at all boundaries. Different thermal conditions were applied in the simulations to investigate the effect of the temperature field on the growth pattern of dendrites.

6.2.1 Horizontal Isotherms

Firstly, the thermal condition of horizontal isotherms with a temperature gradient of 12 K/mm moving upwards at a constant velocity of 150 μm/s was considered. The predicted dendritic structure and undercooling profiles at different times are shown in Fig. 6.2 and Fig. 6.3, respectively. A grain was placed at the bottom-right corner of the domain, with one of its <10> directions fully aligned with the vertical temperature gradient. After 11s growth, the grain starts to propagate a secondary dendrite around the mould corner. A significant degree of undercooling develops in front of the secondary dendrite as the macroscopic solidification proceeds vertically, reaching 20.7 K, which is about twice that in front of the original primary dendrite, 10.8 K. As a result of the high undercooling, the secondary dendrite grows at a much faster rate than the primary dendrite. After 14 s, the secondary dendrite approaches the outside vertical wall of the platform, with the tip undercooling having increased to 26.1 K. In the platform region, many tertiary dendrites emanate with a random initial spacing on both sides of the developing secondary dendrite. However, because of the constraint of the

mould wall, only those facing upward can grow. The spacing between these new columnar dendrites is quickly reduced through an overgrowth mechanism. Although the tertiary dendrites near the outside wall are formed much later than those near the centre, they grow much faster because of higher tip undercooling. The macroscopic solidification front rapidly approaches the shape of isotherms. Meanwhile, the degree of maximum undercooling decreases to approach that in front of the original primary dendrite. After 25 s, an almost flat front is achieved, and the maximum undercooling near the dendrite tips is reduced to 13.3 K, just marginally higher than the tip undercooling of primary dendrite, 11.4 K. Finally, a well-ordered dendritic structure is obtained at 30s, when the solidification front passes the platform region, with all the tertiary dendrites terminating at the upper wall of platform. This simulation shows that, for horizontal isotherms, the abrupt change in the cross section of the mold results in a significant increase of undercooling in front of the lateral secondary dendrite near the lower wall of the platform. This can reach a value more than twice the tip undercooling of the primary dendrite, and if heterogeneous nuclei were present, there would be a much greater chance of stray grains forming. The tertiary dendrites emanating from the secondary grow rapidly, reducing the undercooling difference with the original primary, until the tertiary and primary dendrite tips become isothermal.

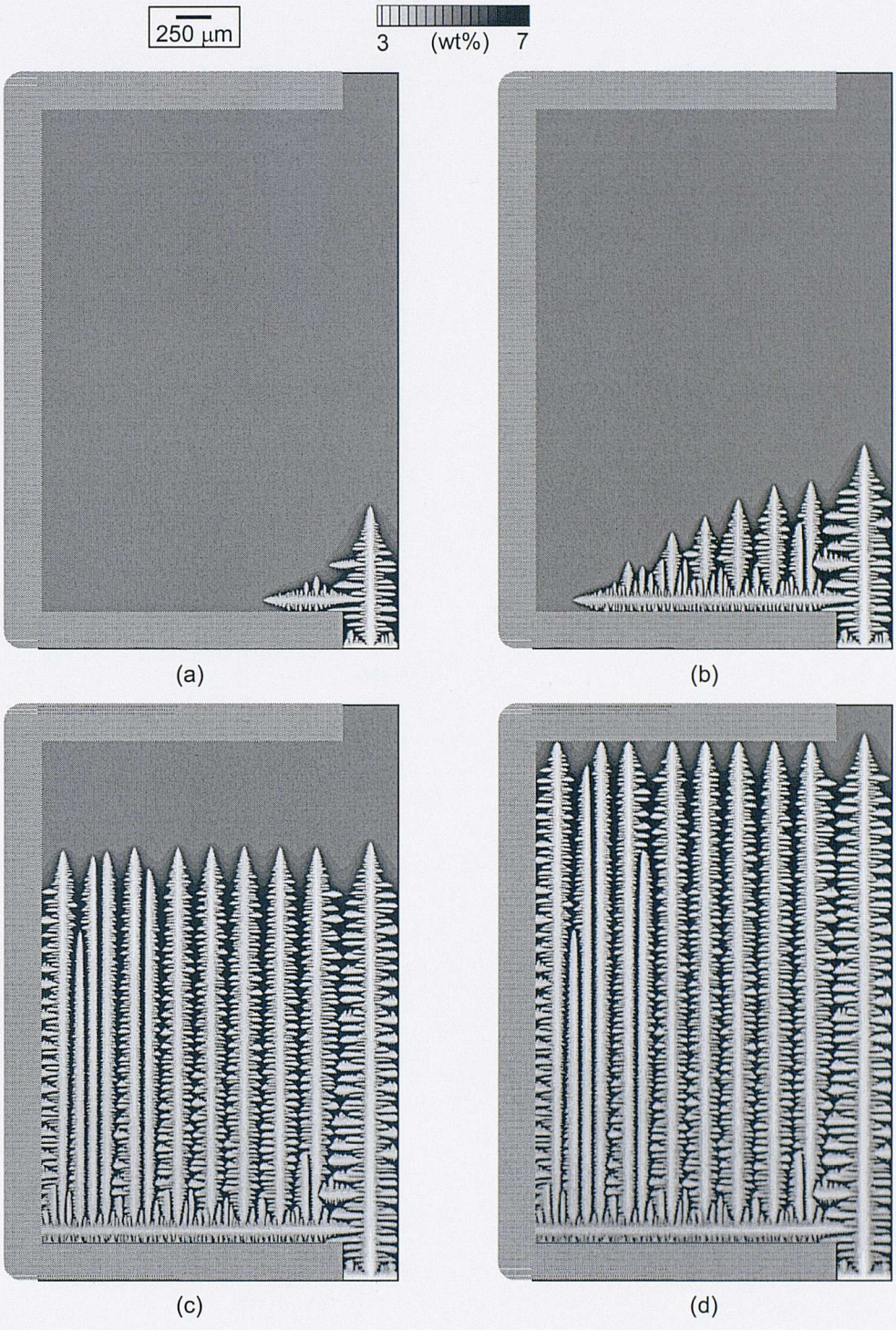

Fig. 6.2 Predicted dendritic structure under thermal conditions of horizontal isotherms moving at a constant velocity of 150 μm/s: (a) t = 11 s; (b) t = 14 s; (c) t = 25 s; (d) t = 30 s.

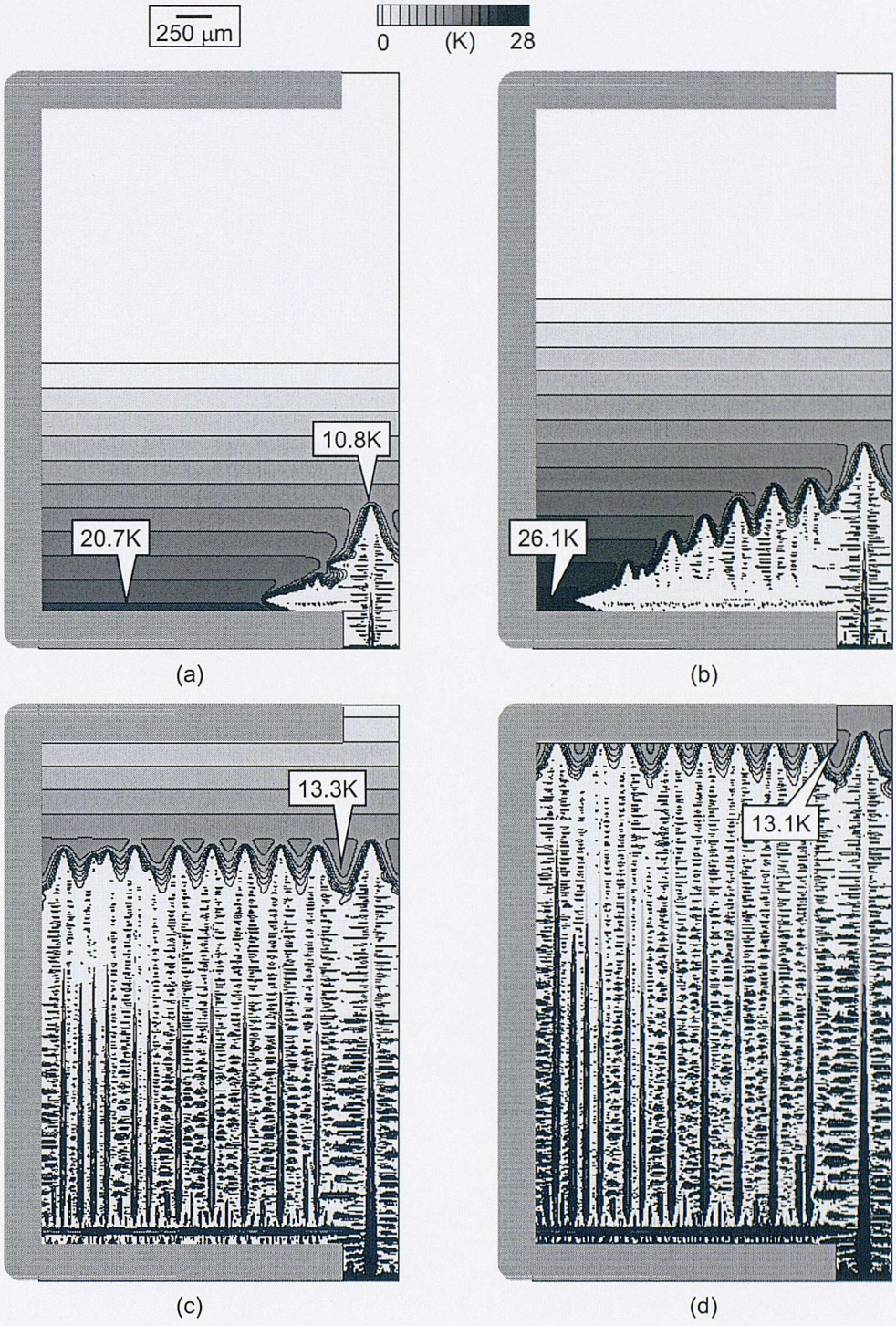

Fig. 6.3 Predicted undercooling distribution under thermal conditions of horizontal isotherms moving at a constant velocity of 150 μm/s: (a) t = 11 s; (b) t = 14 s; (c) t = 25 s; (d) t = 30 s.

6.2.2 Inclined Isotherms

In the second example, the effect of the direction of the temperature gradient was investigated. As shown in Fig. 6.5, the temperature gradient was inclined at 45° relative to the macroscopic solidification direction and the magnitude of the gradient was the same as in the previous case, 12 K/mm. Comparing Fig. 6.2 and Fig. 6.4, it is found that at the early stage of growth (for $t \leq 15$ s), the development of the dendritic microstructure is very similar. However, they diverge after 15 s because of the effect of the inclined isotherms on the tip undercooling and growth. After 19 s of growth the solidification front approaches the 45° inclination of the isotherms (see Fig. 6.4 (c)). Moreover, the fine dendritic structures also exhibit some differences. In Fig. 6.2 all the tertiary dendrites grow symmetrically, but in Fig. 6.4, they develop asymmetrically, with more branches on the right hand side than the left hand side. Because of the inclination of the isotherms, an even higher undercooling develops as high as 39.6 K at the left-bottom corner, which is nearly four times that in front of the primary dendrite, 10.9K. The propensity for stray grains to nucleate is even greater than with horizontal isotherms. The change in the direction of temperature gradient, can clearly affect both the macro- and micro-scale dendritic structures, as well as the maximum undercooling.

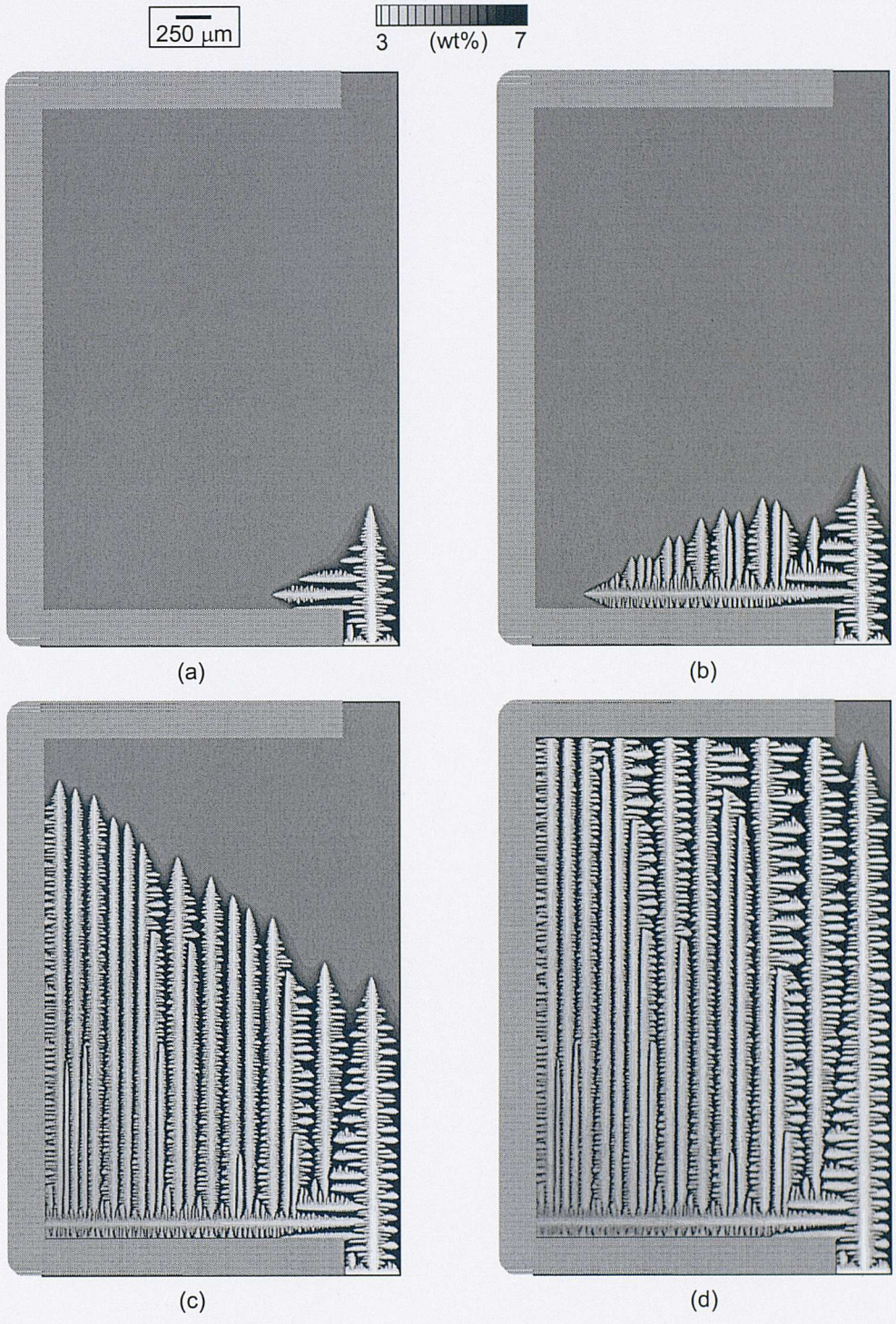

Fig. 6.4 Predicted dendritic structure under thermal conditions of 45° inclined isotherms with respect to the growth direction moving at a constant velocity of 150 μm/s: (a) t = 11 s; (b) t = 13 s; (c) t = 19 s; (d) t = 30 s.

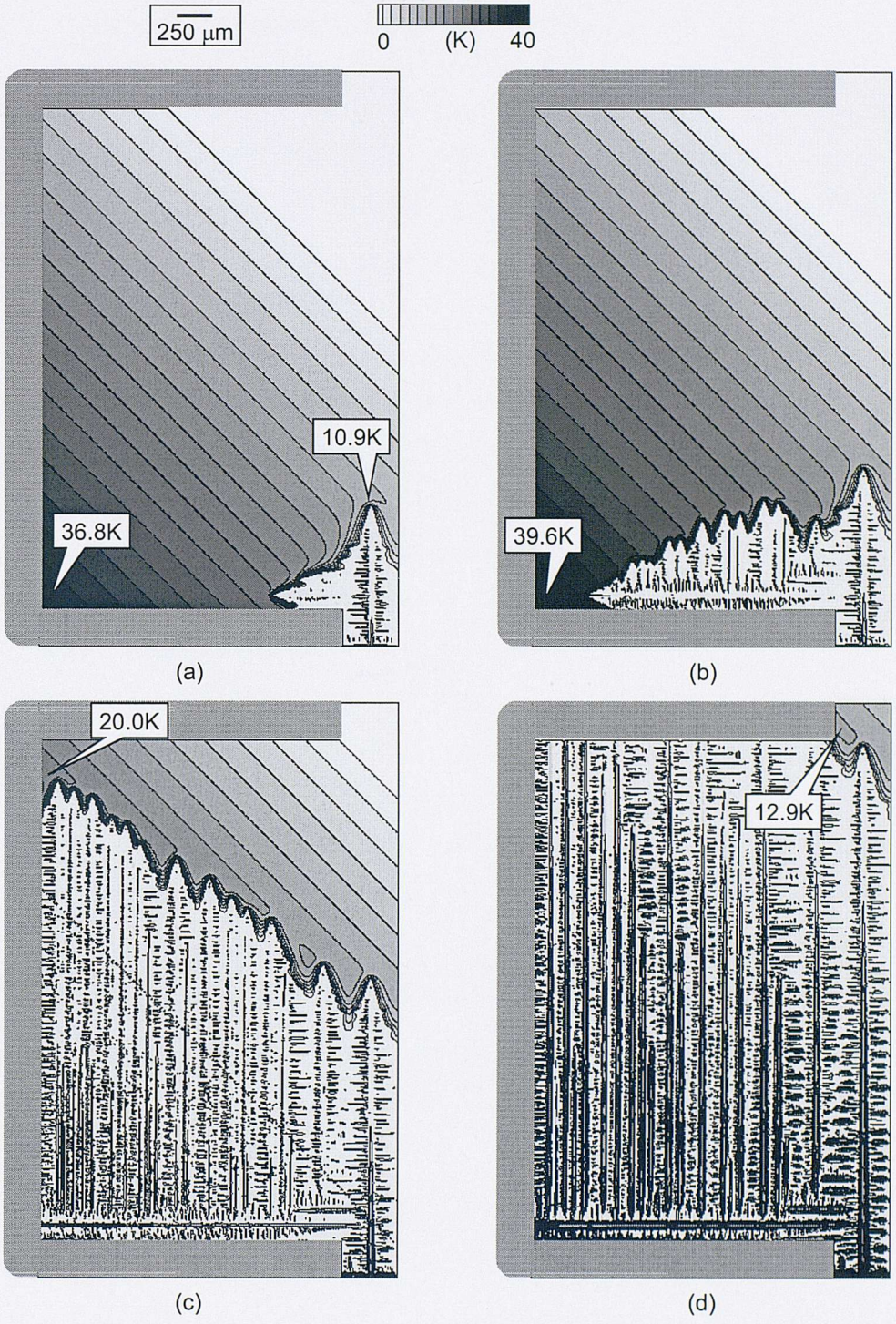

Fig. 6.5 Predicted undercooling distribution under thermal conditions of 45° inclined isotherms with respect to the growth direction moving at a constant velocity of 150 μm/s: (a) t = 11 s; (b) t = 13 s; (c) t = 19 s; (d) t = 30 s.

6.2.3 Concave Isotherms

In the work of Napolitano et al. (Napolitano, *et al.* 2000), they suggest that the true isotherm shape is concave (Fig. 6.1 (b)). This shape was simulated using a polynomial function (Fig. 6.6). For the example shown, at the outside wall, the value of temperature gradient is about 20 K/mm, while at the centre it is about 6 K/mm (with a mean temperature gradient of approximately 12 K/mm). The direction of the gradient relative to the vertical direction varies from 70° at edge to 0° at the centre. Fig. 6.7 shows the undercooling ahead of the dendrites at different times, and the maximum undercooling in the corner reaches 44.4 K, a little more than four times higher than that ahead of the primary dendrite, 10.8 K. Fig. 6.6 shows the evolution of the dendritic structure, with the fastest growth direction marked out by a white arrow at each time. At an early stage (see Fig. 6.6 (a)), the secondary dendrite grows very fast from right to left, until it reaches the outside wall of the platform. Thereafter, the upward tertiary dendrite near the outside wall reaches a maximum growth velocity, growing from the bottom to the top in 9 seconds. During the same time, the original primary dendrite only extends a distance one-fifth of that traversed by the fastest growing tertiary. As the tertiary dendrites approach the upper wall, they branch again. The small dendrites growing from left to right, block the growth of other relatively slow growing tertiary dendrites. However, eventually all these lateral branches are stopped by the original primary dendrite and a complex dendritic pattern is obtained, with a boundary between differently oriented dendrites, similar to a grain boundary, being formed.

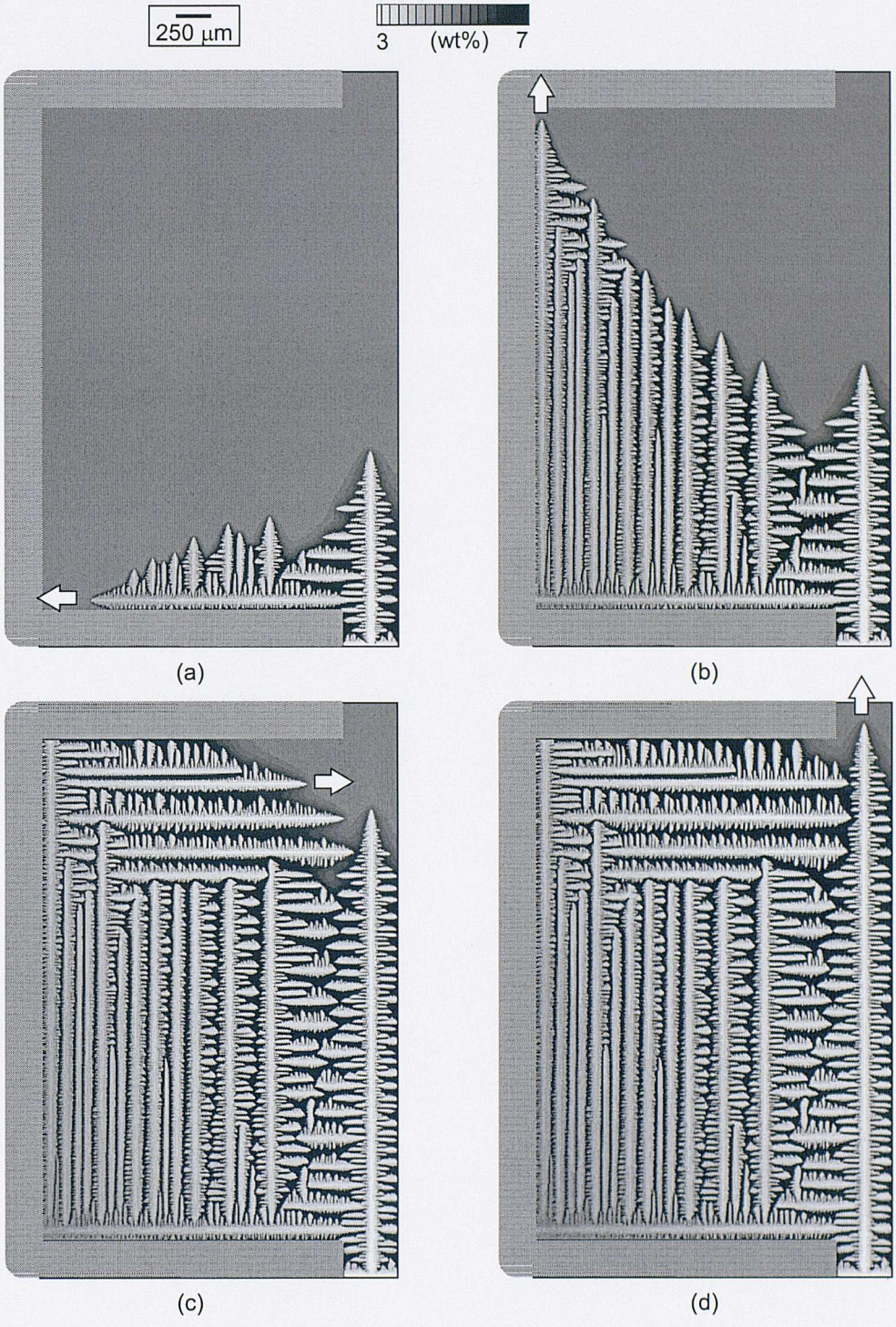

Fig. 6.6 Predicted dendritic structure under thermal conditions of concave isotherms, as suggested by Napolitano *et al.* (Napolitano, *et al.* 2000), moving at a constant velocity of 150 μm/s: (a) t = 16.5 s; (b) t = 21 s; (c) t = 30 s; (d) t = 34 s.

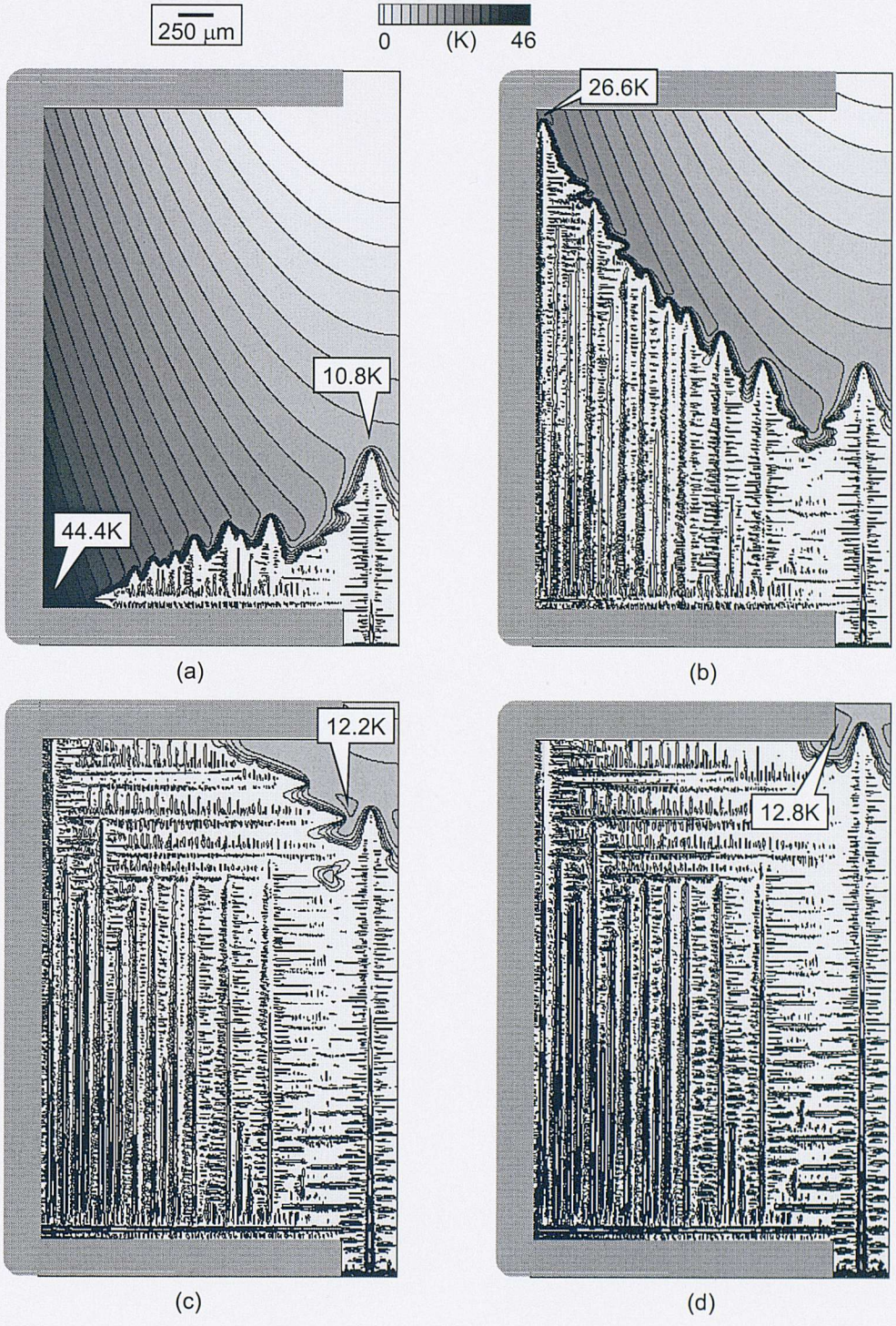

Fig. 6.7 Predicted undercooling distribution under thermal conditions of concave isotherms, as suggested by Napolitano *et al.* (Napolitano, *et al.* 2000), moving at a constant velocity of 150 μm/s: (a) $t = 16.5$ s; (b) $t = 21$ s; (c) $t = 30$ s; (d) $t = 34$ s.

6.3 Comparison with Experiments

The simulation results are compared with the microstructures observed experimentally by Napolitano et al. (Napolitano, *et al.* 2000) in a nickel-based superalloy as discussed earlier. In the experimental micrograph (see Fig. 6.8 (b)) the boundary between the differently oriented dendrites is marked by a dashed line. The simulation shows excellent correlation with the experimental result. The model has correctly predicted the complex dendrite branching pattern happening in the platform region that results in a self-convergent boundary. The region near the boundary will be the last solidified part in the platform, where the solute segregation is the highest and non-equilibrium eutectic phase can form.

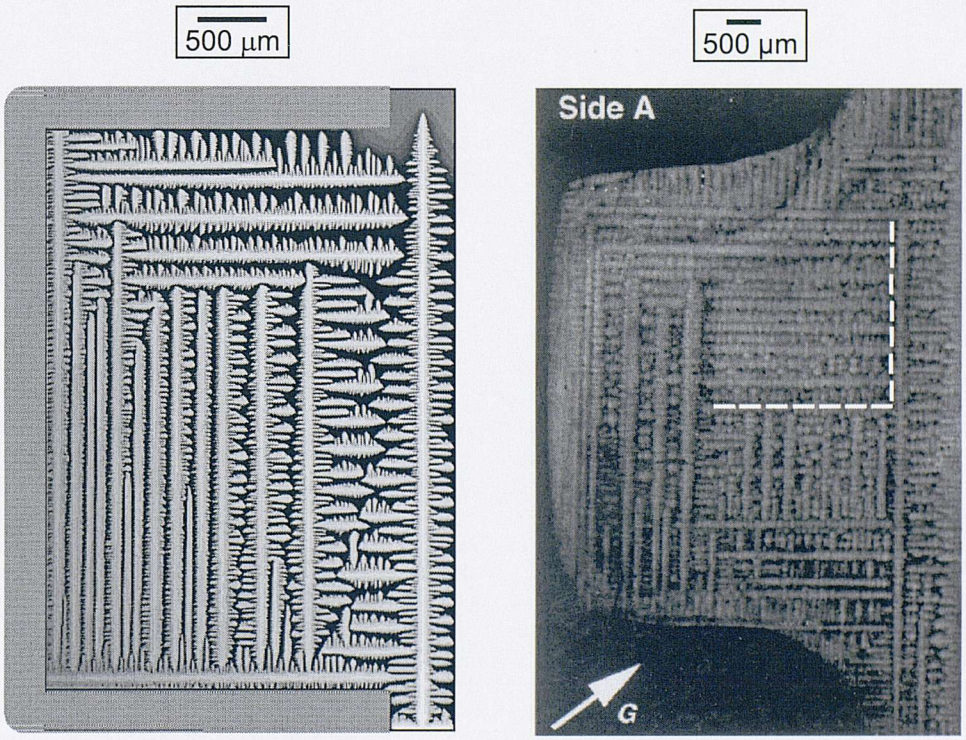

Fig. 6.8 (c) The complex branching dendritic microstructure predicted by the present CAFD model. (b) The microstructure experimentally observed by Napolitano et al. at the outward facing platform section of a SX Ni-based superalloy blade (after (Napolitano, *et al.* 2000)).

In terms of the functionality of the SX components, the occurrence of these complex self-convergent dendritic structures should be avoided, both in terms ensuring consistent properties and because the high undercoolings occurring increases the chance of stray grains forming. Application of the current model should allow the operating parameters of the SX system to be adjusted so that a well-ordered uniform columnar dendritic structure is achieved throughout the entire component. Although the current model gives a good qualitative prediction of the complex dendrite branching pattern in the platform region under conditions of imposed polynomial isotherms, a fully coupled macro-micro model which incorporates both thermal calculations and solidification simulation would allow the effect of latent heat to be considered and thus give more realistic results.

Chapter 7

Simulation of Competitive Growth

The implementation of single-crystal technology in the production of gas turbine blades has greatly improved the properties of the final product, such as creep and thermal fatigue resistance (Wagner, *et al.* 2001). Full exploitation of the benefits of the single crystal technology depends on the effective control of the solidification process, ensuring the deviation of the crystal orientation from the thermal gradient direction is restricted within a few degrees of the preferred growth direction [001]. Grain selection mechanisms play an important role in producing directionally solidified (Gandin, *et al.* 1995) (DS) and single crystal (D'Souza 1999) (SX) nickel-based superalloy gas turbine blades. If the orientation is selected via 'pig-tail' grain selectors, the alloy at first solidifies as a selection of randomly oriented fine grains. Those grains which have one of the <001> preferred growth directions closely aligned with the thermal gradient grow faster than, and eventually eliminate, the other grains with greater deviations. As a result of the grain selection a sharp texture is achieved in the final component. However, in certain situations the misorientated grains have been observed to overgrow sharply oriented grains, giving a diffuse texture.

To obtain better understanding of the grain selection process, the CA-FD model was applied to simulate competitive growth between aligned and inclined dendrites during directional solidification, with the results presented and discussed in this chapter. Good qualitative correlation was found between the predictions and experimental results. However, the model was found to have some limitations in carrying out quantitative investigation on this problem; a phase field model was therefore used to enhance the investigations.

7.1 Cellular Automation Simulation of Competitive Growth

A modified decentred square growth algorithm has been incorporated into the 2D CA-FD model which allows simulation of the growth of grains with random misorientation with respect of the grid. And the competitive growth between grains with different misorientation relative to the macroscopic solidification direction can therefore been studied.

7.1.1 Effect of Misorientation on Tip Undercooling

In the following simulations thermal conditions of G = 12K/mm and $V = 1.5 \times 10^{-4}$ m/s were imposed. The simulations were run on a domain composed of 300×600 cells with a cell size of 5 μm. Periodic boundary conditions were applied to the lateral sides of the domain. At the beginning of each simulation, several seeds were placed at the bottom. These seeds were assigned with different misorientations, ranging from 1 to 30 degree. As solidification proceeds, columnar dendrites develop from these seeds. They are not aligned with respect to the grid, but inclined at the angle of misorientation associated with the seeds. Part of the simulation domain is shown in Fig. 7.1 for the cases with misoriented seeds.

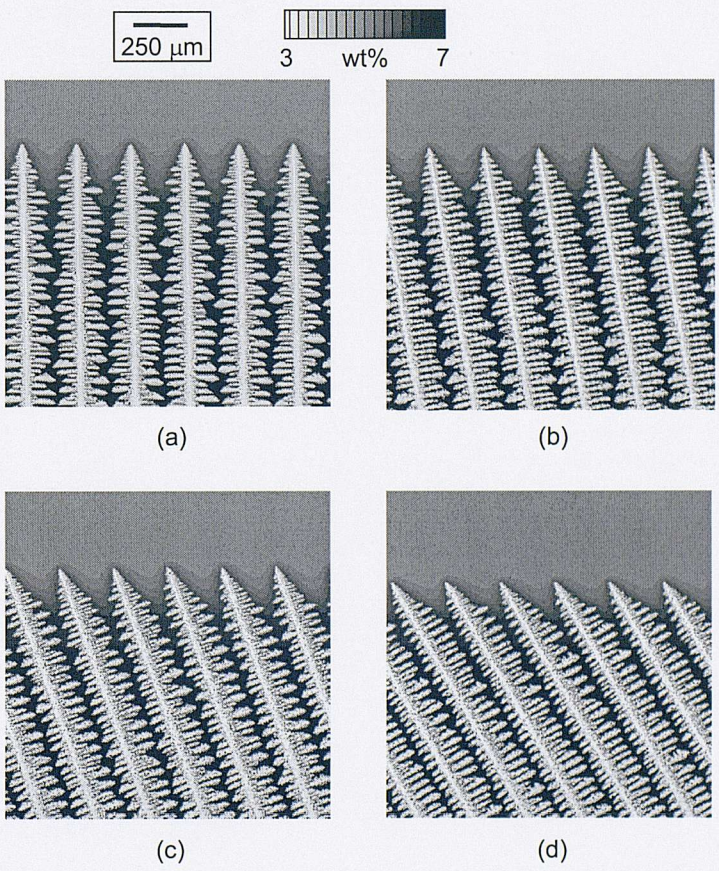

Fig. 7.1 Predictions of columnar dendrite morphologies with different misorientations to the thermal gradient: (a) 1°, (b) 10°, (c) 20° and (d) 30°.

In Fig. 7.1, the columnar dendrites have different misorientations: (a) 1°, (b) 10°, (c) 20° and (d) 30°, and their microstructures also show some differences. In Fig. 7.1 (a), the dendrites are almost aligned with the temperature gradient, with only 1° deviation, and the secondary dendrites developing from the primary dendrites are both nearly perpendicular to the thermal gradient, and show very good symmetry in their microstructures. However, the symmetry in the secondary dendrites doesn't exist in other cases, as shown in Fig. 7.1 (b), (c) and (d), where the preferred growth orientations significantly deviate from the thermal gradient. In these cases, the secondary dendrites exhibit more development on the side of primary dendrites facing the solidification front than the other side.

The relationship between the dimensionless undercooling at the dendrite tip position, calculated as $\Delta T' = \Delta Tk/(mC_0(k-1))$, and the misorientation, θ, is plotted in Fig. 7.2. The tip undercooling increases as the misorientation increases, agreeing with the theoretical analysis of Rappaz and Gandin (Gandin, *et al.* 1993).

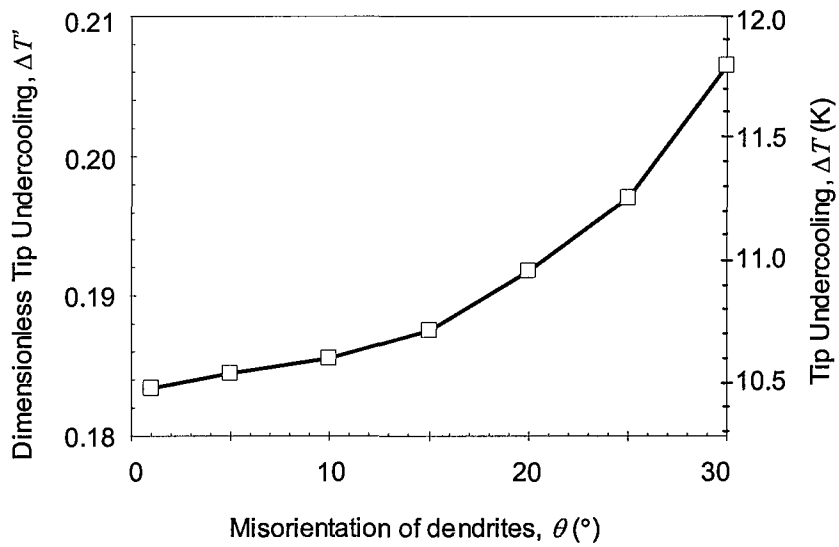

Fig. 7.2 Tip undercooling vs. dendrite misorientation.

7.1.2 Simulation of Converging and Diverging Grains

Simulation was carried out for competitive growth between two converging grains. As shown in Fig. 7.3(a), grain A has a misorientation of 1°, grain B has a misorientation of 15° with respect to the thermal gradient, and they are growing towards each other. As grain A has a lower tip undercooling than grain B due to its smaller misorientation, it grows ahead of grain B. The growth of secondary dendrites at the edge of grain A is suppressed as the primary dendrites in grain B approach it. Also the secondary dendrites in grain B adjacent to grain A develop in an asymmetric manner; they are suppressed on the side next to grain A, but develop on the side away from it. Finally the primary dendrites of grain B stop growing at the edge of grain A. This simulation was found to have good agreement with the experimental result carried out by Wagner *et al.* (Wagner, *et al.* 2001) for CMSX4 superalloy (see Fig. 7.3(b)).

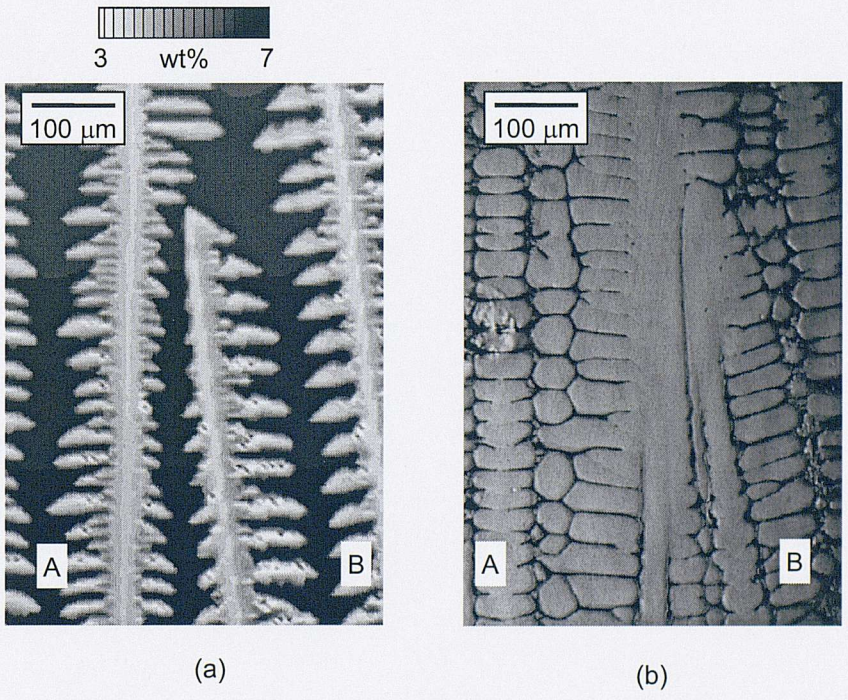

Fig. 7.3 (a) Predicted and (b) experimental results (Wagner, *et al.* 2001) of competitive growth for two converging grains, A and B, with misorientations of 1° and 7°, respectively.

Simulation was also carried out for two diverging grains. As shown in Fig. 7.4 (a), two grains with 1° and 25° misorientations, are grown in diverging directions. Tertiary dendrites emanate from the secondary dendrites in both grains to fill the diverging gap. The boundary between the two simulated grains is nearly a straight line, with a misorientation of approximately 7°, or more closely aligned to the oriented grain rather than the misoriented one. The reason is that, although the primary dendrites in the grain B are better aligned than those in grain A, the secondary dendrites of grain B are in better alignment (inclined at 65°) than those in grain A (inclined at 89°) with respect to the thermal gradient. Therefore the growth of the secondary dendrites in grain A restrain the branching and generation of tertiary dendrites in grain B. Again, the predictions show excellent qualitative agreement to the experiments of Wagner *et al.* (Wagner, *et al.* 2001).

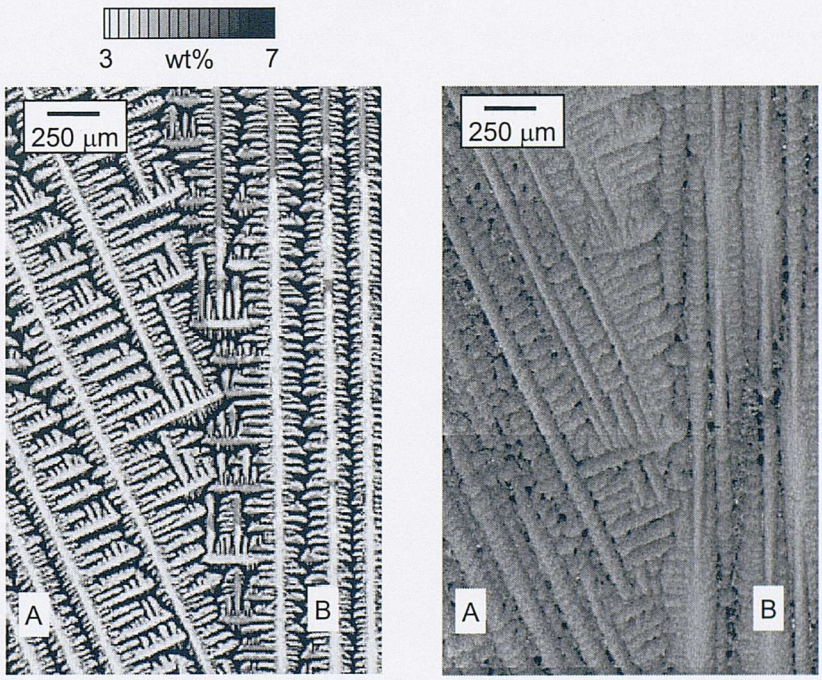

Fig. 7.4 (a) Predicted and (b) experimental results (Wagner, *et al.* 2001) of competitive growth for two diverging grains, A and B, with misorientations of 25° and 1°, respectively.

7.1.3 Summary

The simulation results have shown that the current model is capable of reproducing dendrite morphology, predicting the relationship between tip undercooling and the misorientation of dendrites. The model is also capable of simulating competitive grain growth both at converging and diverging grain boundaries, with good correlation to experimental results. However, problems are also found that the resolution is not high enough. The simulations was run on a grid with a cell size of 5 μm, which is not small enough to reproduce the correct shape of the primary dendrite tips. If a higher resolution is needed, a much finer grid must be used. However, as shown in Chapter 4, the dependence of network grid size has not yet been resolved in the model, and when the cell size changes, the predicted tip undercooling also changes, which makes the prediction unreliable.

To find an alternative solution, a phase field model, which is believed to have higher numerical resolution and less network grid dependency, was used to carry out a complementary investigation on competitive growth.

7.2 Phase Field Simulation of Competitive Growth

The phase field method solves solid/liquid free boundary problems by introducing a diffuse transition layer instead of explicitly tracking a sharp interface as in CA models. Not only constitutional undercooling and curvature undercooling but also kinetic undercooling which is neglected in the CA-FD model, are taken into consideration to calculate the velocity of the solid/liquid interface. The anisotropy of the crystal lattice is considered by introducing an anisotropic term in the interfacial mobility and/or interfacial energy. The phase field model developed by Steinbach and his colleagues (Steinbach, *et al.* 1998b; Tiaden, *et al.* 1999) was used to simulate competitive growth in directional solidification. For the details of the phase field model theory please refer to Chapter 2.

Simulations were performed for a binary alloy, Ni 0.1wt% Hf, with the properties given in Table 7.1. The simulations were run on a regular grid with a cell size of 1 μm,

and the time step is 2.5×10^{-4} s. Both the cell size and time step are much smaller than those used in the cellular automaton simulations.

Table 7.1 Parameters used in phase field simulations

Parameter	Symbol	Value
Initial concentration	C_0	0.1 wt%
Equilibrium partition coefficient	k	0.11
Liquidus temperature	T_{Liq}	1656 K
Solidus temperature	T_{sol}	1607 K
Liquidus slope	m_L	-60.6 K/wt%
Solidus slope	m_S	-550.6 K/wt%
Diffusivity in liquid	D_L	1.0×10^{-9} m^2/s
Diffusivity in solid	D_S	0 m^2/s
Entropy of fusion	Δs_f	1.0×10^{6} J/(K·m^3)
Surface energy	σ	2.0×10^{-1} J/m^2
Kinetic coefficient	μ	2.5×10^{-10} m^4/(J·s)
Amplitude of mobility anisotropy	ε_{kin}	30%
Cell size	Δx	1.0×10^{-6} m
Interface thickness	δ	6.0×10^{-6} m
Time step	Δt	2.5×10^{-4} s

Periodic boundary conditions were applied to the left and right hand sides of the domain, and a zero flux condition was applied to the top and bottom. Thermal conditions of a gradient of 15K/mm and a constant pull velocity were used. To reduce the domain size and hence computational cost, a moving frame of reference technique was applied (Diepers, *et al.* 2002).

7.2.1 Prediction on Tip Undercooling

The competitive growth between two differently orientated grains was simulated under different pulling velocities, and the results are shown in Fig. 7.5. All the simulations

started with the same initial conditions: seven equally spaced seeds (120 μm) at the base of the domain with an initial undercooling of 2 K. The preferred growth direction of the two seeds on the left was aligned with the thermal gradient and they can be regarded as a single grain (labelled **A** in Fig. 7.6). The rightmost grain was also aligned with the thermal gradient, and is labelled **C**. Because of the periodic boundaries, it can be considered as part of the grain formed by the two dendrites labelled **A**. The remaining four seeds are misorientated by 15°, labelled **B**, and they can be considered to constitute a second grain. Therefore, two grain boundaries are formed: A-B, where the grains converge; and B-C where the grains diverge. Thus competitive growth at both converging (A-B) and diverging (B-C) grain boundaries can be simulated at the same time.

Three different solidification rates, V, were applied to the simulations to investigate their effect on the competitive growth: (a) 50, (b) 100, and (c) 150 μm/s. The characteristic diffusion length for each solidification rate, defined as $d = D_L/V$, is given in Table 7.2. At the lowest V, d is the largest, with the diffusion fields overlapping to a sufficient extent to delay secondary dendrite arm formation relative to the higher velocities. As shown in Fig. 7.5(a), for a solidification rate of 50 μm/s, the diffusion fields of all the dendrites overlap sufficiently to suppress secondary formation except for where the dendrites diverge at the B-C boundary. For the higher solidification rates (Figs. Fig. 7.5 (b) and (c)), fully developed secondary dendrites form on all primaries.

The solidification rate also has a significant effect upon the primary dendrite tip undercooling, with the predicted values listed in Table 7.2. The average tip undercooling for both fully aligned dendrites ($\Delta T_{0°}$) and inclined dendrites ($\Delta T_{15°}$) increases with increasing solidification rate, although $\Delta T_{15°}$ always remains greater than $\Delta T_{0°}$. The difference in tip undercooling, defined as $\delta(\Delta T) = \Delta T_{15°} - \Delta T_{0°}$, was also increased with increasing solidification rate. (This is illustrated in Fig. 7.5 by a dashed line for the position of the fully aligned dendrites and a dotted line for inclined dendrites.) The distance between these two lines, $\eta = \delta(\Delta T)/G$, increases from 7 to 27 μm as the solidification rate increases from 50 to 150 μm/s.

Table 7.2 Predicted Values for Directional Solidified Dendrites

	Velocity	d	$\Delta T_{0°}$	$\Delta T_{15°}$	$\delta(\Delta T)$	η
(a)	50 μm/s	20 μm	4.03 K	4.14 K	0.11 K	7 μm
(b)	100 μm/s	10 μm	5.73 K	6.00 K	0.27 K	18 μm
(c)	150 μm/s	6.7 μm	7.48 K	7.89 K	0.41 K	27 μm

The average tip undercooling of fully aligned dendrites is less than that of inclined dendrites; therefore, the aligned dendrite will usually grow ahead of the misaligned ones, suppressing and eventually overgrowing them. Some examples of this overgrowth can be seen in Fig. 7.5. However, abnormal overgrowth is also observed (e.g. Fig. 7.5(a2)), where an inclined dendrite overtakes a fully aligned one.

Comparing the values for the critical diffusion length (d) with the gap between the tip positions of the fully aligned and inclined dendrites (η) in simulation (a) $d > \eta$; and in (b) and (c) $d < \eta$. When an inclined dendrite approaches a fully aligned one, the diffusion fields of the two dendrites overlap, and the growth of the two dendrites will both be affected. As a result, in most cases, the inclined dendrite will stop growing, whilst the fully aligned dendrite will simply slow down to a greater or lesser extent. In simulation (b) and (c), where $d < \eta$, the tip of the inclined dendrite is well behind that of the fully aligned dendrite, and this distance is greater than the critical diffusion length, thus the diffusion field of the inclined dendrite has little effect on the growth velocity of the fully aligned dendrite. However in simulation (a), where $d > \eta$, the critical diffusion length is larger than the distance between the two tips, therefore the effect becomes more significant. As shown in Fig. 7.5 (a1), a fully aligned dendrite is overtaking an inclined dendrite, and its growth velocity is obviously slower than other fully aligned dendrites. Subsequently, when it comes into contact with the next inclined dendrite, it is overtaken by the latter, as shown in Fig. 7.5 (a2). Such abnormal overgrowth was only observed in simulations with a low solidification rate, because in the simulations with high solidification rate the large tip undercooling difference counteracts the effect of overlapping diffusion fields.

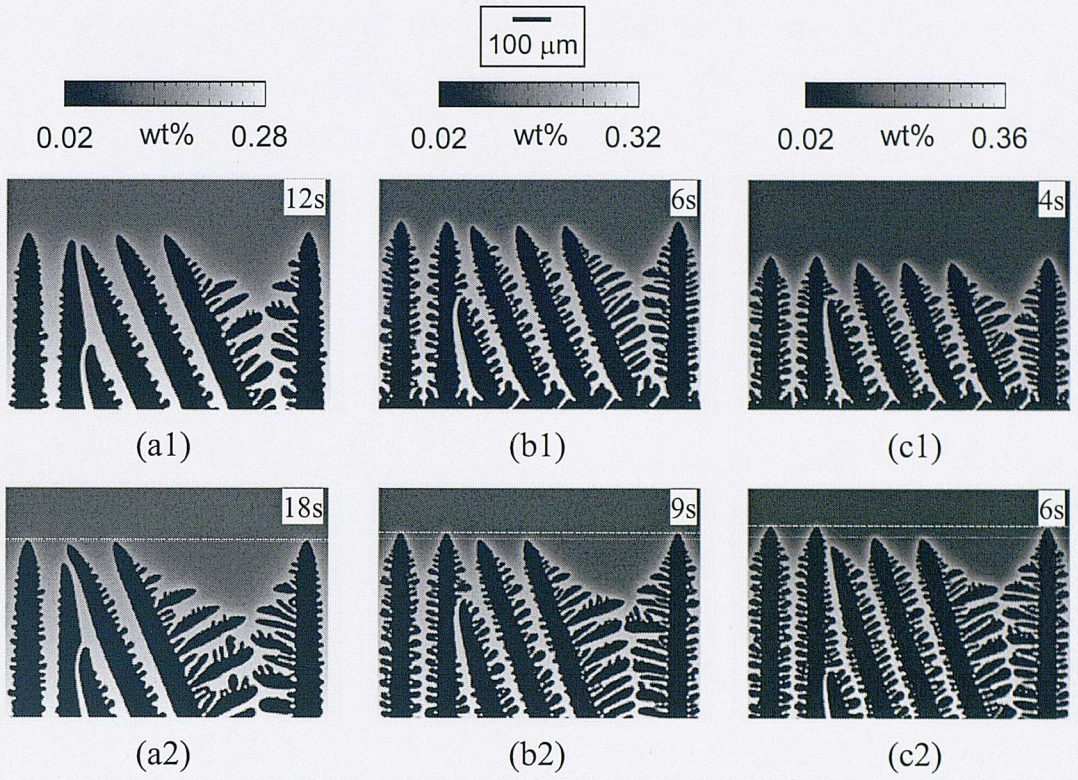

Fig. 7.5 Simulated interaction of dendrite tips normal to, and inclined with the thermal gradient for three growth velocities: (a) 50 μm/s, (b) 100 μm/s, and (c) 150 μm/s.

7.2.2 Grain Selection

During processes such as solidification in the grain selector of single crystal turbine blades, the rate at which, and/or distance over which, overgrowth occurs, is also important. Therefore, the final dendritic structure for the three withdrawal velocities was also examined, as shown in Fig. 7.6. The grain with its preferred growth direction oriented perpendicular to the isotherms always has overgrown that misoriented by 15° when the primary dendrite spacing is the same in both grains. However, the distance grain B grows before being completely overtaken reduces with increasing solidification velocity, decreasing from 3.3 mm at 50 μm/s to 1.9 mm at 150 μm/s. Two factors contribute to this change in overgrowth distance: i) the different behaviour of the dendrite overgrowth at the converging boundary (A-B) due to the reduced size of the solute layer with increasing velocity, as discussed above, and ii) the different

direction of the diverging boundary (B-C). Although in the three simulations grain B has an identical misorientation (15°) and grain C is perfectly aligned with the temperature gradient, the diverging grain boundary has a different orientation, changing from 7 to 9° with increasing solidification rate. The higher solidification rate is more favourable for the fast selection of a well oriented grain. This is contrary to the accepted practice when casting of directionally solidified nickel-base superalloy turbine blades, where lower solidification rates are often used when more stringent texture control is required. In theory, one could conclude that high velocity should used; however, there are many other factors, such as the altered furnace designs required to maintain flat isotherms, which must be considered when commercially casting clusters of turbine blades.

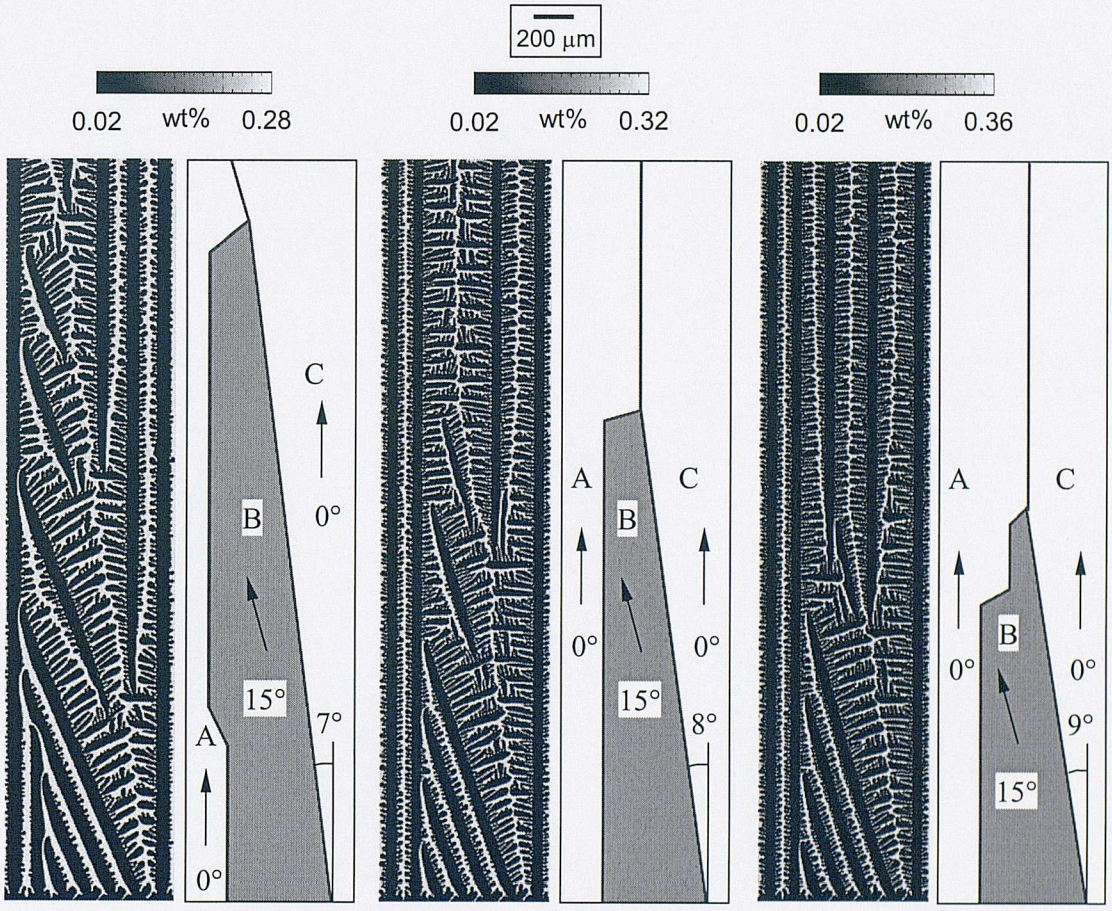

Fig. 7.6 Final dendritic structure and an associated schematic of the grain boundaries for competitive growth at withdrawal rates of: (a) 50 µm/s, (b) 100 µm/s, and (c) 150 µm/s.

7.2.3 Anomalous Grain Selection

All of the calculations shown above exhibit a similar primary spacing between the different dendritic grains. However the primary spacing under transient casting conditions depends on the history of the process (see Chapter 4), and there is a wide range of possible stable spacings. Therefore this assumption is quite restrictive. For this reason, a simulation was also performed where the initial spacing of the misaligned grain was larger than the well aligned grain. In Fig. 7.7 (c) the left grain, which is well aligned with the temperature gradient, starts with a spacing that is half of the spacing of the middle grain with a misalignment of 15°. Fig. 7.7 (a) and (b) show the development of dendrites at solidification time of 12 and 18 s, respectively. It can be seen that the inclined dendrites grow slightly faster than the aligned ones. Fig. 7.7 (c) shows that the misaligned grain systematically overgrows the well aligned grain. The cause of this behaviour is due to the dependence of tip undercooling on the primary spacing. A dendritic array with a wide spacing shows a lower solutal tip undercooling than a tight array, where the solutal fields of neighbouring tips strongly overlap. This dependency of undercooling on spacing was predicted by prior authors (Warren, *et al.* 1993) and is reproduced by the phase field simulations. A novel implication of this effect presented here, is that under certain conditions the reduction of tip undercooling due to 'wide' spacing can overcompensate the enhanced tip undercooling due to misalignment. When this happens, a systematic overgrowth of a well aligned grain by a misaligned grain can occur.

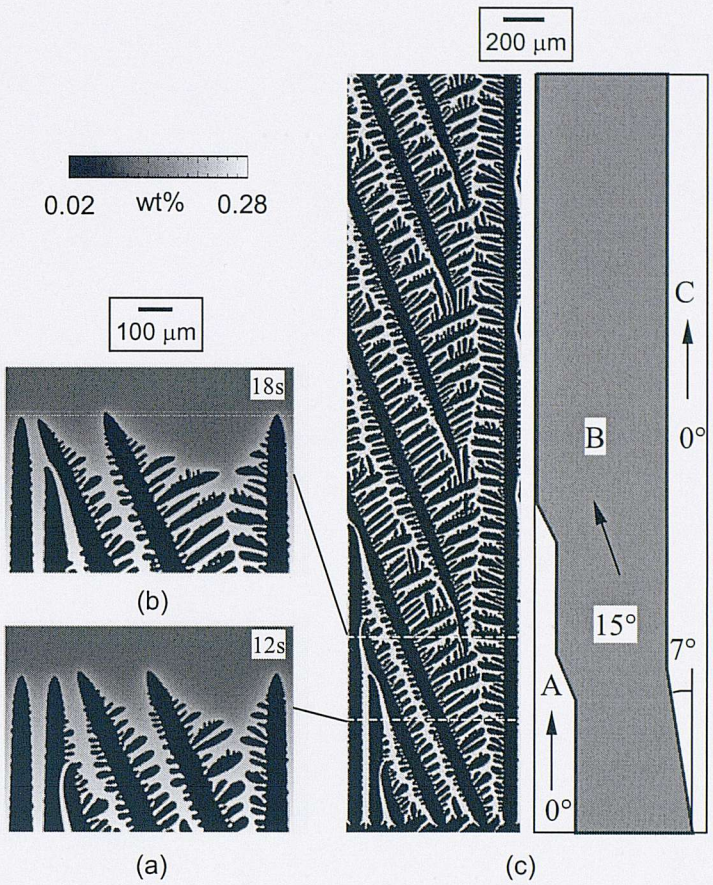

Fig. 7.7 Prediction on the competitive growth between normal grains with a narrow spacing and inclined grains with a wide spacing at a pulling velocity of 50 μm/s. (a) the dendritic structure at solidification time of 12 s; (b) at time of 18 s; and (c) the final structure.

7.2.4 Summary

The dendrite tip undercooling during columnar growth in directional solidification is affected by both the pulling velocity and the orientation of the preferred growth direction of the dendrites relative to the thermal gradient. Higher pulling velocity and greater misorientations both result in increased tip undercooling. This increase in tip undercooling with increasing misorientation leads to the overgrowth of misaligned grains, and the effectiveness of this competitive growth depends on the withdrawal velocity. At high pulling velocities, the difference in tip undercooling is large, resulting in the aligned dendrites always overtaking those misorientated ones. However, at a low

solidification rate of 50 μm/s, the tip undercooling is small and hence occasionally a misorientated dendrite overtook a well aligned one. The higher the solidification rate, the faster the misorientated grains are overgrown by aligned ones. Another finding of this study was a mechanism for 'anomalous grain selection' due to the dependence of tip undercooling on the width of primary spacing.

However, although Fig. 7.7 suggests the probable mechanism of abnormal overgrowth, more detailed studies are needed to produce a fully quantitative description. Some of the latest simulations show that the phase field model also has a dependence on the grid it runs on which is discussed in the Appendix A.

Chapter 8
Conclusions and Future Work

A mathematical model of dendritic microstructures was developed during the course of this work which combines a description of grain nucleation and growth by means of a cellular automaton technique and a finite difference computation of solute diffusion. This model has been used to simulate three specific aspects of microstructural development in nickel-based superalloys: (i) selection of stable primary dendrite spacing during directional solidification with various growth conditions; (ii) multi-directional dendritic growth in the platform region of turbine blade; and (iii) competitive growth at converging and diverging grain boundaries. The model was subject to some limitations when simulating competitive growth and a phase field model developed by Access, RWTH-Aachen was therefore used to investigate competitive grain growth during directional solidification.

The conclusions drawn from this study are presented in this chapter, together with recommendations for future work.

8.1 Conclusions

The following conclusions can be drawn from the simulations carried out.

Two-dimensional simulations were carried out for the directional solidification of dendritic grains developing from seeds placed at the base of the simulation domain. The initial seed density has a direct effect on the initial growth stage of columnar dendrites, but little effect on the final primary dendrite spacing after growth becomes stable. The columnar dendrites adjust their spacing during solidification by branching and/or overgrowth and there is a range of stable primary dendrite spacing for any given growth condition. The maximum stable spacing is about three times the minimum value.

The influence on the dendritic structures of processing parameters such as the pulling velocity and the thermal gradient was studied. The mean value of stable primary dendrite spacing has a power law relationship with the pulling velocity and with the thermal gradient. Both higher pulling velocity and thermal gradient result in smaller primary spacing. The predicted relationships between the primary spacing, the pulling

velocity and the thermal gradient show excellent correlation with earlier theoretical analysis and other numerical predictions.

Perturbations of the processing parameters were also examined. Increases in pulling velocity and in thermal gradient lead to a reduction in primary spacing. The dendrite spacing selection has the effect of hysteresis in that the change in the spacing in response to the variation of the processing parameters does not always take place immediately. When the processing parameters are restored to the original values after a cycle of variation, the primary dendrite spacing does not necessarily return to its original value. The primary dendrite spacing is dependent on history rather than only the current processing parameters, and is affected by the process leading to the prevailing conditions.

Perturbation of the pulling velocity affects both the primary dendrite spacing and the tip undercooling. Primary dendrite spacing has a much narrower distribution after a cycle of variation of the pulling velocity around a mean value. The upper limit of the stable primary dendrite spacing is about two times the lower limit. After reaching a minimum value the tip undercooling increases with the pulling velocity. The increase in the tip undercooling can facilitate the nucleation of small equiaxed grains near the primary tips, and eventually a transition from columnar to equiaxed structure may occur.

Three-dimensional simulations were also performed for directional solidification with seeds placed at the base of the simulation domain. The seeds were arranged in such a way that the columnar dendrites developing from them formed either a square or a hexagonal packing pattern. As with the two-dimensional simulations, there is a range of stable primary dendrite spacings in three-dimensions, the upper limit of which is about three times the lower limit. Compared with the two-dimensional results, the whole range of stable spacing is shifted to smaller values by a factor of about 1.7. The three-dimensional simulations were compared with earlier experimental results and were found to be in good agreement.

The model was then used to simulate dendritic growth in the platform region of single crystal superalloy turbine blades. Differently shaped isotherms moving at a constant velocity were imposed. A significant degree of undercooling develops at the platform

region in front of the secondary dendrites. The maximum undercooling increases as the local temperature gradient increasingly deviates from the withdrawal direction. The increase in undercooling for the curved interfaces found when casting clusters of blades is nearly four times the steady state value, with a significant increase in the chance of stray grains formation. Even where stray grains are avoided, a complex dendritic pattern with a self-convergent grain boundary forms, which is in excellent agreement with experimental observations.

The model was also used to simulate competitive growth between grains with different misorientations with respect to the macro-scale growth direction in directional solidification. Competitive growth at both converging and diverging grains was simulated and compared well with earlier experimental results.

A phase field model was applied to further investigate competitive grain growth. The tip undercooling of the dendrites during directional solidification is affected by both the pulling velocity and the orientation of the preferred growth direction of the dendrites relative to the thermal gradient. Higher pulling velocity and greater misorientation both result in increased tip undercooling. This increase with increasing misorientation leads to the overgrowth of misaligned grains, and the efficiency of this competitive growth is dependent upon the pulling velocity. At high solidification rates, the difference in tip undercooling is large, with the results that the aligned overtake misorientated dendrites. Although the simulation results suggest a probable mechanism for anomalous grain selection at low pulling velocity arising from the dependence of tip undercooling on the width of primary spacing, more studies are needed to produce a fully quantitative description.

These conclusions suggest potential applications of the model: to tailor the primary dendrite spacing either by selecting an appropriate seed density or through controlled growth history; to reduce the chances of stray grains forming during the solidification of turbine blades with a platform region; and to improve the design of a 'pig-tail' selector to facilitate the grain selection process.

8.2 Future Work

Based on these simulation results and the conclusions drawn from them, the following recommendations are made for future work to complement this study.

It has been shown in Chapter 4 that in the current CA-FD model, the dependence on the grid size has not yet been eliminated. The simulated dendritic morphology and the predicted tip radius are both affected by the cell size and thus a major improvement in the model is necessary to reduce this dependence on grid size.

In current simulations thermal conditions are always well defined, i.e. a constant thermal gradient and a fixed cooling rate are imposed. But it is desirable to couple the model with a finite element or finite difference model of heat diffusion so that simulations can be carried out under more realistic conditions.

The main purpose in implementing the decentred square/octahedron growth algorithm in the model is to allow simulation of the growth of dendritic grains with random misorientations with respect to the macro-scale solidification direction. Although, as shown in Chapter 7, the model can provide quite good qualitative predictions of competitive grain growth, it lacks the accuracy to perform quantitative simulations which is why the phase field model has been used to investigate the problem of competitive growth. There are still many further improvements that can be made for example considering multicomponent alloys.

References

Ahmad, N. A., Wheeler, A. A., Boettinger, W. J. and Mcfadden, G. B. (1998), Solute Trapping and Solute Drag in a Phase-Field Model of Rapid Solidification, Phys. Rev. E, 58: 3436-3450

Anderson, M. P., Srolovitz, D. J., Grest, G. S. and Sahni, P. S. (1984), Computer Simulation of Grain Growth-I. Kinetics, Acta Mater., 32: 783-791

Auburtin, P., Wang, T., Cockcroft, S. L. and Mitchell, A. (2000), Freckle formation and freckle criterion in superalloy castings, Metall. Mater. Trans. B, 31: 801-811

Beltran-Sanchez, L. and Stefanescu, D. M. (2002), Growth of Solutal Dendrites - A Celluar Automaton Model, Int. J. Cast Metals Res., 15: 251-256

Boettinger, W. J., Coriell, S. R., Greer, A. L., Karma, A., Kurz, W., Rappaz, M. and Trivedi, R. (2000), Solidification Microstructures: Recent Developments, Future Directions, Acta Mater., 48: 43-70

Boettinger, W. J. and Warren, J. A. (1996), The Phase-Field Method: Simulation of Alloy Dendritic Solidification during Recalescence, Metall. Mater. Trans. A, 27: 657-669

Boettinger, W. J. and Warren, J. A. (1999), Simulation of the Cell to Plane Front Transition during Directional Solidification at High Velocity, J. Cryst. Growth, 200: 583-591

Bradley, E. F. (1988), Superalloys, ASM International,,

Braun, R. J., Mcfadden, G. B. and Coriell, S. R. (1994), Morphological Instability in Phase-Field Models of Solidification, Phys. Rev. E, 49: 4336-4352

Broughton, J. Q., Bonissent, A. and Abraham, F. F. (1981), The Fcc (111) and (100) Crystal-Melt Interfaces: A Comparison by Molecular Dynamics Simulation, J. Chem. Phys., 74: 4029

Brown, S. G. R. and Spittle, J. A. (1989), Computer Simulation of Grain Growth and Macrostructure Development during Solidification, Mater. Sci. Tech., 5: 362-368

Brown, S. G. R., Williams, T. and Spittle, J. A. (1994), A Cellular Automaton Model of the Steady-State "Free" Growth of A Non-Isothermal Dendrite, Acta Metall. Mater., 42: 2893-2898

Caginalp, G. and Xie, W. (1993), Phase-field and Sharp-Interface Alloy Models, Phys. Rev. E, 48: 1897-1910

Charbon, C. and Rappaz, M. (1993), 3D Probabilistic Modelling of Equiaxed Eutectic Solidification, Modelling Simul. Mater. Sci. Eng., 1: 455-466

Copley, S. M., Giamei, A. F., Johnson, S. M. and Hornbecker, M. F. (1970), The Origin of Freckles in Unidirectionally Solidified Castings, Met. Trans. A, A1: 2193-2203

Davies, H. A., Shohojin, N. and Warrington, D. H. (1980), in e. a. Mehrabian Eds. Rapid Solidification Processing Principles and Technologies II, 153-164

Desbiolles, J.-L., Gandin, C.-A., Joyeux, J. F., Rappaz, M. and Thevoz, P. (1998), A 3D CAFE Model for the Prediction of Solidification Grain Structures, in B. G. Thomas and B. C. Eds. Proceedings of the Eighth International Conference on Modeling of Casting and Welding Processes, San Diego, California, 433-440

Diepers, H.-J., Beckermann, C. and Steinbach, I. (1998), Modeling of convection-influenced coarsening of a binary alloy mush using the phase-field method, in B. G. Thomas and C. Beckermann Eds. Proceedings of the Eighth International Conference on Modeling of Casting and Welding Processes, San Diego, California, 565-572

Diepers, H.-J., Ma, D. and Steinbach, I. (2002), History Effects during the Selection of Primary Dendrite Spacing. Comparison of Phase-Field Simulations with Experimental Observations, J. Cryst. Growth, 237-239: 149-153

D'souza, N. (1999), Texture Evolution and Mircrosegregation during Directional and Single Crystal Solidification of the Nickel Based Superalloy, CMSX4, Materials, Imperial College, London

D'souza, N., Ardakani, M. G., Mclean, M. and Shollock, B. A. (2000), Directional and Single-Crystal Solidification of Ni-Base Superalloys: Part I. The Role of Curved Isotherms on Grain Selection, Metall. Mater. Trans. A, 31A: 2877-2886

Espi (2003), INCONEL 718, http://www.espimetals.com/tech/inconel718.pdf

Flemings, M. C. (1974), Solidification Processing, McGraw-Hill, Inc.,

Gandin, C.-A., Jalanti, T. and Rappaz, M. (1998), Modeling of Dendritic Grain Structures, in B. G. Thomas and C. Beckermann Eds. Proceedings of the Eighth International Conference on Modeling of Casting and Welding Processes, San Diego, California, 363-374

Gandin, C.-A. and Rappaz, M. (1994a), A Coupled Finite Element-Cellular Automaton Model for the Prediction of Dendritic Grain Structures in Solidification Processes, Acta Metall. Mater., 42: 2233-2246

Gandin, C.-A. and Rappaz, M. (1997), A 3D Cellular Automaton Algorithm for the Prediction of Dendritic Grain Growth, Acta Mater., 45: 2187-2195

Gandin, C.-A., Rappaz, M. and Tintillier, R. (1993), Three-Dimensional Probabilistic Simulation Of Solidification Grain Structures: Application To Superalloy Precision Castings, Metall. Trans. A, 24: 467-479

Gandin, C.-A., Rappaz, M. and Tintillier, R. (1994b), 3-Dimensional Simulation of the Grain Formation in Investment Castings, Metall. Trans. A, 25A: 629-635

Gandin, C.-A., Rappaz, M., West, D. and Adams, B. L. (1995), Grain Texture Evolution during the Columnar Growth of Dendritic Alloys, Metall. Mater. Trans. A, 26: 1543-1551

Gandin, C.-A., Schaefer, R. J. and Rappaz, M. (1996), Analytical and Numerical Predictions of Dendritic Grain Envolpes, Acta Mater., 44: 3339-3347

Huang, W., Geng, X. and Zhou, Y. (1993), Primary Spacing Selection of Constrained Dendritic Growth, J. Cryst. Growth, 134: 105-115

Hunt, J. D. (1979), Keynote Address: Cellular and primary dendrite spacings, Solidification Cast. Met., Proc. Int. Conf. Solidification, Met. Society, 3-9

Hunt, J. D. (1991), A Numerical Analysis of Dendritic and Cellular Growth of A Pure Material Investigating the Transition from 'Array' to 'Isolated' Growth, Acta Metall. Mater., 30: 2117-2133

Hunt, J. D. and Lu, S.-Z. (1996), Numerical Modeling of Cellular/Dendritic Array Growth: Spacing and Structure Predictions, Metall. Mater. Trans. A, 27: 611-623

Jackson, K. A. and Hunt, J. D. (1965), Transparent compounds that freeze like metals, Acta Metall, 13: 1212-1215

Jackson, K. A. and Hunt, J. D. (1966), Lamellar and Rod Eutectic Growth, Trans. Metall. Soc. AIME, 236: 1129-1142

Karma, A. and Rappel, W. J. (1996), Phase-Field Method for Computationally Efficient Modeling of Solidification with Arbitrary Interface Kinetics, Phys. Rev. E, 53: 3017-3020

Kermanpur, A., Varahraam, N., Engilehei, E., Mohammadzadeh, M. and Davami, P. (2000), Directional solidification of Ni base superalloy IN738LC to improve creep properties, Mater. Sci. Tech., 16: 579-586

Kobayashi, R. (1993), Modeling and Numerical Simulations of Dendritic Crystal Growth, Physica D, 63: 410-423

Koss, M. B., Lacombe, J. C., Tennenhouse, L. A., Glicksman, M. E. and Winsa, E. A. (1999), Dendritic Growth Tip Velocities and Radii of Curvature in Microgravity, Metall. Mater. Trans. A, 30: 3177-3190

Krumbhaar, H. M. and Kurz, W. (1991), Solidification, in P. Hassen Eds. Mater. Sci. Tech., VCH-Verlag, Weinheim,

Kurz, W. and Fisher, D. J. (1992), Fundamentals of Solidification, Trans Tech Pub.,

Kurz, W., Giovanola, B. and Trivedi, R. (1986), Theory of Microstructural Development during Rapid Solidification, Acta Metall., 34: 823-830

Laxmanan, V. (1985), Dendritic Solidification-I: Analysis of Current Theories and Models, Acta Metall, 33: 1023-1036

Loginova, I., Amberg, G. and Agren, J. (2001), Phase-Field Simulation of Non-isothermal Binary Alloy Solidification, Acta Mater., 49: 573-581

Ma, D. (2002), Modeling of Primary Spacing Selection in Dendrite Arrays during Directional Solidification, Metall. Mater. Trans. B, 33: 223-233

Ma, D. (2003), Response of Primary Dendrite Spacing to Varying Temperature Gradient during Directional Solidification, Metall. Mater. Trans. A, Submitted

Mccartney, D. G. and Hunt, J. D. (1984), A Numerical Finite Difference Model of Steady State Cellular and Dendritic Growth, Metall. Trans. A, 15: 983-994

Mcfadden, G. B., Wheeler, A. A., Braun, R. J. and Coriell, S. R. (1993), Phase-Field Models for Anisotropic Interfaces, Phys. Rev. E, 48: 2016-2023

Mclean, M. (1983), Directionally Solidified Materials for High Temperature Service, The Metals Society,

Meyer Ter Vehn, M., Dedecke, D., Paul, U. and Sahm, P. R. (1996), Undercooling Related Casting Defects in Single Crystal Turbine Blades, in R. D. Kissingger, Deye, D.J., Anton, D.L., Cetel, A.D., Nathal, M.V., Pollock, T.M., and Woodford, D.A. Eds. Superalloys 1996, Pennsylvania, USA, 471-479

Napolitano, R. E. and Schaefer, R. J. (2000), The Convergence-Fault Mechanism for Low-Angle Boundary Formation in Single-Crystal Castings, J. Mater. Sci., 35: 1641-1659

Nastac, L. (2000), A Stochastic Approach for Simulation of Solidification Morphologies and Segregation Patterns in Cast Alloys, in P. R. Sahm, P. N. Hansen and J. G. Conley Eds. Modeling of Casting, Welding and Advanced Solidification Processes - IX, Aachen, Germany, 497-504

Nastac, L. and Stefanescu, D. M. (1997), Stochastic Modelling of Microstructure Formation in Solidification Processes, Modelling Simul. Mater. Sci. Eng., 5: 391-420

Paul, U., Sahm, P. R. and Goldschmidt, D. (1993), Inhomogenities in Single-Crystal Components, Mat. Sci. and Eng. A, A173: 49-54

Pollock, T. M. and Murphy, W. H. (1996), The breakdown of single-crystal solidification in high refractory nickel-base alloys, Metall. Mater. Trans. A, 27A: 1081-1094

Pollock, T. M., Murphy, W. H., Goldman, E. H., Uram, D. L. and Tu, J. S. (1992), Grain Deffect Formation during Directional Solidification of Nickel Based Single Crystals, in S. D. Antolovich, R. W. Stusrud, R. A. MacKay, D. L. Anton, T. Khan, R. D. Kissinger and D. L. Klarstrom Eds. The 7th International Symposium on Superalloys, Champion, Pennsylvania, 125-134

Provatas, N., Goldenfeld, N. and Dantzig, J. (1998), Efficient Computation of Dendritic Microstructures Using Adaptive Mesh Refinement, Phys. Rev. Lett., 80: 3308-3311

Raabe, D. (1998), Computational Materials Science, Weinheim ; Chichester : Wiley-VCH,,

Rappaz, M. and Gandin, C.-A. (1993), Probablistic Modelling of Microstructure Formation in Solidification Process, Acta Metall. Mater., 41: 345-360

Rappaz, M. and Thevoz, P. H. (1987a), Solute Diffusion Model for Equiaxed Dendritic Growth, Acta Metall., 35: 1487-1497

Rappaz, M. and Thevoz, P. H. (1987b), Solute Diffusion Model for Equiaxed Dendritic Growth: Analytical Solution, Acta Metall., 35: 2929-2933

Schaefer, R. J., Black, D. R., Vaudin, M. D., Mueller, B. R. and Giamei, A. F. (1997), Geometry and Mechanisms of Dendrite Misalignments in Superalloy Single Crystals, in J. a. J. Beech, H. Eds. 4th Decenninal International Conference on Solidification Processing, Sheffield, UK, 37-40

Semoroz, A., Henry, S. and Rappaz, M. (2000), Application of the Phase-Field Method to the Solidification of Hot-Dipped Galvanized Coatings, Metall. Mater. Trans. A, 31: 487-495

Somboonsuk, K. and Trivedi, R. (1985), Dynamic Studies of Dendritic Growth, Acta Mater., 33: 1051-1060

Spittle, J. A. and Brown, S. G. R. (1989a), J. Mater. Sci., 23: 1777

Spittle, J. A. and Brown, S. G. R. (1989b), Computer Simulation of the Effects of Alloy Variables on the Grain Structures of Castings, Acta Metall., 37: 1803-1810

Steinbach, I., Kauerauf, B., Beckermann, C., Guo, J. and Li, Q. (1998a), Three-dimensional modeling of equiaxed dendritic growth on a mesoscopic scale, in B. G. Thomas and C. Beckermann Eds. Proceedings of the Eighth International Conference on Modeling of Casting and Welding Processes, San Diego, California, 565-572

Steinbach, I., Pezzolla, F., Nestler, B., Seebelberg, M., Prieler, R., Schmitz, G. J. and Rezende, J. L. L. (1996), A Phase Field Concept for Multiphase Systems, Physica D, 94: 135-147

Steinbach, I. and Schmitz, G. J. (1998b), Direct numerical simulation of solidification structure using the phase field method, in B. G. Thomas and C. Beckermann Eds. Proceedings of the Eighth International Conference on Modeling of Casting and Welding Processes, San Diego, California, 521-532

Thevoz, P., Desbiolles, J. L. and Rappaz, M. (1989), Modeling of Equiaxed Microstructure Formation in Casting, Metall. Trans. A, 20: 311-322

Tiaden, J. and Grafe, U. (1999), A Phase-Field Model for Diffusion and Curvature Controlled Phase Transformations in Steels, in M. Koiwa, K. Otsuka and T. Miyazaki Eds. Proceedings of the International Conference on Solid-Solid Phase Transformations '99 (JIMIC-3), Kyoto, 737-740

Tiaden, J., Nestler, B., Diepers, H. J. and Steinbach, I. (1998), The Multiphase-Field Model with an Integrated Concept for Modelling Solute Diffusion, Physica D, 115: 73-86

Tien, J. K. and Caulfield, T. (1989), Superalloys, Supercomposites and Superceremics, Academic Press,

Wagner, A., D'souza, N., Shollock, B. A. and Mclean, M. (2001), Competitive grain growth and solute partitioning in Ni-base Superalloys, in Alec Mitchell and J. V. D. Avyle Eds. Proceeding of the 2001 International Symposium on Liquid Metal Processing and Casting, Santa Fe, New Mexico, 301-313

Wan, X., Han, Q. and Hunt, J. D. (1997), Different Growth Regimes during Directional Dendritic Growth, Acta Mater., 45: 3975-3979

Wang, W., Kermanpur, A., Lee, P. D., Mclean, M., Wang, X., Ward, R. M. and Jacobs, M. H. (2001), An Investigation of the Effect of Perturbations on Dendritic Growth in Nickel Base Superalloys, in Alec Mitchell and J. V. D. Avyle Eds. Proc. Int. Sym. on Liq. Metal Processing and Casting, Santa Fe, New Mexico, 267-279

Warren, J. A. and Boettinger, W. J. (1995), Prediction of Dendritic Growth and Microsegregation Patterns in A Binary Alloy Using the Phase-Field Method, Acta Mater., 43: 689-703

Warren, J. A. and Langer, J. S. (1993), Prediction of Dendritic Spacings in A Directional-Solidification Experiment, Phys. Rev. E, 47: 2702-2712

Wheeler, A. A., Boettinger, W. J. and Mcfadden, G. B. (1992), Phase-Field Model for Isothermal Phase Transitions in Binary Alloys, Phys. Rev. E, 45: 7424-9439

Xu, Q. Y., Feng, W. M. and Liu, B., C. (2002a), Stochastic Modeling of Dendritic Microstructur of Aluminum Alloy, Int. J. Cast Metals Res., 15: 225-230

Xu, X., Zhang, W., Atwood, R. C., Sridhar, S., Lee, P. D., Mclean, M., Drummings, B., Ward, R. M. and Jacobs, M. H. (1999), Grain Size Predictions in VAR: A Critical Comparison of Micromodelling Approaches, in A. Mitchell Eds. Proc. Int. Sym. on Liq. Metal Proc. & Casting, Santa Fe, New Mexico,, 76-89

Xu, X., Zhang, W. and Lee, P. D. (2002b), Tree-ring formation during vacuum arc remelting of INCONEL 718: Part II. Mathematical modeling, Metall. Mater. Trans. A-Phys. Metall. Mater. Sci., 33: 1805-1815

Xu, X., Zhang, W., Lee, P. D., Mclean, M., Ward, R. M. and Jacobs, M. H. (2000), The Influence of Processing Condition Fluctuations on Defect Formation During VAR of Nickel Based Superalloys, in P. R. Sahm, P. N. Hansen and J. G. Conley Eds. Modeling of Casting, Welding and Advanced Solidification Processes - IX, Aachen, Germany, 574-581

Yao, X., Davidson, C. J., Dahle, A. K. and Stjohn, D. H. (2002), Modelling of Microstructure Formation and Evolution during Solidification, Int. J. Cast Metals Res., 15: 219-223

Yu, K. O., Oti, J. A., Robinson, M. and Carlson, R. G. (1992), Solidification Modeling of Complex-Shaped Single Crystal Turbine Airfoils, in S. D. Antolovich, R. W. Stusrud, R. A. MacKay, D. L. Anton, T. Khan, R. D. Kissinger and D. L. Klarstrom Eds. The 7th International Symposium on Superalloys, Champion, Pennsylvania, 135-144

Zeisler-Mashl, K. L. and Pletka, B. J. (1992), Segregation during Solidification, in S. D. Antolovich, R. W. Stusrud, R. A. MacKay, D. L. Anton, T. Khan, R. D. Kissinger and D. L. Klarstrom Eds. The 7th International Symposium on Superalloys, Champion, Pennsylvania, 175-184

Zhu, M. F. and Hong, C. P. (2003), Modeling of Microstructure Evolution in Eutectic and Peritectic Solidification, in D. M. Stefanescu, J. A. Warren, M. R. Jolly and M. J.

M. Krane Eds. Modelling of Casting, Welding and Advanced Solidification Processes X, Sandestin, Florida, 91-98

Zhu, P. and Smith, R. W. (1992), Dynamic Simulation of Crystal Growth by Monte Carlo Method - I. Model Description and Kinetics, Acta Metall. Mater., 40: 683-692

Zou, J., Wang, H. P., Doherty, R. and Perry, M. (1992), Solidification Behaviour and Microstructure Formation in A Cast Nickel Based Superalloy: Experiment and Modeling, in S. D. Antolovich, R. W. Stusrud, R. A. MacKay, D. L. Anton, T. Khan, R. D. Kissinger and D. L. Klarstrom Eds. The 7th International Symposium on Superalloys, Champion, Pennsylvania, 165-174

Appendices

Appendix A. Some Problems in Phase Field Model

The phase field simulations presented in Chapter 7 suggest that the tip undercooling of columnar dendrites is affected by the primary spacing. More simulations were run to verify this observation. Conditions of G = 50 K/mm and V = 50 K/mm were imposed in these simulations. As shown in Fig. A.1, six simulations were carried out, three of which (cases (a) (b) and (c)) for fully aligned dendrites and the other (cases (d), (e) and (f) for 15° inclined dendrites. Simulation (a) and (d) start with 2 seeds initially placed at the base of the domain; (b) and (e) start with 4 seeds; (c) and (f) start with 6 seeds.

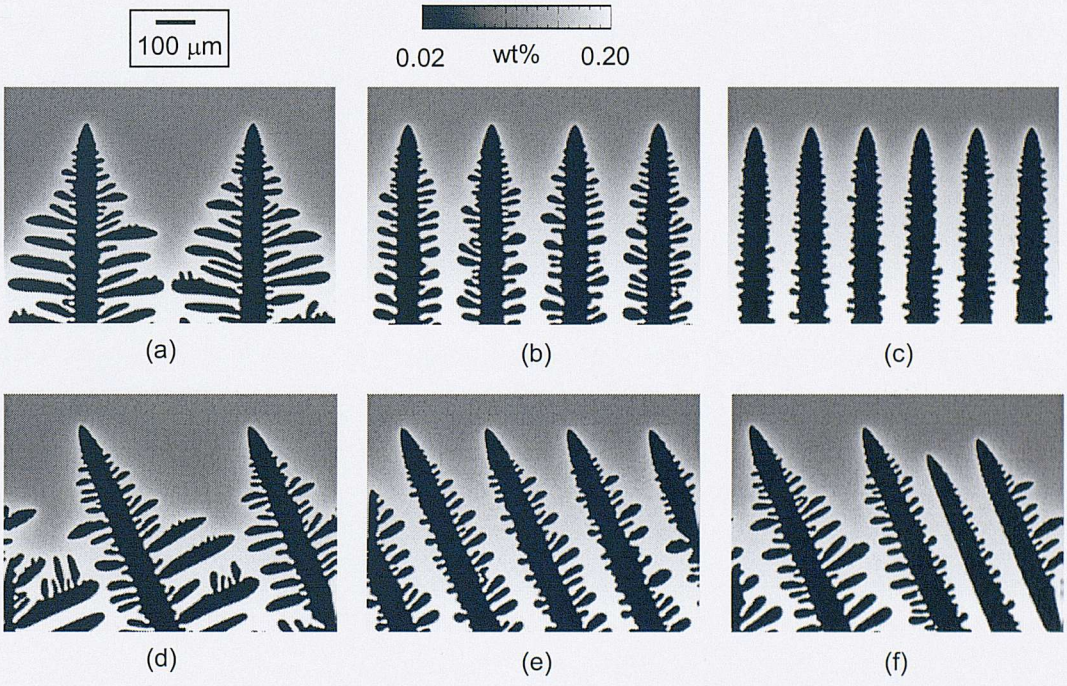

Fig. A.1 Simulation of columnar dendrites under conditions of G = 50 K/mm and V = 50 K/mm. Simulation (a) and (d) starts with 2 seeds placed at the base; (b) and (e) 4 seeds; (c) and (f) 6 seeds. In (a), (b) and (c) dendrites are aligned with the grid; while in (d), (e) and (f) they have a 15° misorientation.

It can be seen that for the aligned cases, dendrites developing from (a) 2, (b) 4 and (c) 6 seeds have all reached a stable growth state after 100 s of growth, and there is a wide range of the stable spacings, varying from 140 to 420 μm. This is in very good agreement with the conclusions drawn from the CA simulation. Although the shapes of the primary tips are slightly affected by the primary spacing, the significant difference in these cases is the development of secondary dendrites. In case (a) where the primary spacing is 420 μm, the secondary dendrites are well developed. And some tiny tertiary dendrites are also observed emanating from the secondaries, but they are all blocked by other latterly formed secondaries. In case (c) where the spacing is only 140 μm, the growth of secondary dendrites is largely suppressed.

The results for the 15° inclined dendrites are different. In case (f), 6 seeds are preset at the base of the domain, after 100 s of growth, 2 of the 6 dendrites are eliminated. But for the cases (d) and (e), the dendrites have reached a stable state.

The tip undercooling is also measured and plotted in Fig. A.2. For the aligned dendrites (a-c), tip undercooling decreases from 3.895 to 3.840 K, or decreases by 0.055 K, as the primary spacing is tripled, from 140 to 420 μm. A similar trend exists for inclined dendrites (d and e): the tip undercooling reduces from 3.820 to 3.780 K, or reduces by 0.040 K, when the primary spacing is doubled, from 210 to 420 μm. However, it is also noted that for both cases of 2 and 4 dendrites, the tip undercooling of the inclined dendrites is lower than the aligned ones, which means, under the given conditions, the inclined dendrites will always overgrow the aligned dendrites. This is unlikely be physically correct.

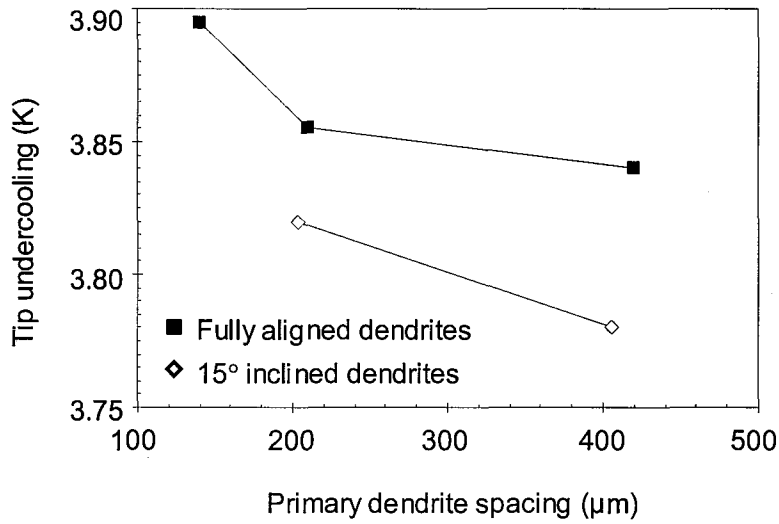

Fig. A.2 Predicted tip undercoolings for the cases shown in Fig. A.1.

Close examination of the shapes of the primary dendrites in Fig. A.1 shows that for the inclined dendrites, the dendrite tip is a little sharper than the aligned ones. However, since the function of output tip curvature has not been incorporated in the version of phase field model being used, it is not possible to give an accurate value for the tip curvatures.

Based on personnel communications with Dr. Ingo Steinbach, the director of the group that developed the phase field model, some possible reasons are suggested: (i) the phase field model has not yet got rid of the grid dependence; (b) since only the anisotropy in the kinetic term is accounted in the model, it would be better to incorporate the anisotropy in surface tension as well.

Published Papers

1. **Wang, W.**, Lee, P.D., Mclean, M., Diepers, H.J. and Steinbach I., "A Phase Field Model of Competitive Grain Growth during Directional Solidification", Modelling and Simulation in Materials Science and Engineering, 2003 (Submitted).

2. Yang, X. L., Dong, H. B., **Wang, W.** and Lee, P. D., "Microscale simulation of stray grain formation in investment cast turbine blades", Materials Science and Engineering A, 2003 (Submitted).

3. Dong, H. B., Yang, X. L., **Wang, W.** and Lee, P. D., "Simulation of Equiaxed Growth ahead of an Advancing Columnar Front in Directionally Solidified Ni-Based Superalloys", in Ed. Lee, P.D., Mitchel, A., Bellot, J-P, Jardy, eds. *Int. Symp. On Liquid Metal Processing and Casting*, Nancy, Sep. 22-25, 2003, 39-48

4. **Wang, W.**, Kermanpur, A., Lee, P.D. and Mclean, M., "Simulation of Dendritic Growth in the Platform Region of Single Crystal Superalloy Turbine Blades", Journal of Materials Science, 2003 (Accepted).

5. **Wang, W.**, Lee, P.D. and Mclean, M., "Simulation of the History Dependence of Primary Dendrite Spacing in Directional Solidification", *Modelling of Casting, Welding and Advanced Solidification Processes X*, Sandestin, Florida, May 25-30, 2003, pp. 83-90.

6. **Wang, W.**, Lee, P.D. and Mclean, M., "A Model of Solidification Microstructures in Nickel Based Superalloys: Predicting Primary Dendrite Spacing Selection". *Acta Materialia,* 51(2003): 2971-2987.

7. Lee, P.D., Chirazi, A., Atwood, R.C. and **Wang, W.**, "Multiscale Modelling of Solidification Microstructures, Including Microsegregation and Microporosity, in An Al-Si-Cu alloy", *Materials Sciences. and Engineering.* A, 2003 (In Print).

8. Kermanpur, A., **Wang, W.**, Lee, P.D. and Mclean, M., "Continuous Variable, Cellular Automaton Model for Grain Growth during the Homogenization of Vacuum Arc Remelted INCONEL 718", *Materials Science and Technology*, 2002 (In Print).

9. **Wang, W.**, Kermanpur, A., Lee, P.D., Mclean, M., Diepers, H.J. and Steinbach, I., "Simulation of Grain Selection in Nickel Based Superalloys", Guo, Z.X. and Winstone, M.R. eds., *The 1st International Conference of Multiscale Materials Modelling*, London, June 17-20 2002 (poster).

10. **Wang, W.**, Kermanpur, A., Lee, P.D. and Mclean, M., "A Microstructural Model of Competitive Growth in Nickel Based Superalloys", *International Journal of Casting Metals*, 15(2002): 269-271.

11. **Wang, W.**, Kermanpur, A., Lee, P.D., Mclean, M., Wang, X., Ward, R.M. and Jacobs, M. H., "An Investigation of the Effect of Perturbations on Dendritic Growth in Nickel Base Superalloys", Mitchell, A. and Avyle, J.V.D. eds., *Proceeding of the 2001 International Symposium on Liquid Metal Processing and Casting*, Santa Fe, New Mexico, Sep 23-26 2001, 267-279.